THE UNIVERSITY OF CALGARY

Borehole seismic surveying: 3C-3D VSP and land vertical cable analysis

by

Jitendra Gulati

A THESIS

SUBMITTED TO THE FACULTY OF GRADUATE STUDIES

IN PARTIAL FULFILMENT OF THE REQUIREMENTS FOR THE

DEGREE OF MASTER OF SCIENCE

DEPARTMENT OF GEOLOGY AND GEOPHYSICS

CALGARY, ALBERTA

DECEMBER, 1998

THE UNIVERSITY OF CALGARY

FACULTY OF GRADUATE STUDIES

The undersigned certify that they have read, and recommend to the Faculty of Graduate Studies for acceptance, a thesis entitled “Borehole seismic surveying: 3C-3D VSP and land vertical cable analysis” submitted by Jitendra Gulati in partial fulfilment of the requirements for the degree of Master of Science

Supervisor, Dr. Robert R. Stewart
Department of Geology and Geophysics

Dr. Donald C. Lawton
Department of Geology and Geophysics

Dr. Laurence R. Lines
Department of Geology and Geophysics

Dr. Michael A. Slawinski
Department of Mechanical and
Manufacturing Engineering

Date

ABSTRACT

This thesis presents analysis of data from two new borehole seismic methods, namely the 3C-3D vertical seismic profile (VSP) and the land vertical cable techniques. Synthetic seismograms and field data from surveys over the Blackfoot oil field in Alberta, Canada are used for the analysis.

Processing flows for the two techniques are developed. A method that uses statistical velocity analysis for VSPCDP stacking is also implemented.

Hodogram analysis, median filtering, VSPCDP stack, and f-xy deconvolution are key steps used in processing the 3C-3D VSP data. Processing of the land vertical cable data primarily involved predictive deconvolution, velocity filtering, VSPCDP stacking, and migration.

The structural images from the two techniques are correlated and interpreted with previously interpreted surface seismic images. Evidence of the productive region (a Glauconitic sand channel) on the 3-D VSP time slices and on the land vertical cable image indicate the promise of these techniques.

ACKNOWLEDGEMENTS

My introduction to borehole seismic methods is largely due to the enthusiasm and inspiration of my supervisor, Dr. Rob Stewart. Through his ideas and feedback, Rob has been instrumental in teaching me about other fields in geophysics as well. Without his support and without the opportunities and facilities in CREWES, this thesis would not have seen the light of day.

Discussions with Dr. Gary Margrave were thoroughly enjoyable and lent a different perspective about geophysics. Brian Hoffe patiently answered some of my most naïve questions and was extremely helpful during processing of the land vertical cable data. Carlos Rodriguez and XinXiang Li have always been there to give geophysical advice during troubleshooting of data processing. Dan Cieslewicz generously shared his experiences with the Blackfoot buried geophone experiment.

I would also like to thank Drs. Kurt M. Strack, Arthur Cheng and Janusz Peron at Baker Atlas, Houston for employing me as a summer intern in 1997. Baker Atlas kindly allowed me to use their SEISLINK processing package on the Blackfoot 3-D VSP and land vertical cable data. The 3-D VSP data used in this thesis was partly processed by John Parkin at Baker Atlas, Calgary. John has been very helpful in giving hints on VSP processing.

I am fortunate to have loving parents such as mine. They have constantly guided and understood me. Last but not least, I thank my wife Anupama for without her I would be doing something other than geophysics.

Dedicated to my parents for their love, support, and teachings.

TABLE OF CONTENTS

LIST OF FIGURES

CHAPTER 1: INTRODUCTION

1.1 New technologies in vertical seismic profiling

The vertical seismic profiling (VSP) is a technique in which seismic signals generated at the surface of the earth are recorded by geophones at various depths in a borehole. The VSP has found a number of applications in the oil industry. Primarily, VSP data have been used to assist surface seismic interpretation through time-to-depth values and a zero-phase, largely multiple-free reflectivity trace. It has given insight into the nature of seismic wave propagation in the earth and provided estimates of rock properties such as interval velocities and attenuation near the borehole. Detailed descriptions about the history and applications of the VSP can be found in Hardage (1983) and in Toksoz and Stewart (1984). Hardage (1992) also describes the reverse VSP (RVSP) technique in which seismic signals generated by a source in a borehole are recorded by receivers at the surface of the earth.

Most VSP surveys to date have either been 1-D (source near the well head) or 2-D (sources in a line out from the well). But the inherent 3-D nature of the earth and a desire to obtain detailed 3-D reservoir information near the well has led to interest in acquiring some type of 3-D data in boreholes. Basically, a 3-D VSP survey is a measurement of seismic signal in borehole detectors using an areal distribution of surface shots. One of the first 3-D VSP surveys is that conducted by AGIP in 1989 in the Brenda field, but it has only been recently that 3-D VSP surveys have started appearing in the public domain. A 3-D VSP conference held in Stavanger, Norway in 1997 and a session dedicated to 3-D

VSP in the Annual SEG Meeting at New Orleans in 1998 are some indicators of the growing interest in 3-D borehole seismic data.

Another area that has recently received renewed interest is the use of hydrophones in acquiring VSP data. Hydrophones offer a rapid and efficient way to acquire VSP data and hence the interest in them. White and Sengbush (1953) and Riggs (1955) were among the first to use hydrophone detectors in acquiring borehole seismic data. Tube waves are the primary stumbling block in the use of hydrophone data. Therefore, properly clamped geophones, which are less sensitive to tube waves, have been the preferred detectors so far. Recently, Findlay et al. (1991), Milligan et al. (1997) and Sheline (1998) demonstrated the viability of using a vertical hydrophone array in their borehole reflection imaging programs.

The marine vertical cable is another new technology that is closely related to the VSP method (Krail, 1994a; Krail, 1994b). In this technique, a cable consisting of a set of vertically separated hydrophone detectors is suspended in water with the help of an anchor at the sea bottom and bouyant floats under the water surface. Krail (1994b) mentions that the marine vertical cable resulted in significant reduction in cost and acquisition speed in a survey over the Gulf of Mexico. He also indicates that the vertical cable resulted in a better image compared to the image from a conventional towed streamer data.

3-D VSP surveys and the use of vertical hydrophone arrays on land (henceforth referred to as land vertical cable) in shallow or deep boreholes are the subject of this thesis. Techniques relevant to the efficient processing of these data are developed and investigated; and real data examples from such surveys analyzed, processed and interpreted in this work. The following sections give an outline of this thesis.

1.2 Introduction to the thesis

Chapter 2 of the thesis is a theoretical development of a VSPCDP mapping technique. Synthetic data are used for comparing the technique with raytrace VSPCDP mapping; thus highlighting its advantages and limitations. Finally, the feasibility of using a standard post-stack migration routine to VSPCDP stacked data is investigated.

Chapter 3 discusses the acquisition, processing and interpretation of real 3-D VSP data. The data used in this chapter is from the 3-D VSP survey shot over the Blackfoot field, which is owned by PanCanadian Petroleum Ltd., in Canada in 1995. This survey (to our knowledge) is the first simultaneous acquisition of a 3-D VSP along with a surface 3-D survey. Detailed descriptions about the survey are given in the chapter. The processing flow used to obtain the final interpretable P-wave and converted-wave time slices from the 3-D VSP data is discussed. Final images from the 3-D VSP data are then correlated with images from the surface 3-D, an offset VSP and synthetic seismograms and interpreted.

Chapter 4 is about land vertical cable acquisition and imaging. The data used in this chapter was obtained during November, 1997 as part of a series of 2-D seismic experiments over the Blackfoot field (see Hoffe et al., 1998 for details). The vertical cable data were recorded by deploying a 48-channel hydrophone cable in a 100m deep, cased and water-filled hole. Acquisition parameters of the data are discussed in this chapter. This is followed by developing a processing flow for land vertical cable data. The processed data are then correlated with 2-D and 3-D images from the same area and finally interpreted.

Chapter 5 provides the final conclusions of the thesis. Future work to improve the 3-D VSP processing flow are also suggested.

1.3 Hardware and software used

The entire work presented in this thesis was performed on the Sun workstation and PC network of the CREWES Project at the University of Calgary. The testing of the VSPCDP mapping techniques was done in the Matlab environment. An existing Matlab P-S raytracing code was adapted to the VSP geometry for this purpose. The implementation of the VSPCDP mapping technique on real data was performed by writing C source codes in Western Atlas Logging Services (WALS) SEISLINK processing package. The 3-D VSP data, as well as the land vertical cable data, were processed using both SEISLINK and ProMax processing packages. Word and image processing for the thesis assembly were performed in MICROSOFT WORD and ADOBE PHOTOSHOP software respectively.

CHAPTER 2: VSP MOVEOUT CORRECTION, MAPPING AND POST-VSPCDP-STACK MIGRATION

2.1 Introduction

Offset and walkaway VSP surveys have been useful in extracting structural information near the well. The structural image from the VSP is, in many cases, obtained from the VSPCDP stacking process (Wyatt and Wyatt, 1984). VSPCDP stacking is an analogue of the surface seismic CMP stacking process. VSPCDP stacking is, however, a more complicated process than CMP stacking. It first involves normal-moveout (NMO) correction. NMO correction is followed by mapping the reflections to their spatial locations and subsequently stacking the data to give an offset-time image.

Raytracing can be used to correct VSP data to normal incidence time (Wyatt and Wyatt, 1984). Velocity information from well-logs, known geology of the area or from surface seismic in the area, and often traveltime inversion of the VSP first-breaks (Stewart, 1984) provide a starting velocity-depth model for raytracing. As both the geometry and frequency content of VSP data are different compared to well-log or surface seismic data, these starting estimates are not optimum for the NMO correction of the VSP data. Also, in the simple case of a horizontally layered earth, velocity anisotropy further complicates determination of the optimum model for the VSP data (Dillon and Thomson, 1984). Thus moveout correction can be a time-consuming process especially for walkaway or 3-D VSPs where the data volume is large and model building comparatively difficult.

Other moveout correction methods such as in Moeckel (1986) and Zhang et. al. (1995) also require a velocity model. These methods calculate the RMS velocity from a model to correct the VSP data to normal incidence time. However, from surface seismic surveys, we know that the stacking velocity is greater than the RMS velocity (Al-Chalabi, 1973). One would then expect that, in a similar way, the above approximation methods may not give the optimum stack for VSP data as well. In such a case, a statistical moveout correction method similar to amplitude semblance analysis (Taner and Koehler, 1969) used in surface seismic surveys may be more desirable. Byun et. al. (1989) used amplitude semblance analysis in their study of anisotropic velocities from VSP data. However, I am not aware of a method described in literature to correct VSP data to normal incidence time using semblance analysis.

After the final velocity-depth model is built, reflections on moveout-corrected VSP data are mapped to their subsurface spatial locations by raytracing through the model (Wyatt and Wyatt, 1984). This process is referred to as VSPCDP transformation or mapping. Although a raytracing approach is accurate in mapping the reflection points, approximate mapping methods such as Stewart (1991) also perform with reasonable accuracy in simple geology. In the case of a 3-D VSP, 3-D raytracing may be a time-consuming process and likely to be unnecessary in a simple geology.

In this chapter, a method is developed for the rapid VSPCDP stacking of VSP data and tested on synthetic VSP data. The possibilities and limitations of applying a standard post-stack migration routine to VSPCDP stacked data are also investigated.

2.2 Normal moveout correction of VSP data

Taner and Koehler (1969) used a power series expansion of the parametric traveltime-distance equations and showed that the offset-traveltime relation is a hyperbola for surface seismic surveys. This relation provides a framework for normal moveout (NMO) correction of surface recorded signals in the common midpoint (CMP) domain. In the following, an equivalent series expansion for VSP-recorded signals is presented which shows that the traveltime-distance formula is hyperbolic for VSP- recorded signals as well. This relation provides an opportunity to NMO-correct VSP records, similar to that performed in surface seismic surveys.

2.2.1 Power series expansion for traveltimes of reflected signals in the VSP geometry

Taner and Koehler (1969) expanded the traveltime of reflected waves recorded on the surface over a horizontally layered medium into a power series as

$$t_n^2(x^2) = c_1 + c_2 x^2 + c_3 x^4 + c_4 x^6 + \ldots\ldots \quad , \qquad (2.1)$$

where the coefficients c_i (i=1,2,3,..) are functions of the thickness and velocity of the layers, and t_n is the traveltime for reflection at the n-th layer with source at an offset x from the receiver.

Using arguments as in Taner and Koehler (1969), one can obtain a similar result for the VSP geometry as well. The asymmetry of the downgoing and upgoing raypaths in the VSP geometry makes the derivation similar to that for converted waves as in Tessmer and Behle (1988). However, I was unaware of this similarity when deriving the following relations for P-wave arrivals in the VSP based on the Taner and Koehler (1969) derivation.

In a horizontally layered medium, the *t-x* relationship for reflections recorded in a borehole can be expressed in the parametric form (Slotnick, 1959) as

$$x = \sum_{k=1}^{k=n} \frac{p v_k d_k}{\sqrt{1 - p^2 v_k^2}} + \sum_{j=n}^{j=m} \frac{p v_j d_j}{\sqrt{1 - p^2 v_j^2}}, \text{ and}$$

$$t = \sum_{k=1}^{k=n} \frac{d_k / v_k}{\sqrt{1 - p^2 v_k^2}} + \sum_{j=n}^{j=m} \frac{d_j / v_j}{\sqrt{1 - p^2 v_j^2}}$$

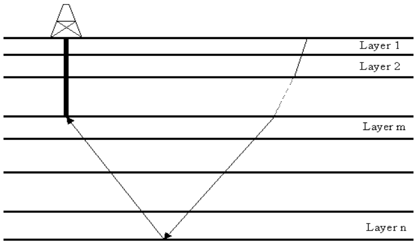

where v_k and d_k are the P-wave velocity and thickness of the k-th layer and p is the ray parameter given by Snell's law as

$p = \frac{\sin q_k}{v_k}$, where q_k is the angle of incidence of the ray at the k-th layer.

Here for the sake of brevity, I assume that the receiver is located at the base of the (m-1)th layer. This assumption, however, does not make a difference in the final result.

Using a Taylor series expansion of the function $(1 - p^2 v_k^2)^{-1/2}$, the above equations can be rewritten as

$$x = \sum_{k=1}^{k=n} p v_k d_k \sum_{i=1}^{\infty} \frac{1.3.5.....(2i-3)}{2.4.6.....(2i-2)} p^{2i-2} v_k^{2i-2} + \sum_{j=n}^{j=m} p v_j d_j \sum_{i=1}^{\infty} \frac{1.3.5....(2i-3)}{2.4.6.....(2i-2)} p^{2i-2} v_j^{2i-2}$$

$$= \sum_{i=1}^{\infty} \frac{1.3.5....(2i-3)}{2.4.6....(2i-2)} p^{2i-1} [\sum_{k=1}^{k=n} v_k^{2(i+1)-3} d_k + \sum_{j=n}^{j=m} v_j^{2(i+1)-3} d_j] \qquad (2.2)$$

Let $q_1 = 1$, $q_i = \frac{1.3.5....(2i-3)}{2.4.6....(2i-2)}$ and

$$a_i = \sum_{k=1}^{k=n} v_k^{2i-3} d_k + \sum_{j=n}^{j=m} v_j^{2i-3} d_j;$$

Substituting the above in (2.2) gives

$$x = \sum_{i=1}^{\infty} q_i a_{i+1} p^{2i-1}$$

Let $b_i = q_i a_{i+1}$, and,

$$x = \sum_{i=1}^{\infty} b_i p^{2i-1} \qquad (2.3)$$

Similarly, letting $g_i = q_i a_i$, we get

$$t = \sum_{i=1}^{\infty} g_i p^{2i-2} \qquad (2.4)$$

Substituting (2.3) and (2.4) in (2.1) and comparing like powers of p^2 gives us the coefficients of the power series in (2.1). Following Taner and Koehler (1969), the coefficients are calculated as follows:

$$c_1 = g_1^{\;2} = q_1 a_1^2 = a_1^2 = [\sum_{k=1}^{k=n} \frac{d_k}{v_k} + \sum_{j=n}^{j=m} \frac{d_j}{v_j}]^2 = t_{0r}^2 \qquad (2.5)$$

where t_{0r} is the zero-offset traveltime for the reflected P-wave arrival to the receiver in the borehole.

Similarly, $c_2 = \dfrac{a_1}{a_2} = \dfrac{\sum_{k=1}^{k=n} d_k / v_k + \sum_{j=n}^{j=m} d_j / v_j}{\sum_{k=1}^{k=n} d_k v_k + \sum_{j=n}^{j=m} d_j v_j} = \dfrac{1}{(\bar{v})^2}$ (2.6)

where $\bar{v}$ can be defined as the *rms* velocity for the reflected P-wave arrival with respect to the nth reflector at the particular receiver depth.

We can derive other coefficients as well, however, a two-term truncation suffices, as evidenced later in this thesis. Therefore, the traveltime-distance relationship for the reflected P-wave arrivals at a receiver in a borehole can be written in the hyperbolic form

$$t^2 = t_{0r}^2 + \frac{x^2}{(\bar{v})^2}. \tag{2.7}$$

Similarly, for direct arrivals at the receiver we find

$$c_1 = [\sum_{j=1}^{j=m-1} \frac{d_j}{v_j}]^2 = t_{0d}^2 \tag{2.8}$$

where t_{0d} is the zero-offset traveltime for the direct arrival to the receiver in the borehole.

Furthermore, $c_2 = \frac{\sum_{j=1}^{j=m-1} d_j / v_j}{\sum_{j=1}^{j=m-1} d_j v_j} = \frac{1}{(\bar{v})^2}$ (2.9)

where $\bar{v}$ is the *rms* velocity for the direct arrival at the receiver.

Thus, a two-term truncation of the power series expansion for direct arrivals gives the hyperbolic *t*-*x* relationship

$$t^2 = t_{0d}^2 + \frac{x^2}{(\bar{v})^2} \tag{2.10}$$

Tessmer and Behle (1988) showed that a hyperbolic approximation to traveltimes can be used for converted-wave arrivals on the surface. Since in the VSP, asymmetry in the raypath is common to both pure P-wave and converted-wave arrivals, we simply extend the formula for pure P-wave arrivals (Equation 2.7) to the converted-wave arrivals in the VSP to give the relation

$$t^2 = t_{0PS}^2 + \frac{x^2}{(\overline{v_{PS}})^2} \tag{2.11}$$

where t_{0PS} is the zero-offset traveltime to the borehole receiver for the converted-wave reflection. $\overline{n_{PS}}$ is the corresponding *rms* velocity given by

$$c_2 = \frac{a_1}{a_2} = \frac{\sum_{k=1}^{k=n} d_k / v_k + \sum_{j=n}^{j=m} d_j / b_j}{\sum_{k=1}^{k=n} d_k v_k + \sum_{j=n}^{j=m} d_j b_j} = \frac{1}{(\overline{n_{PS}})^2} \tag{2.12}$$

b_j is the shear-wave velocity of the *j*-th layer.

The convergence properties of the traveltime expansions are the same as discussed in Al-Chalabi (1973).

2.2.2 VSP moveout correction method

Unlike surface recorded signals, the locus of reflection points for each source-receiver pair in VSP surveys depends on reflector depth. It tends towards the source-receiver midpoint with increasing depth in a horizontally layered earth (see Dillon and Thomson, 1984 for excellent examples). Therefore, VSP data cannot be sorted simply in the CMP domain as in surface seismic surveys. Also, the RMS velocity (Equation 2.6) for reflected signals in the VSP geometry changes with the receiver depths/locations. This implies that to use the inherent data redundancy, VSP data needs to be sorted in the receiver domain for implementation of a NMO correction method similar to the one used in surface seismic surveys. Figure 2.1 shows the difference between the sorting of surface seismic and VSP data.

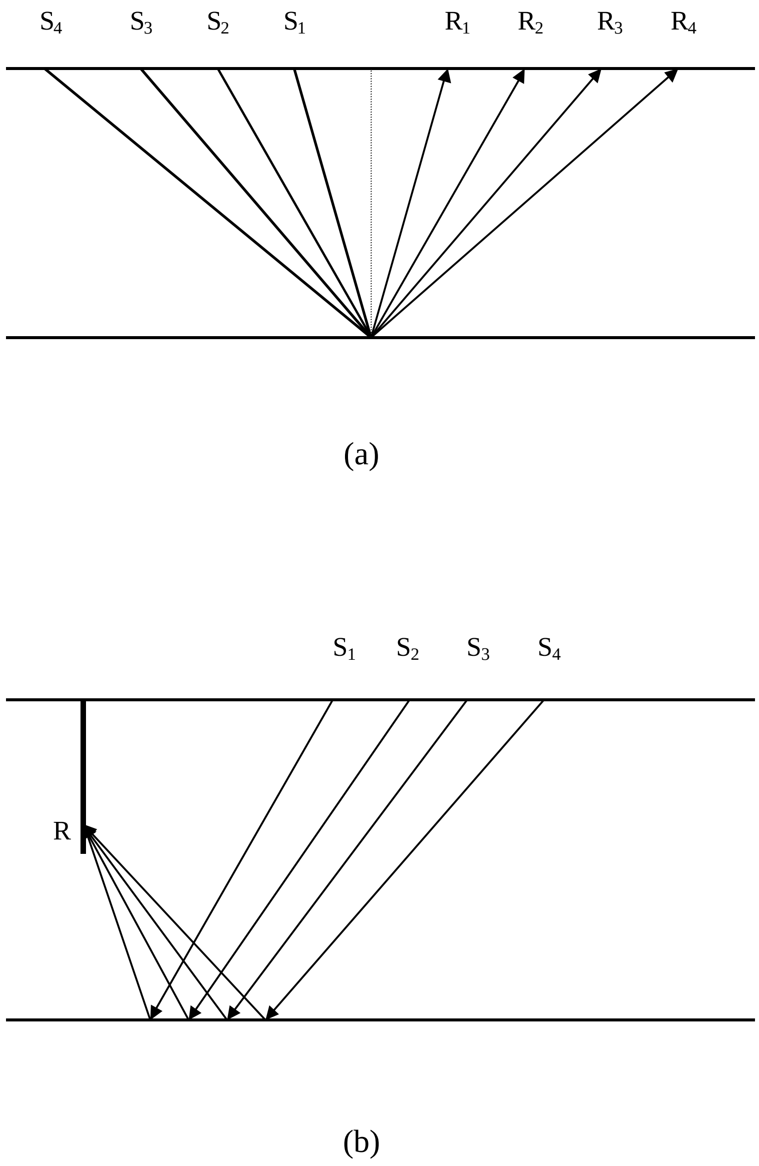

Fig.2.1. (a) Surface seismic data sorted in the CMP domain. (b) VSP data sorted in the receiver domain.

2.2.2.1 Moveout correction of pure P-wave arrivals

After the vertical component data are sorted into the receiver domain, Equation (2.10) is used on the first-break picks to get the zero-offset time of the direct arrivals (t_{0d}). Further, amplitude semblance analysis (see Taner and Koehler, 1969 for details) of the reflected arrivals based on Equation (2.7) gives the zero-offset time (t_{0r}) for each of the reflected arrivals in the sorted data. The quantities t_{0d} and t_{0r} are then added to obtain the normal incidence time of the reflected arrivals. Figure 2.2 shows the steps followed in correcting the reflected arrivals to normal incidence time.

2.2.2.2 Moveout correction of converted-wave arrivals

To correct converted waves to normal incidence P-S times in a manner similar to the procedure outlined in Figure 2.2, one would need the downgoing direct S-wave arrival times. These may be available in the form of S-wave arrivals from P-S transmissions near the surface. When these are not available, one can approximately calculate the zero-offset time for a downgoing S-wave from the P-wave direct arrivals assuming a constant P-wave/S-wave velocity ratio. Equation 2.11 is then used to calculate the zero-offset time of a converted-wave reflection from amplitude semblance analysis. In Figure 2.6, a schematic diagram is shown to correct the converted-wave arrivals to approximate normal incidence P-S times using P-wave direct arrivals.

2.2.2.3 Synthetic results of the moveout correction methods

Raytracing was used to generate synthetic P-wave traveltimes for a model (Figure 2.3). Traveltimes were calculated for borehole receivers placed at depths 400m and 910m with source offsets varying from 50m to 1950m. These times were calculated for the model with maximum depth of reflection being 2000m. Figure 2.4 shows the traveltimes of the

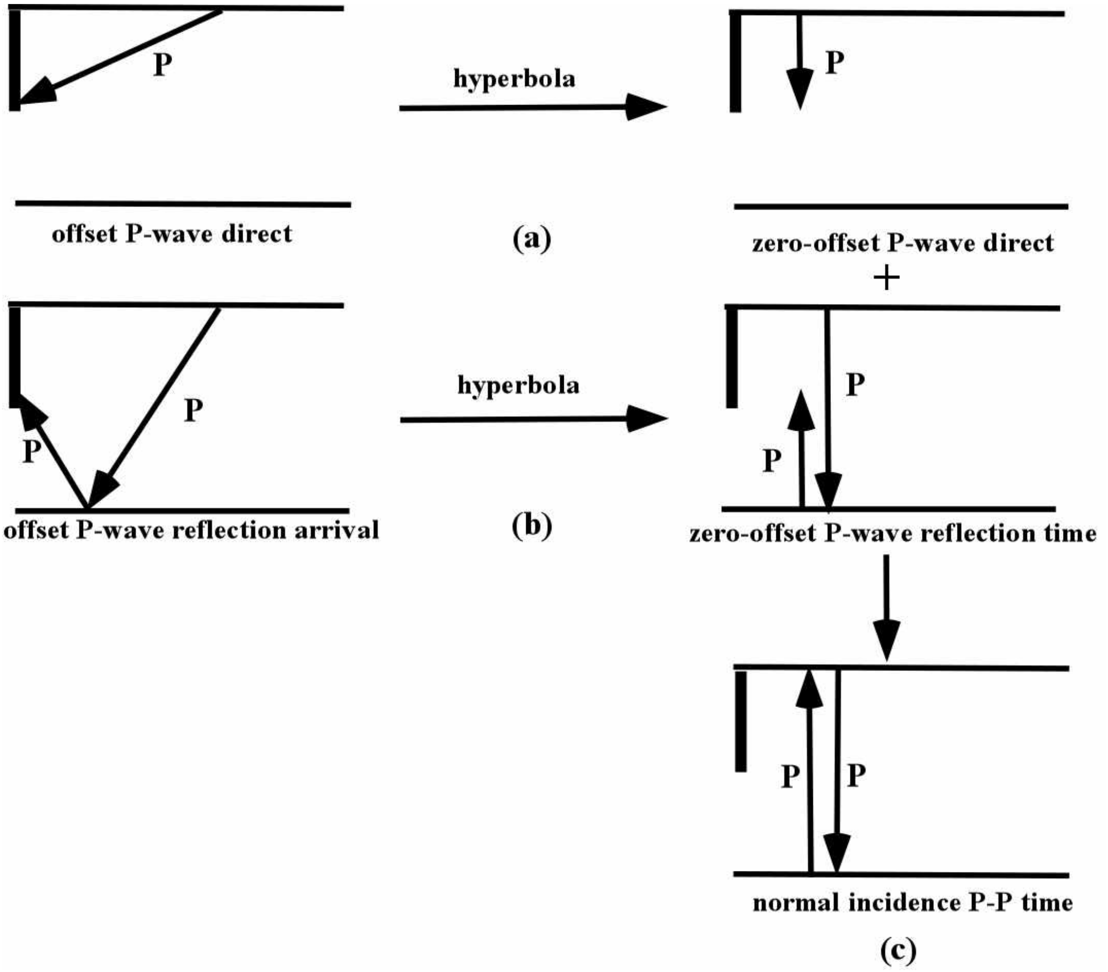

Fig.2.2. Method to calculate the normal incidence time of VSP reflections. (a) Calculate the zero-offset time of the direct arrivals using Equation 2.10. (b) Calculate the zero-offset time of P-wave reflections using Equation 2.7 (c) Normal incidence time of the P-wave reflections is then obtained by adding quantities obtained from (a) and (b).

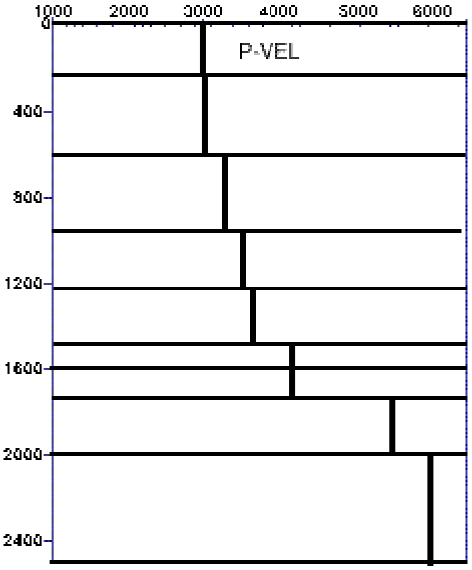

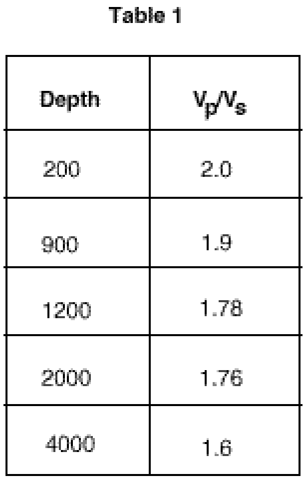

Table 1

Depth	V_p/V_s
200	2.0
900	1.9
1200	1.78
2000	1.76
4000	1.6

Fig.2.3. Elastic model used to generate P-P and P-S traveltimes for borehole geometries (from Zhang et al., 1996)

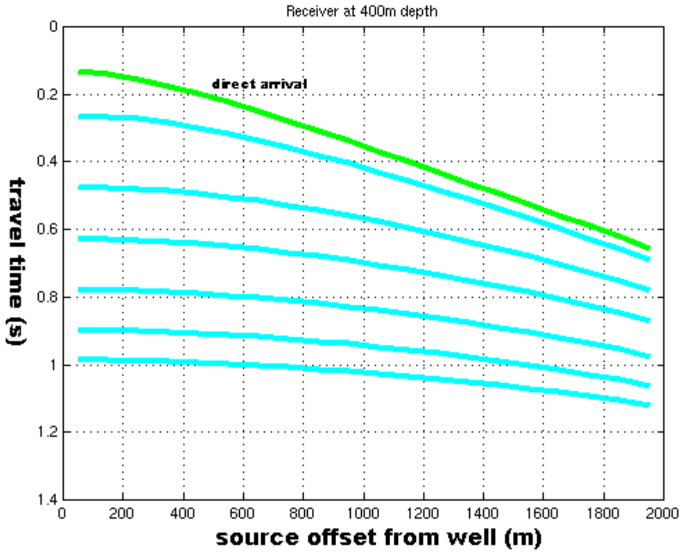

Fig.2.4. Traveltimes for direct and reflected P-wave arrivals for borehole receiver at a 400m depth of the model in Figure 2.3.

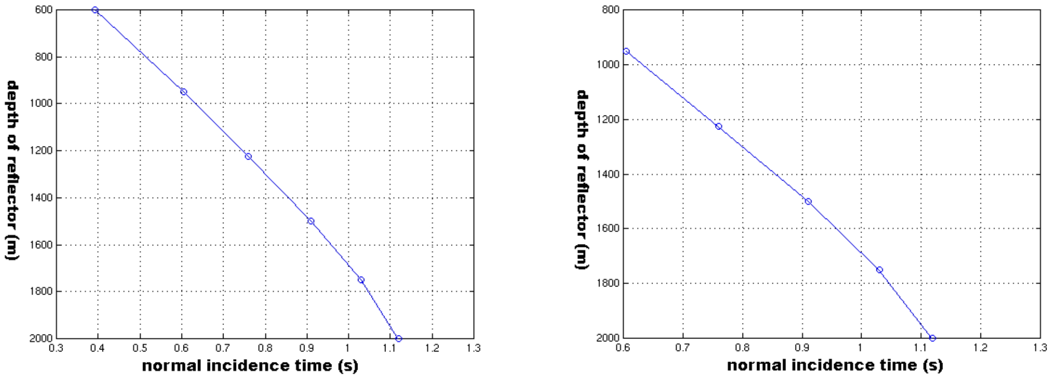

(a) Normal incidence times for receiver depth at 400m.

(b) Normal incidence times for receiver depth at 910m.

Fig.2.5. Normal incidence times estimated after semblance analysis match remarkably well with the actual times. Circles indicate the times estimated from the method in Figure 2.2 where the line passing through these are the actual times.

P-wave reflected arrivals for the model with borehole receiver at 400m depth; the first event representing the P-wave direct arrival. Following the steps outlined above, normal incidence times (Figure 2.5) for reflection events were determined for both receiver depths. To simulate amplitude semblance analysis, a least-squares solution to the traveltimes was used to calculate the normal incidence time. The estimated times match remarkably well with the true zero-offset times, with maximum error being less than 2ms.

Next, synthetic converted-wave traveltimes were used to test the method for converted-waves. The synthetic converted-wave traveltimes were generated for the same model (Figure 2.3) using raytracing for the same source-receiver geometry. Following the steps outlined in Figure 2.6, normal incidence P-S times were determined for converted-waves assuming a V_P / V_S ratio of 1.75 (Figure 2.7). Times estimated using the method in

Figure 2.6 match well with actual calculated times, the maximum error being less than 7ms.

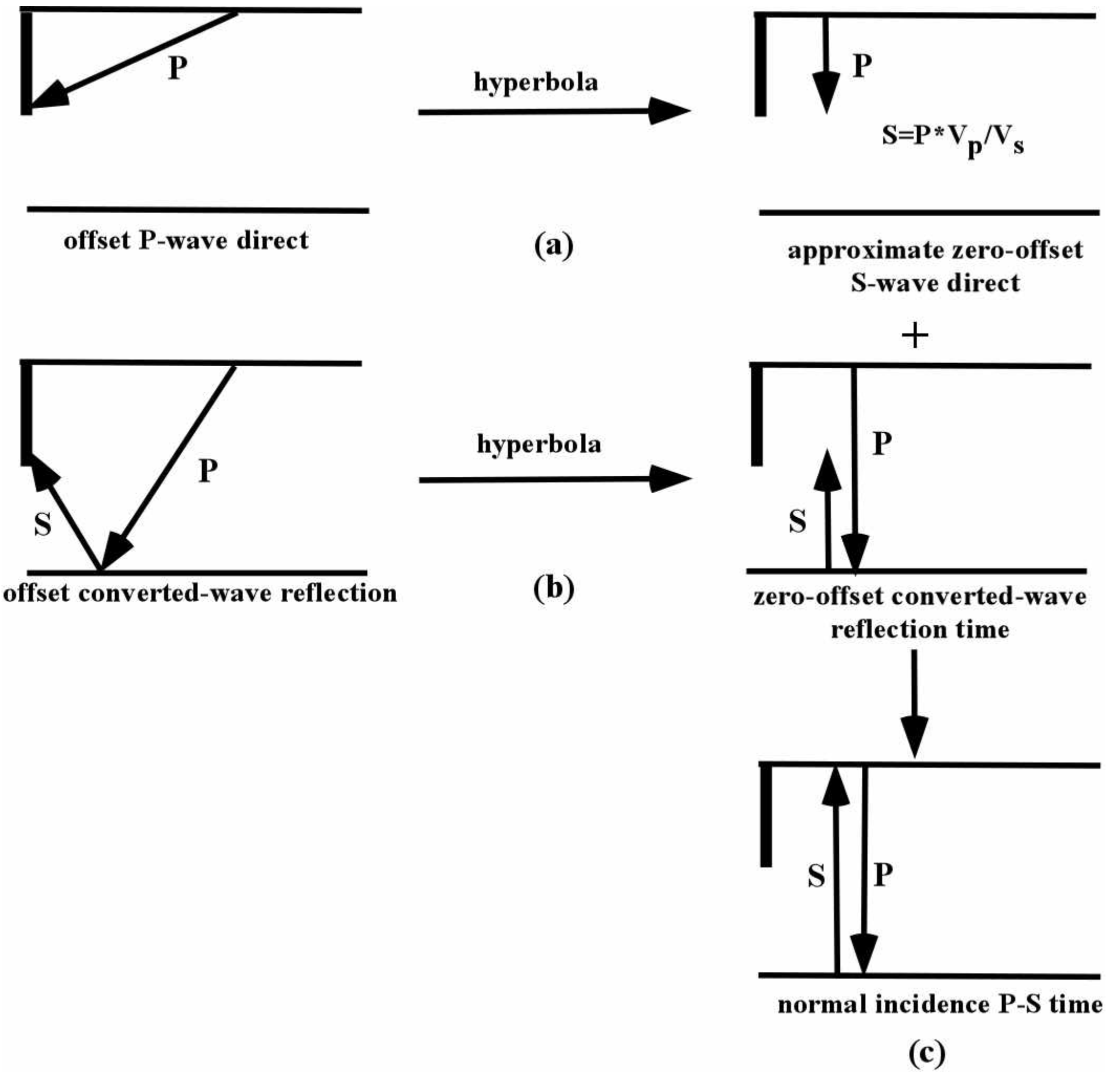

Fig.2.6. Method to calculate the normal incidence time of VSP reflections. (a) Calculate the zero-offset time of the direct arrivals using Equation 2.10. Multiply it by an assumed V_P/V_S to get approximate zero-offset time of a downgoing S-wave. (b) Calculate the zero-offset time of converted-wave reflections using Equation 2.11. (c) Normal incidence time of the converted-wave reflections is then obtained by adding quantities obtained from (a) and (b).

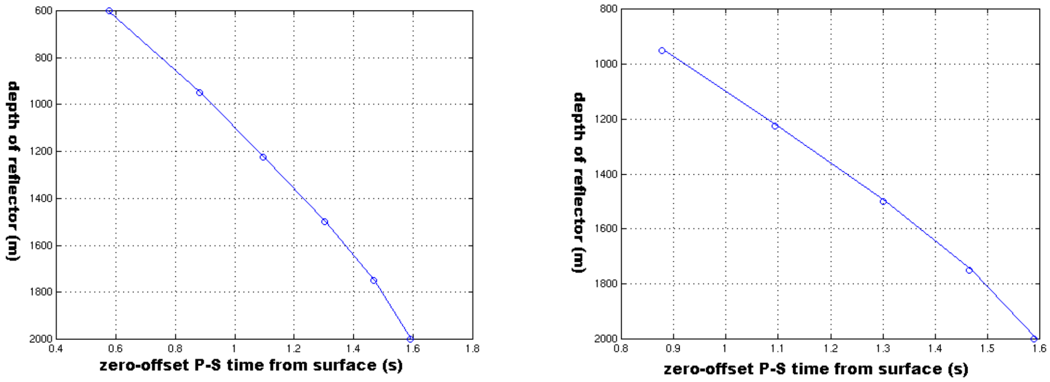

(a)Normal incidence P-S times for receiver depth at 400m.

(b)Normal incidence P-S times for receiver depth at 910m.

Fig.2.7. Normal incidence P-S times estimated after semblance analysis match remarkably well with the actual times. Circles indicate the times estimated from the method in Figure 2.6 where the line passing through these are the actual times.

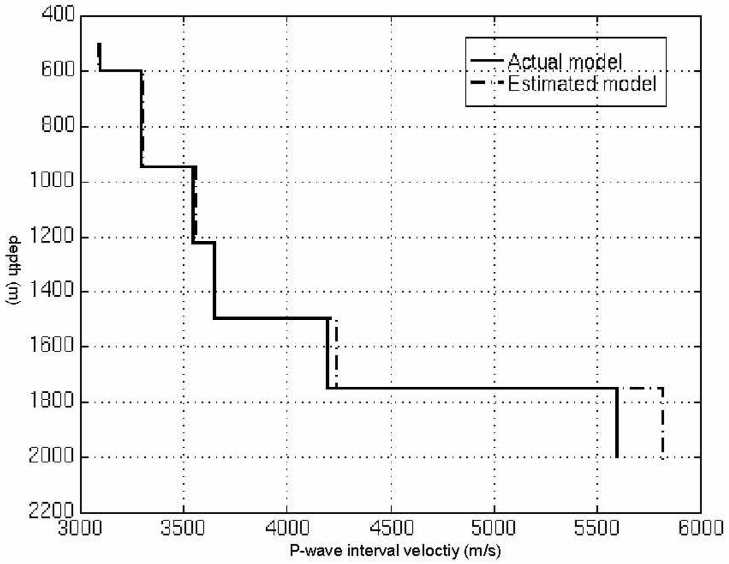

Fig.2.8. Dix estimates of the model compared with the actual model.

2.3 Dix interval velocities from VSP data

Equation 2.9 results in the same formula $v_n = \sqrt{\dfrac{\bar{v}_{n+1}^2 t_{n+1} - \bar{v}_n^2 t_n}{t_{n+1} - t_n}}$ for the P-wave interval velocity as in Dix (1955). Estimates of interval velocities obtained during moveout correction of the synthetic P-P traveltimes are compared with the actual model (Figure 2.8). The estimated velocity-depth model using the Dix formula is very close to the actual model despite the assumption of stacking velocities being equal to the RMS velocities. When events are closely spaced in time, the estimates deviate more from the actual values as observed in the case of the last two events.

2.4 VSPCDP mapping

The advantage of doing the NMO correction of VSP data using the method described in previous sections is that it does not require a model. However, standard procedure for VSPCDP mapping involves raytracing through a model to map the spatial locations of reflections. In such a case, methods that use information obtained from semblance analysis are required to map the reflection points. Approximate mapping methods such as in Stewart (1985) and Stewart (1991) are easily adapted to serve the above purpose and are shown in the following section.

2.4.1 VSPCDP mapping equations

The offset x_B of the reflection point from the well for a P-wave arrival over a homogeneous single-layered earth is given in Stewart (1985) as

$$x_B = \frac{x}{2}[\frac{vt_v - 2z}{vt_v - z}] \tag{2.13}$$

where x, v, t_v, z are the source-receiver offset, constant velocity of the homogeneous single-layered medium, normal incidence time of reflection and depth of the receiver respectively. Equation 2.13 which is valid for a single-layered is adapted to a multi-layered earth by simply substituting the stacking velocity $\bar{v}$ (assumed equal to RMS velocity) in place of the constant velocity v.

Another formula that can be used for mapping both P-wave and converted-wave reflections is given in Stewart (1991) as

$$x_B = \frac{x}{1 + \frac{\bar{V}_D^2\, t_{oD}}{\bar{V}_U^2\, t_{oU}}} \tag{2.14}$$

where $\bar{V}_D, \bar{V}_U$ are the RMS velocities, and t_{oD}, t_{oU} are the zero-offset time for the downgoing and upgoing waves respectively.

The quantities in the denominator in Equation 2.14 can be determined as

$$\bar{V}_D^2\, t_{oD} = \bar{V}_d^2\, t_{od} + \frac{\bar{V}_r^2\, t_{or} - \bar{V}_d^2\, t_{od}}{1 + 1/\gamma} \tag{2.15}$$

where t_{or} and t_{od} are the zero-offset times, and $\bar{V}_r$ and $\bar{V}_d$ are the RMS velocities for the reflected and direct wave respectively. These values are obtained during NMO correction of VSP data using the method discussed in the previous sections. γ is the P-wave to S-wave interval velocity ratio and is assumed to be a constant for the entire model. $\gamma = 1$ in the case of P-wave reflections.

The other quantity in Equation 2.14 is then determined as

$$\overline{V}_U^2 \, t_{oU} = \overline{V}_r^2 \, t_{or} - \overline{V}_D^2 \, t_{oD} \tag{2.16}$$

2.4.1 VSPCDP mapping of P-wave reflections

Synthetic traveltimes from previous sections are used for testing the accuracy of the approximate methods. For comparison, reflection points were mapped using a 2-D raytracing and both of the approximate mapping procedures. Stacking velocities and normal incidence times for P-wave reflections obtained from moveout correction of the P-wave synthetic traveltimes are used in the calculations.

From Figure 2.9, we observe that the approximate reflection points at small source offsets are accurate when compared to those obtained from raytracing. Even at a large offset of 1950m, the approximate mappings are reasonable relative to bin size. Figure 2.10 displays the reflection point maps for all source-receiver offsets for reflections recorded at receiver depths of 400m and 850m respectively. It can be seen that the accuracy of the approximate methods decreases with increasing offset and receiver depth. However, in a VSP the maximum source offset is usually equal to the depth of the reflector of interest. Within this limit, the mapping methods are as good as raytracing for the simple earth model of Figure 2.3. Therefore, in a simple geology the final image will nearly be the same using either of the mapping methods.

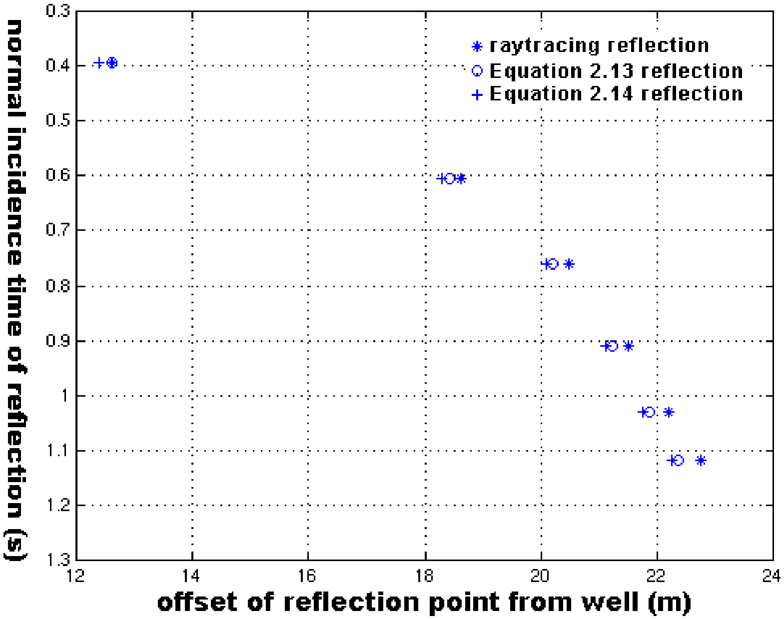

(a) Source at 50m offset

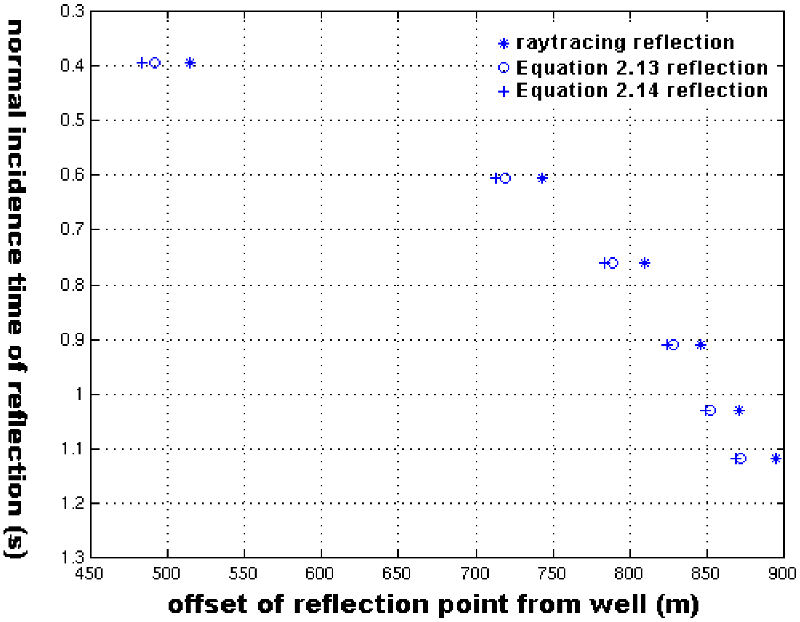

(b) Source at 1950m offset

Fig.2.9. Comparison of mapped reflection points for P-wave reflections using raytracing and approximate mapping methods for borehole receiver at 400m depth.

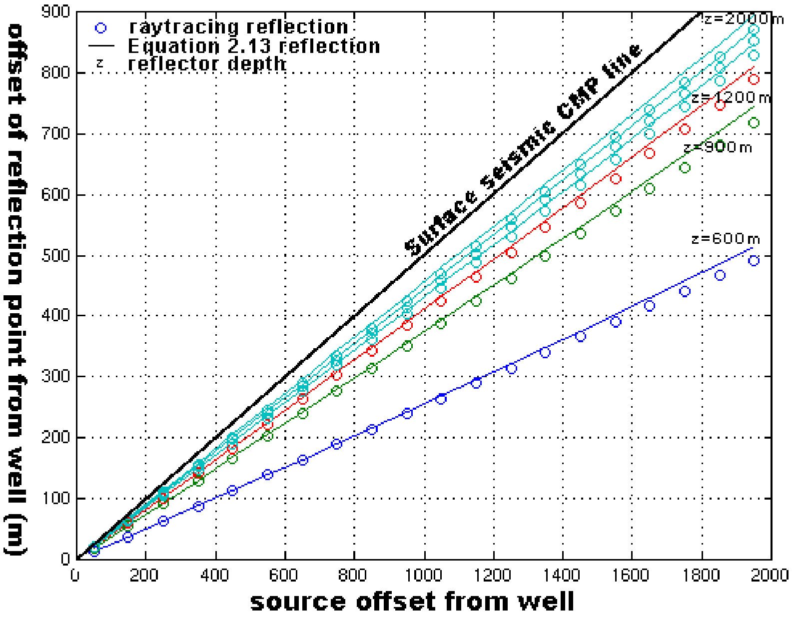

(a) Receiver at 400m depth in borehole.

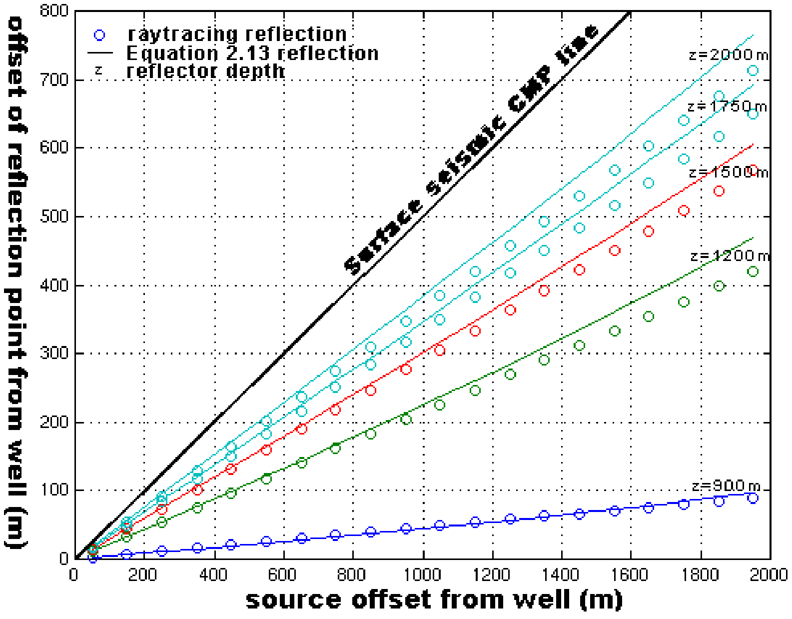

(b) Receiver at 850m depth in borehole.

Fig.2.10. Comparison of mapped reflection points using both raytracing and the approximate method using Equation 2.13 for model in Figure 2.4. Source offsets range from 50-2450m with borehole receivers at (a) 400m and (b) 850m depth.

2.4.2 VSPCCP mapping of converted-wave reflections

Equations 2.14-2.16 are used for mapping the converted-wave reflection points. Synthetic converted-wave traveltimes computed in previous sections were used for testing the accuracy of the mapping method. Stacking velocities and zero-offset times used in the equations were obtained from amplitude semblance analysis of the converted-wave synthetic. Values around $\gamma = 2.0$ for the model resulted in reflection points closest to that obtained from raytracing. These are shown and compared with reflection maps obtained from raytracing (Figure 2.11). The average and time-weighted average γ values for the synthetic traveltimes was found to be 1.81 and 1.79 respectively. From this, it appears that γ values slightly higher than the average or a time-weighted average should be used in the computation of the approximate reflection maps.

From Figure 2.11, we observe that the approximate reflections are again accurate at small source offsets when compared to those obtained from raytracing. However, at the far offset of 1950m, the approximate mappings have large errors at shallow depths which decreases with increasing depth of the reflectors. Figure 2.12 displays the reflection point maps for all source-receiver offsets for reflections recorded at receiver depths of 400m and 850m respectively. The increase in accuracy with reflector depth is due to a larger P-wave leg in the converted-wave reflection and also on effective smaller source offset-to-depth ratio. We observe that application of the mapping equation to converted-waves is restricted to the zone where the lateral movement of the reflection point is a linear function of the source offset.

Reflection maps were also calculated for a range of γ values for studying the effect of errors in the γ value (Figure 2.13). The errors in the figure are relative to the reflection map for $\gamma = 2.0$ value, assuming that in a particular area this value gives reflection maps closest to those obtained from raytracing. It can be seen that even small errors in γ values result in high errors. It appears that it would be more appropriate to use raytracing than an approximate equation for VSPCCP mapping.

2.5 Post-VSPCDP stack migration

Methods discussed in the above sections assumed a simple stratified earth model. Limitations of reflection mapping methods discussed in the previous sections for dipping layer earth models are well-known. It should also be noted that for the VSP geometry in the dipping layer case, solving for the hyperbola for zero-offset time is not equivalent to solving for normal incidence time. In surface seismic surveys, both zero-offset and normal incidence times are considered equivalent. Moreover, the VSPCDP stacking methods are not capable of collapsing diffractions.

This would mean unfocussed fault edges, incorrect dips, and therefore, misinterpretations. In the case of surface seismic data, the conventional approach to handle diffractions is to use a post-stack migration routine using the exploding reflector model (Loewenthal et al., 1976). In the VSP, however, the asymmetry of raypaths and subsequent VSPCDP stack are believed to complicate diffraction patterns on the stacked section.

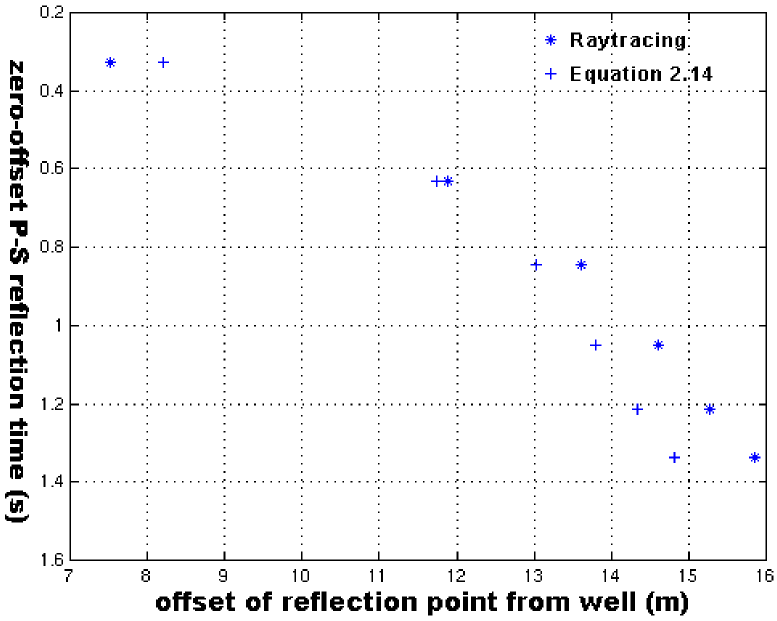

(a) Source at 50m offset

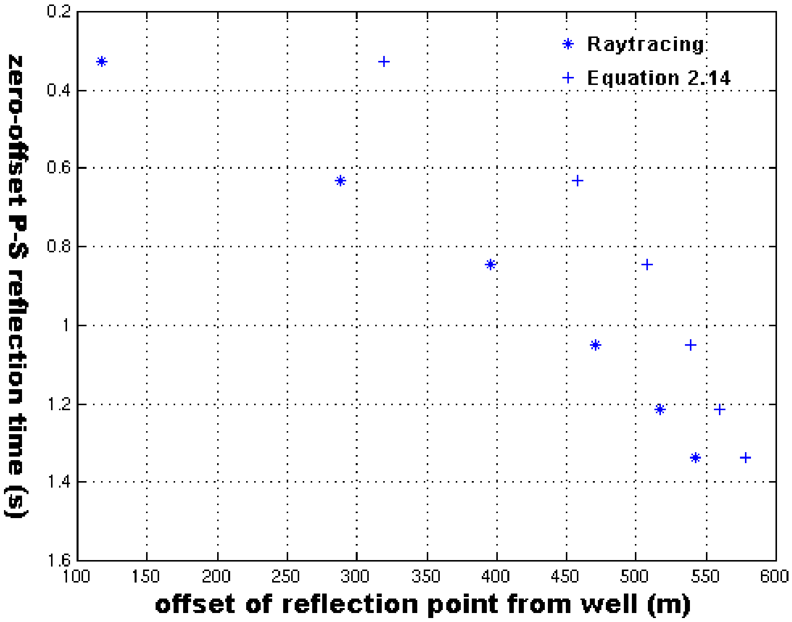

(b) Source at 1950m offset

Fig.2.11. Comparison of mapped conversion points for converted-wave reflections using raytracing and Equation 2.14 for borehole receiver at 400m depth.

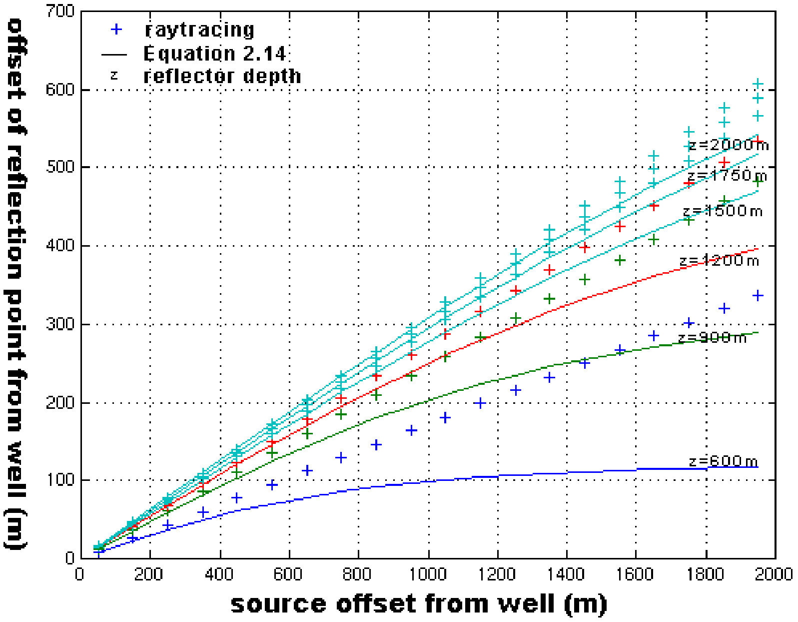

(a) Receiver at 400m depth in borehole.

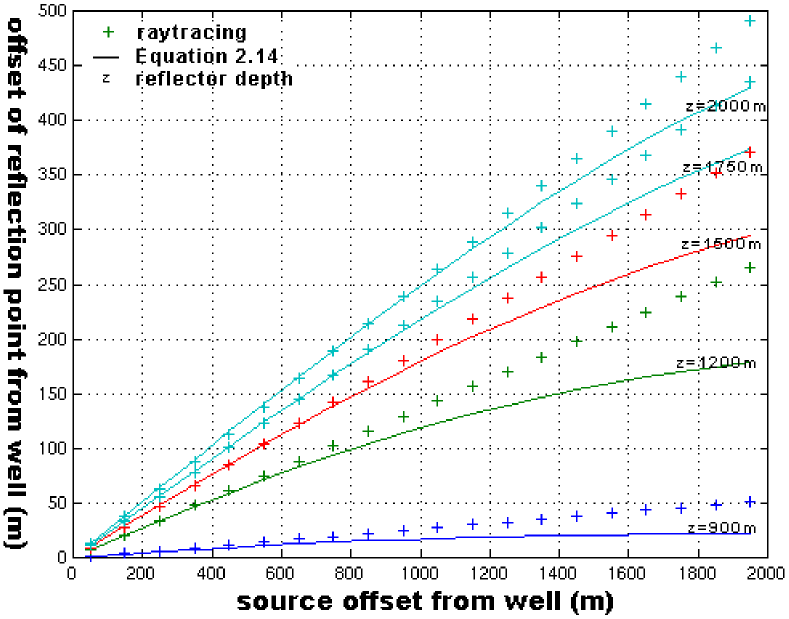

(b) Receiver at 850m depth in borehole.

Fig.2.12. Comparision of mapped conversion points using both raytracing and the approximate method using Equation 2.14 for model in Figure 2.4. Source offsets range from 50-2450m with borehole receivers at (a) 400m and (b) 850m depth.

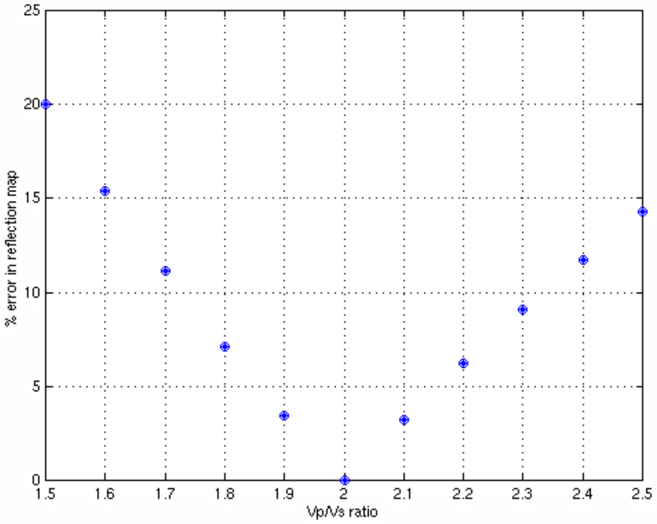

Fig.2.13. Comparison of reflection map errors using the converted-wave mapping equation with a range of γ values.

Thus, data acquired in a VSP geometry is usually migrated before stack using methods such as those discussed in Chang and McMechan (1986), Kohler and Koenig (1986), and Whitmore and Lines (1986). If diffractions on VSPCDP stack do not have a regular pattern, then it may be advantageous to an interpreter. On the other hand, if they do follow a certain pattern then it would be worthwhile to investigate if surface seismic migration routines can be used to enhance interpretation. The problem is analogous to post-stack converted data recorded on the surface of the earth and is discussed in the following sections.

2.5.1 Diffractions on VSPCDP stacked data

Consider the VSP geometry in Figure 2.14 where a specular reflection occurs at a distance x_c and a diffraction at a further distance R from it. The traveltime t_r for the specular reflection is then given by the double square-root equation as

$$t_r = \frac{1}{v}\left\{\left[D^2 + (x - x_c)^2\right]^{1/2} + \left[(D - z)^2 + x_c^2\right]^{1/2}\right\}$$

which can be written as

$t_r = \frac{1}{v}\left\{\left[D^2 + (x - x_c)^2\right]^{1/2} + \left[D^2 + (z^2 - 2Dz) + x_c^2\right]^{1/2}\right\}$. Assuming that the moveout contributions are small compared to normal incidence time, the traveltime can approximately be written as

$$t_r = \frac{1}{v}\left\{ D\left[1 + \frac{(x - x_c)^2}{2D^2}\right] + D\left[1 + \frac{z^2 - 2Dz + x_c^2}{2D^2}\right]\right\},$$

i.e.,

$$t_r = \frac{2D}{v} + \left(\frac{z^2 - 2Dz}{2Dv} + \frac{(x - x_c)^2}{2Dv} + \frac{x_c^2}{2Dv}\right). \qquad (2.17)$$

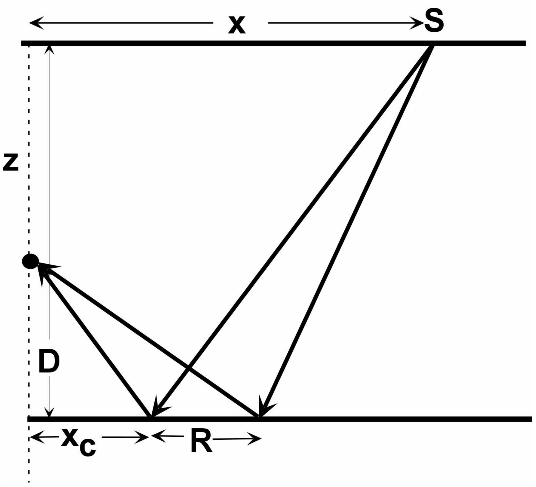

Fig.2.14. Reflection and diffraction arrivals in a VSP geometry.

The traveltime for the diffraction in the figure is given by

$$t_d = \frac{1}{v}\left\{\left[D^2 + (x - x_c - R)^2\right]^{1/2} + \left[(D - z)^2 + (x_c + R)^2\right]^{1/2}\right\}. \tag{2.18}$$

By repeating the same procedure as in the previous case, the diffraction traveltime can be approximated to

$$t_d = \frac{2D}{v} + \left(\frac{z^2 - 2Dz}{2Dv} + \frac{(x - x_c)^2}{2Dv} + \frac{x_c^2}{2Dv}\right) + \frac{R^2}{Dv} + \frac{1}{Dv}(2x_c - x)R \tag{2.19}$$

From Equations 2.17 and 2.19, the residual time t_d^r for the diffraction after NMO correction is

$$t_d^r = \frac{2D}{v} + \frac{R^2}{Dv} + \frac{1}{Dv}(2x_c - x)R \tag{2.20}$$

Now let us consider two extreme cases. First consider the case in which the receiver is closer to the reflector such that $z \to D$ and, therefore, $x_c << x$. Then $t_d^r \approx \frac{2D}{v} + \frac{R^2}{Dv} - \frac{xR}{Dv}$ and thus the diffraction residual is dependent on the geometry as well. Some sort of pre-stack operator would, therefore, be required so as to apply a standard migration routine on stacked VSP data.

Now consider the case in which the receiver is closer to the surface than to the reflector such that $0 < z << D$. In such a case, the reflection point would tend towards the mid-point of source-receiver offset i.e. $x_c \to x/2$. Therefore, $t_d^r \approx \frac{2D}{v} + \frac{R^2}{Dv}$. Squaring and neglecting the term raised to the power of four results in the familiar hyperbola relation for the surface seismic and given as

$t_d^{r^2} \approx \frac{4D^2}{v^2} + \frac{4R^2}{v^2}$. Thus, standard surface seismic migration routines could be applied to a VSPCDP stacked section under the above limitation.

2.5.2 Synthetic example on post-VSPCDP stack migration

We saw the limitations of applying a migration operator to a VSPCDP stacked section in the previous section. Nonetheless, valuable information could be obtained if the data could be migrated with reasonable success. This information could then provide additional knowledge for building the velocity-depth model for pre-stack depth migration. Synthetic data are tested to evaluate the performance of a post-stack migration operator on VSPCDP stacked data.

Kirchhoff diffraction modelling was used to generate synthetic P-P data for the model shown in Figure 2.15. Five borehole receivers were placed at depths between 400-460m every 15m. The shot interval was 15m and shot offsets from the well ranged from 5-1500m. Diffractions from the fault edges at A, C and D can be seen on the receiver gathers (Figure 2.16). Diffractions from zone B are not visible as they interfere with reflection arrivals from the reflector at about 1600m depth. A VSPCDP stack from the entire dataset was obtained following the procedure outlined in the previous sections (Figure 2.17). One can observe that diffractions also stack and have a hyperbola-like moveout. A post-stack Kirchhoff migration was then applied to the VSPCDP stacked data using moveout velocities obtained from receiver gather at 430m depth (Figure 2.18). The post-stack migration has significantly collapsed the diffractions and the fault edge is more visible. Due to the robustness of post-stack time migrations, varying the velocities by 10% did not result in significant change in the final migrated section shown in the figure. Comparing the result with raytracing reflections in Figure 2.19, one could infer that post-stack migration did not correctly position the reflections. This is expected as the above process is a further approximation to the normal application of post-stack migrations to surface seismic data.

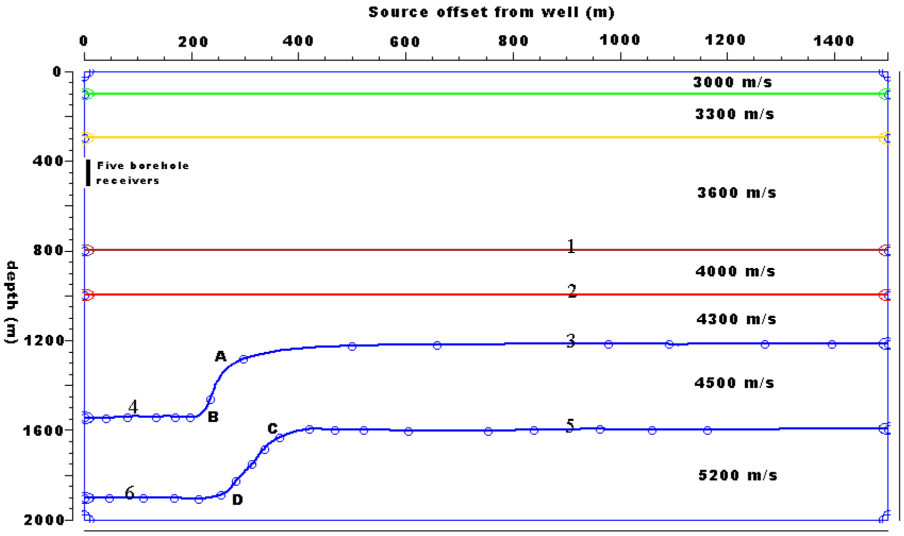

Fig.2.15. Model used for generating synthetic data by Kirchhoff diffraction modelling.

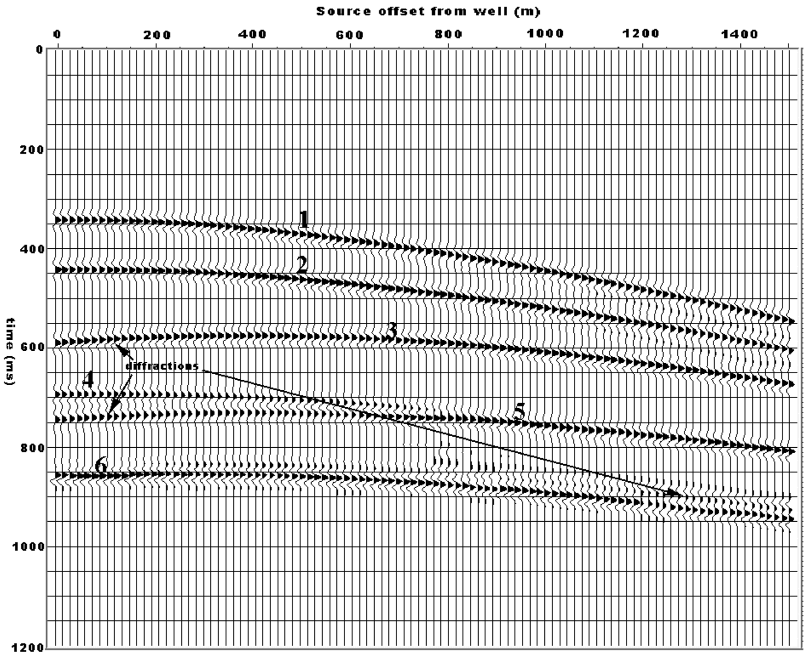

Fig.2.16. Diffractions from the fault edges can be seen along with reflections from the layers for receiver gather at depth 400m. Direct arrivals are not shown in the figure.

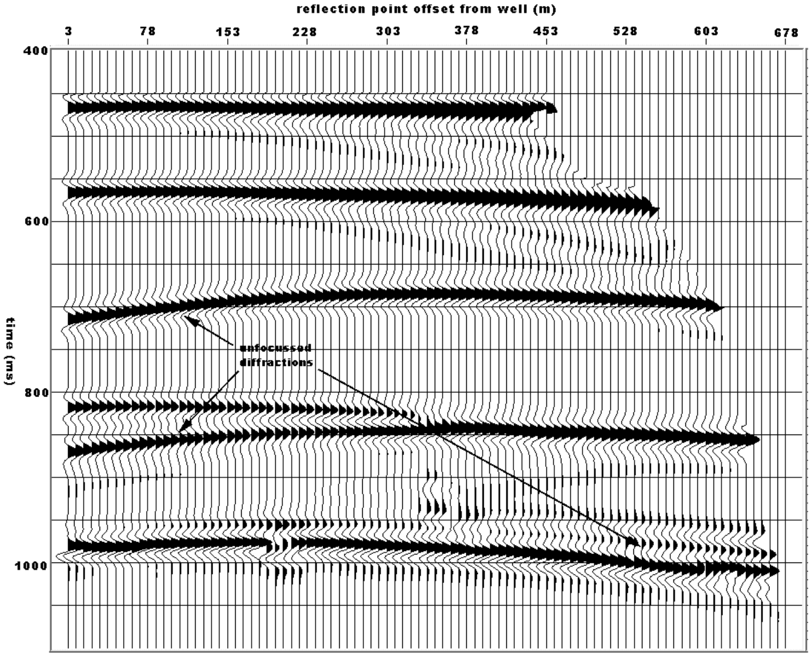

Fig.2.17. VSPCDP stack of synthetic data. Diffractions from fault edges remain uncollapsed and have a hyperbola-like moveout.

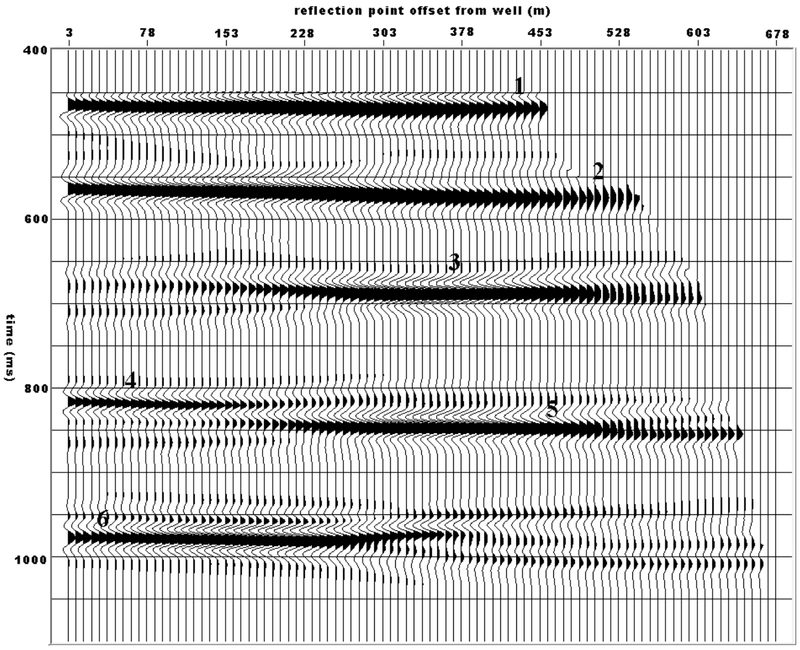

Fig.2.18. VSPCDP stacked data in Figure 2.16 after post-stack Kirchhoff migration.

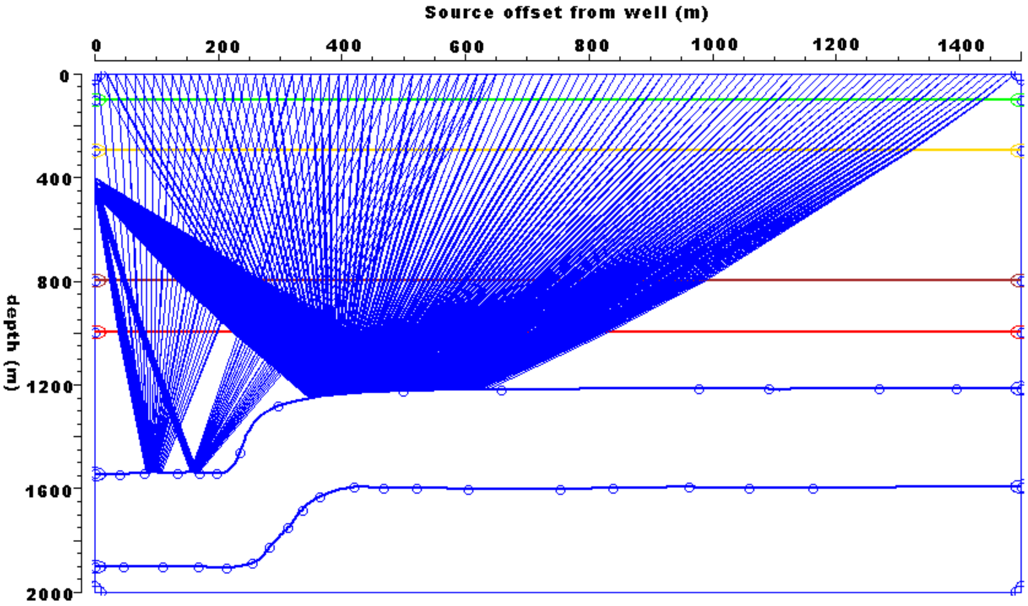

Fig.2.19. Raytracing showing specular reflections from the layer at 1200m depth.

2.6 Conclusions

The traveltime-offset relation for reflections recorded in the VSP geometry can be approximated by a hyperbola. This relation provides a statistical framework to NMO correct VSP data in the receiver domain by using amplitude semblance analysis. The method is robust and accurately corrects VSP data to normal incidence time for a horizontally layered earth. Moveout correction using semblance analysis is easier to use compared to raytracing especially in the 3-D context where the data volume is large.

VSPCDP mapping of P-wave arrivals based on an approximate mapping method gives reasonably accurate reflection maps when compared to the raytracing method. However, raytracing is the preferred option when mapping converted-wave reflections.

Post-stack migration of VSPCDP stacked data, although theoretically incorrect, could be used keeping in mind the approximations and limitations of such a process. In simple geology, VSPCDP stack followed by post-stack migration may suffice to give a reasonably accurate picture of the geology around the borehole.

The methods developed for VSP acquisition are an efficient way to obtain 2-D or 3-D seismic images in simple geology. In complex geology, however, they could precede more accurate imaging methods like pre-stack depth migration to give additional information about the geology.

CHAPTER 3: 3C-3D VSP IMAGING: THE BLACKFOOT EXPERIMENT

3.1 Introduction

As discussed in Chapter 1 and from Stewart and Gulati (1997), we know that borehole seismic surveys have a long history of providing rock properties such as interval velocity, impedance and attenuation near the borehole. These surveys have also assisted surface-seismic interpretation through time-to-depth values and the provision of a zero-phase reflectivity that is largely multiple-free. These results are basically one-dimensional within a Fresnel zone near the borehole.

With the advent of offset source positions, techniques were developed to obtain a structural image from VSP data (Wyatt and Wyatt, 1984; Chang and McMechan, 1986, Whitmore and Lines, 1986). These produced credible 2-D sections. While valuable, this 2-D VSP image still had limitations such as suffering from restricted angular coverage per bin, limited total bin fold, and difficulty tying various shot statics and moveout.

The fundamental 2-D limitation in a VSP, and indeed many of the other previously mentioned problems, can be overcome by using an areal distribution of shot points, or in the reverse VSP case an areal distribution of receivers. This allows a 3-D image to be constructed near the borehole.

Interest in 3-D well seismic data led to investigations of the feasibility and advantages of using the 3-D VSP geometry. Chen and McMechan (1992) used a pre-stack depth migration algorithm and synthetic 3-D reverse VSP data to investigate imaging of salt structures. They found that 3-D imaging provided imaging of dips and structures not normally accessible to surface surveys. Sun and Stewart (1994) used raytracing over a dome model in a synthetic 3-D reverse VSP and found that converted-waves provided significant coverage of the dome compared to compressional waves. Clochard et al. (1997) used pre-stack migrations and showed the ability of 3-D VSP to image complex structures.

Early 3-D VSP surveys included those conducted by AGIP in 1986 in Brenda field and the 1989 Ekofisk 3-D VSP by Phillips Petroleum group of companies (Dangerfield, 1996). Subsequent to these, several more 3-D VSPs have been shot. Shekhtman et al. (1993) outlined a land VSP where they used vibrators over an area and a 3-level VSP tool to construct a 3-D image. Shell, UK shot a 3-D VSP over the Brent field, North Sea in 1993 for optimizing the development of the field (Van der Pal et al., 1996). The Ekofisk reservoir was revisited and more 3-D VSPs were shot over the field (Farmer et al., 1997; Omnes and Clough, 1998). Fairborn and Harding, Jr. (1996) showed a case in Louisiana of using a downhole vibratory source and a surface spread of receivers to reconstruct a 3-D tomographic image of a sinkhole. A CREWES-supported group shot a 3-D VSP over the Blackfoot field in 1995 simultaneously with a surface 3C-3D survey. The main goal was to assess the 3-D VSP capability for improved delineation of a Glauconitic sand-channel (Stewart and Zhang, 1996). Recently, a 3-D VSP was shot over BP's Magnus field to improve structural interpretation of the field (First Break, 1997).

Several authors have analysed 3-D VSP data processing. Sun and Stewart (1994) proposed a processing flow that included common receiver and common shot gathering, statics removal, binning, and pre-stack migration. Boelle et al. (1998) describe the whole processing sequence used for processing the Oseberg 3-D VSP data. Zhang et al. (1997) developed rapid moveout correction and VSPCDP mapping methods to process the Blackfoot 3-D VSP survey. Chen (1998), and Chen and Peron (1998) implemented the ray-trace mapping method using 3-D velocity models and applied it to real data. Farmer et al. (1997) used a 3-D tomographic inversion scheme for determining velocities in the depth migration of a 3-D VSP survey over the Ekofisk field. Mittet et al. (1997) used a 3-D elastic reverse time migration scheme and applied it to synthetic and the Oseberg 3C-3D VSP circular shoot. Clochard et al. (1998) showed that elastic depth migration of the Oseberg VSP data with no wavefield separation gave interpretable images consistent with those obtained after wavefield separation. Bicquart (1998) applied Kirchhoff depth migration to two real data examples and obtained images comparable with those from surface 3-D seismic data.

Standard 3-D seismic interpretive techniques have also been applied to the 3-D volume obtained from the 3-D VSP surveys. The 1989 Ekofisk 3-D VSP resulted in a clear image where the surface 3-D had failed (Dangerfield, 1996). The Brent 3-D VSP revealed fault patterns that were more complex and better resolved compared to those from the surface seismic (Van der Pal et al., 1996). Results from an initial 3-D VSP processing flow over the Blackfoot field resulted in an image consistent with that of a 3-D surface seismic survey in the area (Zhang et al., 1997). Farmer et al. (1997) indicate that processing of a later 3-D VSP survey over the Ekofisk field resulted in a vastly improved image of the Ekofisk reservoir. Boelle et al. (1998) observed that the 3-D borehole seismic gave more details within the reservoir formation compared to the surface seismic. These results show the promise of the 3-D VSP and are nicely summarized by Dangerfield's (1996) statement:

> *"3-D borehole profiles should be considered as a working alternative to 2-D borehole profiles since the extra rig time and cost are surprisingly small and the benefits of 3-D are substantial".*

In this chapter, results from the Blackfoot 3C-3D VSP are presented. Initial results from the Blackfoot survey were first presented by Zhang et al. (1997). Since then developments in the processing flow have resulted in an improved image of the channel body in the area and new results presented in this chapter. The following sections give details of the survey from the acquisition to the interpretation stage.

3.2 Acquisition of the Blackfoot 3C-3D VSP

In 1995, a 3C-3D VSP survey was conducted by the CREWES Project by recording an existing 3C-3D surface survey over the Blackfoot field. The Blackfoot field, which is owned by PanCanadian Petroleum Ltd., is located about 15 kilometres southeast of Strathmore in Alberta, Canada. The producing formation within the Blackfoot area is a Lower Cretaceous, cemented glauconitic sand. The sand was deposited as incised channel-fill sediments above Mississippian carbonates (Wood and Hopkins, 1992). The glauconitic sandstone lies at a depth of about 1,500m below surface and is up to 45m thick. The average porosity in this producing sandstone is near 18% and the cumulative production from it throughout southern Alberta exceeds 200 million barrels of oil and 400 BCF gas (Margrave et al., 1998).

The simultaneous monitoring of shots used in the surface 3C-3D program enabled very cost-effective acquisition of the 3-D VSP survey. The objectives of the survey were (i) to see if it was logistically possible, (ii) to develop acquisition and processing procedures for 3-D VSP, and (iii) to determine if the 3-D VSP data could image the channel body.

The downhole recording of the surface shots was acquired in well 100/12-16-023-23W4 (Figure 3.1) using Baker Atlas's 5-level receiver tool. The 3-D VSP recorded 431 source locations, 4 kg. of dynamite in 18 m holes arranged in 12 lines. The 12 north-south shot lines for the 3-D VSP were spaced 210 m apart with a shot interval of 60 m. Only the shots within 2200 m offset from the well were used out of the total 1395 sources acquired in the whole 3C-3D survey. The shot parameters were designed to meet the criteria of the surface survey and were not optimized for the 3-D VSP survey.

Zhang et al. (1997) indicate that it was intended to have the receiver tool deep in the well for near-offset shots to obtain high-resolution coverage of the target near the borehole and good velocity control. The tool would then be moved progressively shallower for far-offset shots to obtain wider sub-surface coverage.

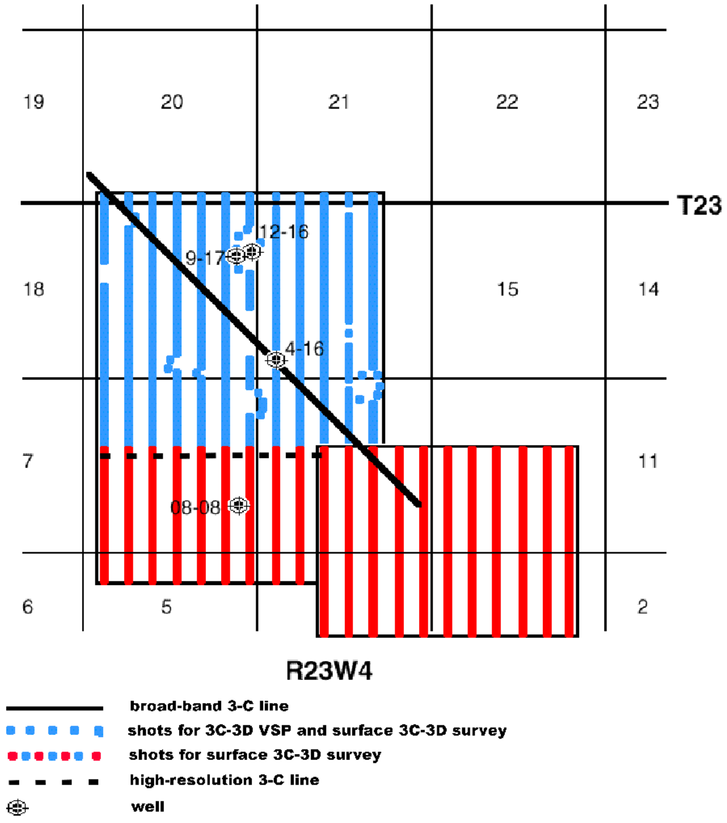

Fig.3.1. Map of the Blackfoot surveys showing shot points for the surface 3C-3D and the 3C-3D VSP. A previous broad-band and a recent high-resolution 3-C line are also shown in the figure (modified from Zhang et al., 1996).

However, field logistics dictated otherwise as the surface shooting used four shooters at variable locations, who fired when ready. It was then decided in the field that the downhole tool would record a minimum of 40 shots before moving to the next interval regardless of source locations. This minimized the number of downhole receiver moves and thus missed shots. Over the course of the survey, the receiver tool was moved seven times (75 m each) to give a receiver depth range from 400m to 910m.

3.3 Processing the 3C-3D VSP data

Initial analysis and processing of the raw data was first performed by Zhang et al. (1996). The results from an improved processing flow are presented here. The first objective of processing the data was to separate the upgoing compressional and shear wavefields. This was followed by mapping of the upgoing P-waves and converted-waves to obtain 3-D images from the survey.

3.3.1 Upgoing compressional and shear wavefield separation

The data were processed by Baker Atlas to obtain the upgoing compressional and shear wavefields. Although the data volume for the entire 3-D VSP survey was small (about 2000 traces per component), processing the data with conventional VSP wavefield separation techniques posed new challenges. Wavefield separation and VSP deconvolution had to be applied with care in lieu of having only 5 levels of receivers for each shot. Figure 3.2 outlines the steps followed by Baker Atlas in processing the raw data to separate the two upgoing wavefields, and is discussed in the following sections.

Figures 3.3a-3.3c show the raw shot gathers for shot at an offset of 372m from the well. Apart from the direct arrivals, it is very difficult to see any events on these gathers. The coupling resonance is seen to be stronger on the two horizontal components compared to the vertical component. This indicates that the VSP sonde carrying the three-component geophones is well coupled vertically but not horizontally for the receiver depths shown in the figures.

After geometry and trace edits, shot statics from the surface 3-D survey were applied to the three-component VSP data. This was followed by hodogram analysis of the two horizontal components (here referred to as H1 and H2) in a small window around the direct arrivals. Hodogram analysis was used to align one of the horizontal components in the direction of the source. The horizontal component aligned in the direction of the source is henceforth referred to as the radial component and the other as the transverse component. Figure 3.3d is the radial component data obtained after hodogram analysis of the H1 and H2 shots gathers of Figures 3.3b and 3.3c respectively. It is interesting to note that the presence of casing resonance is weaker on 910m receiver on the radial component than on the corresponding H2 component. A downgoing wave at about 880ms is also decipherable on the radial component.

The same exponential gain correction was applied to both the vertical and radial component data. The two datasets were time-shifted using first-break arrival times to align downgoing P-waves on both of them. A small median filter of seven traces was then used to separate downgoing P-waves from the data. Next, downgoing converted-waves were separated from the data by using a median filter based on the moveout of the downgoing converted-wave. Figures 3.3e-3.3f show the resultant downgoing and upgoing compressional and shear wavefields. Although downgoing and upgoing events are now visible, wavefield separation has also resulted in upgoing energy leaking onto the downgoing part of the wavefield. Nonetheless, the results are satisfactory considering that there were only five receiver depths for each shot location. Use of a modal filter

(Esmersoy, 1990; Labonte, 1990) would probably give better results than those shown in Figure 3.3.

Upgoing converted-waves and P-waves were then removed from the vertical and radial component data respectively by using a three-trace median filter based on the moveout of the downgoing P-waves. This was followed by a trace-by-trace VSP deconvolution (Kennett et al., 1980) based on the downgoing P-waves in a window of 180ms around the first-breaks to give the P-wave and converted-wave reflectivity traces (Figure 3.4).

From the shot gathers in Figure 3.4, we observe that data on the radial component has larger moveout compared to that on the vertical component data, thereby, indicating effective wavefield separation. The process of obtaining upgoing P-wave and converted-wave reflections was carried out either on a trace-by-trace basis or in shot gathers. So in this context, it is important to verify the results by making some observations on receiver gathers of the data (Figures 3.5-3.7). As the data on each component is a superposition of several wavefields, the receiver gathers in general look noisy. Nonetheless, several events can be seen on both the raw vertical component and one of the horizontal components of the data (Figures 3.5 and 3.6). The H2 horizontal component (Figure 3.7) appears to be mainly dominated by noise. The upgoing deconvolved P-wave and converted-wave reflections are shown in Figures 3.8 and 3.9 respectively. The reflection signals are strong on both the vertical and radial component receiver gathers. The results of processing the data are more evident on the radial component data. In Figures 3.6 and 3.7, the raw horizontal components lack regular moveout of events. On the contrary, the radial component in Figure 3.9 shows regular moveout of events. Also, events on the radial component data have larger moveout with offsets when compared to the vertical component data. These observations increase confidence about the processing results.

3.3.2 P-wave and converted-wave 3-D imaging

The deconvolved upgoing P-wave and converted-wave reflections were then used to generate 3-D volumes. Equation 2.13 and the velocity model in Figure 2.3 were first used to calculate the fold distribution for the P-wave at the target depth of 1500m for different bin configurations. A bin size of 110m by 20m was then decided upon as the smallest bin size that gave uniform fold distribution at the target depth (Figure 3.11). Due to the sparse data of about 2000 traces and reflection coverage of about a square km. at the target depth, the average fold per bin location was a small number. Moreover, although the bin size of 110m by 20m resulted in uniform fold distribution, the azimuth and offset coverage in each bin was somewhat variable. This was unavoidable due to the manner in which shots for the 3-D VSP survey were undertaken and also due to the recording taking place only in one well location.

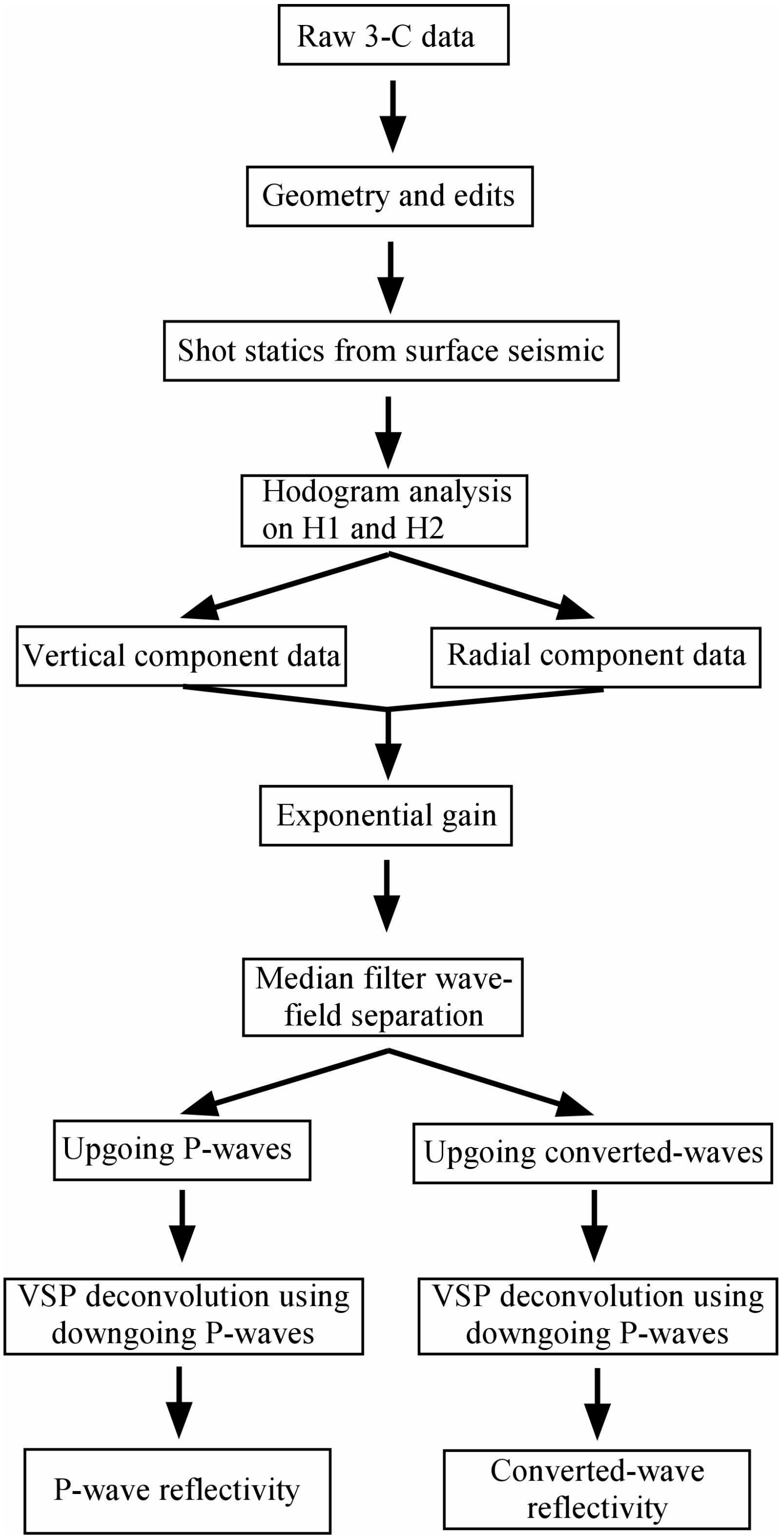

Fig.3.2. Processing flow to obtain deconvolved upgoing P-wave and converted-waves from the 3C-3D VSP data.

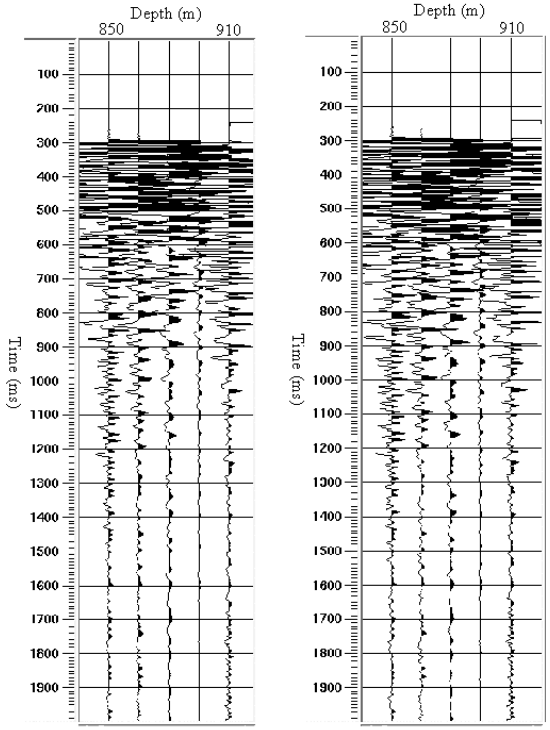

(a) Raw vertical component. (b) Raw H1 component.

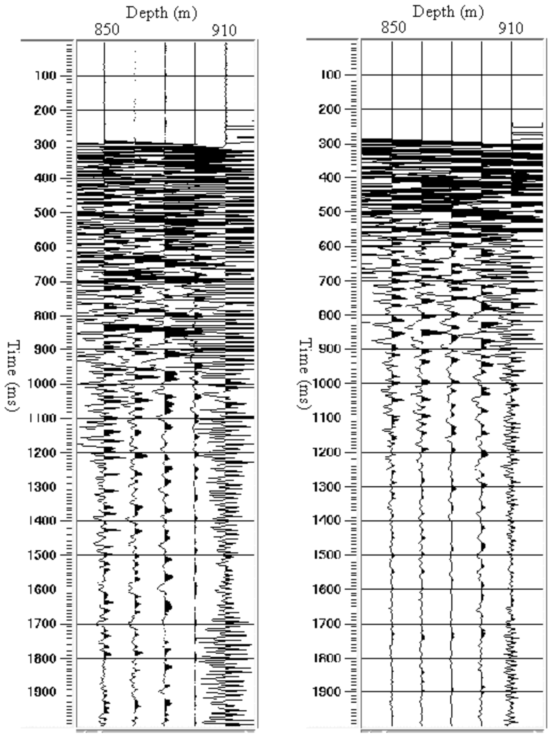

(c) Raw H2 component. (d) Radial component.

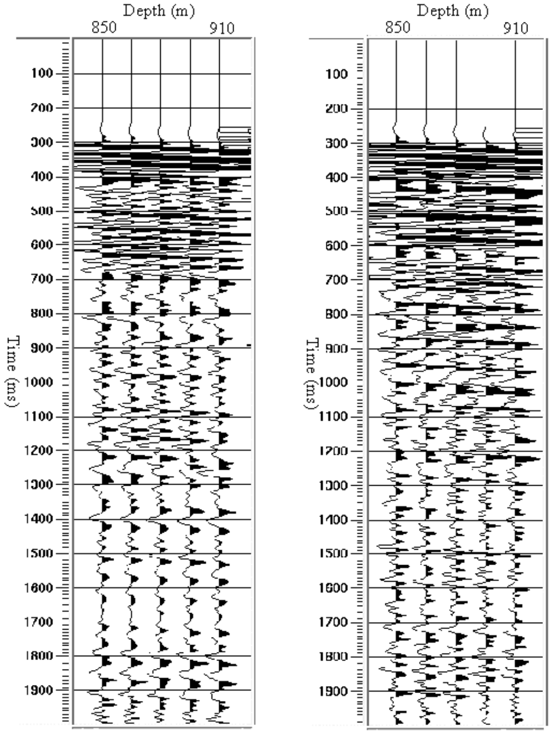

(e) Downgoing P-waves. (f) Downgoing converted-waves.

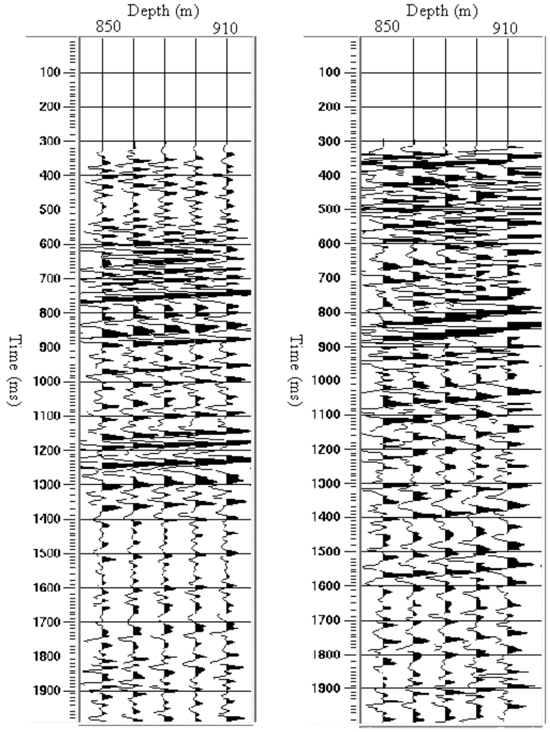

(f) Upgoing P-waves. (g) Upgoing converted-waves.

Fig.3.3. Shot gathers for shot at an offset of 372m from the well.

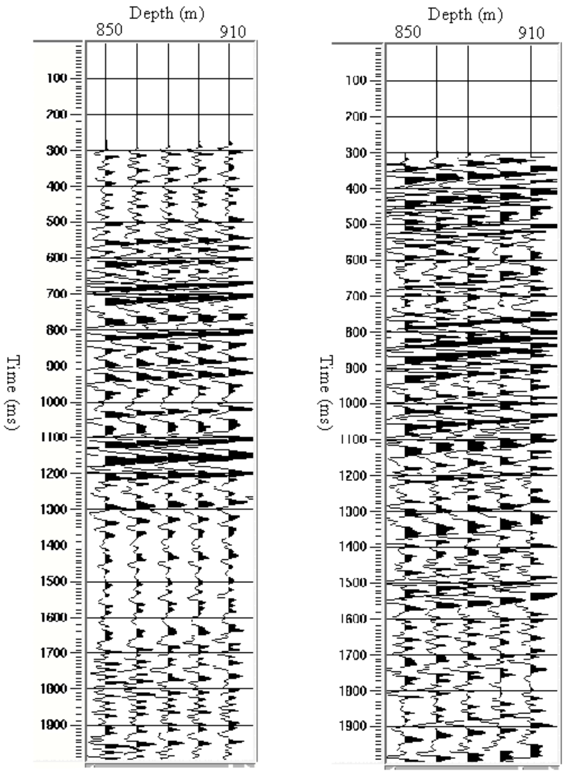

(a) Upgoing P-waves. (b) Upgoing converted-waves.

Fig.3.4. Deconvolved upgoing waves for the same shot gather as in Fig. 3.3.

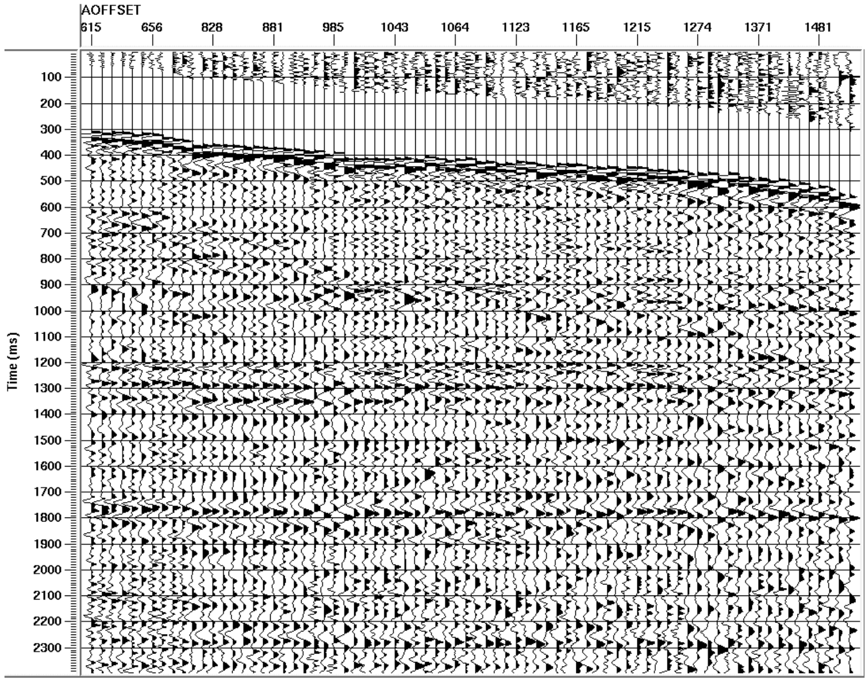

Fig.3.5. Raw vertical component receiver gather for receiver at depth 655m displayed with an AGC window of 500ms.

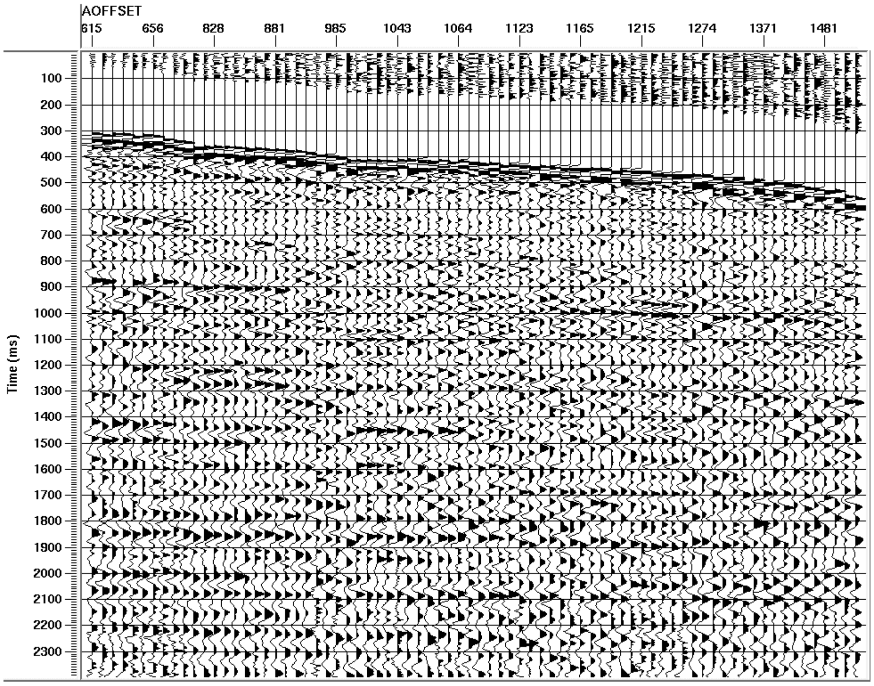

Fig.3.6. Raw H1 component receiver gather for receiver at depth 655m displayed with an AGC window of 500ms.

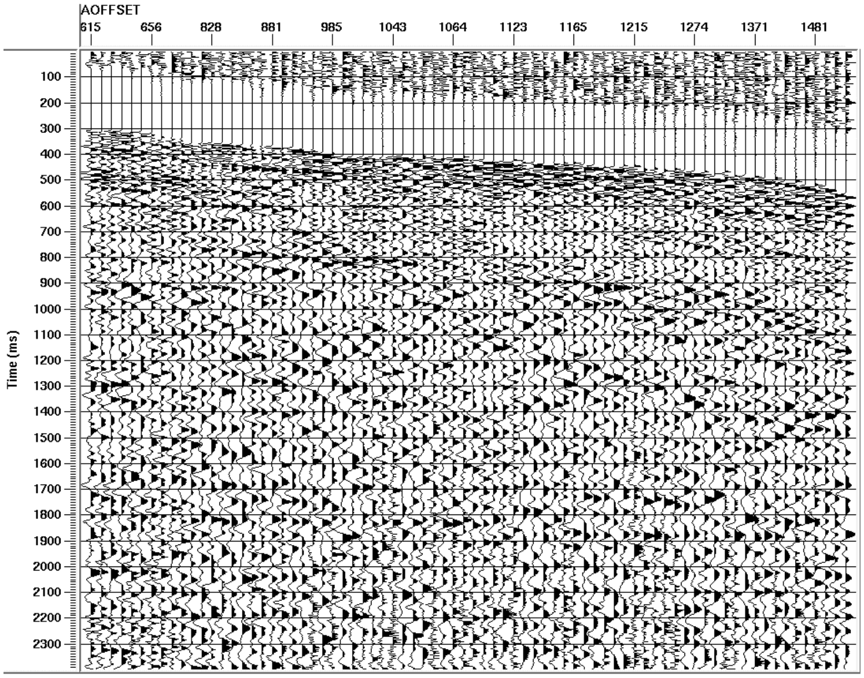

Fig.3.7. Raw H2 component receiver gather for receiver at depth 655m displayed with an AGC window of 500ms.

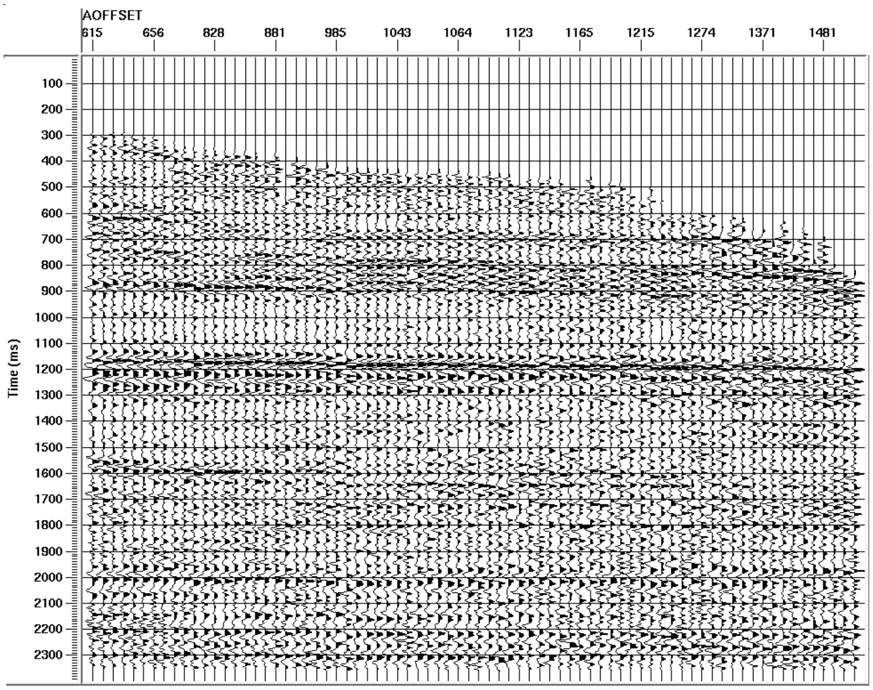

Fig.3.8. Deconvolved upgoing P-waves on vertical component receiver gather for receiver at depth 655m. Data is displayed with an AGC window of 500ms.

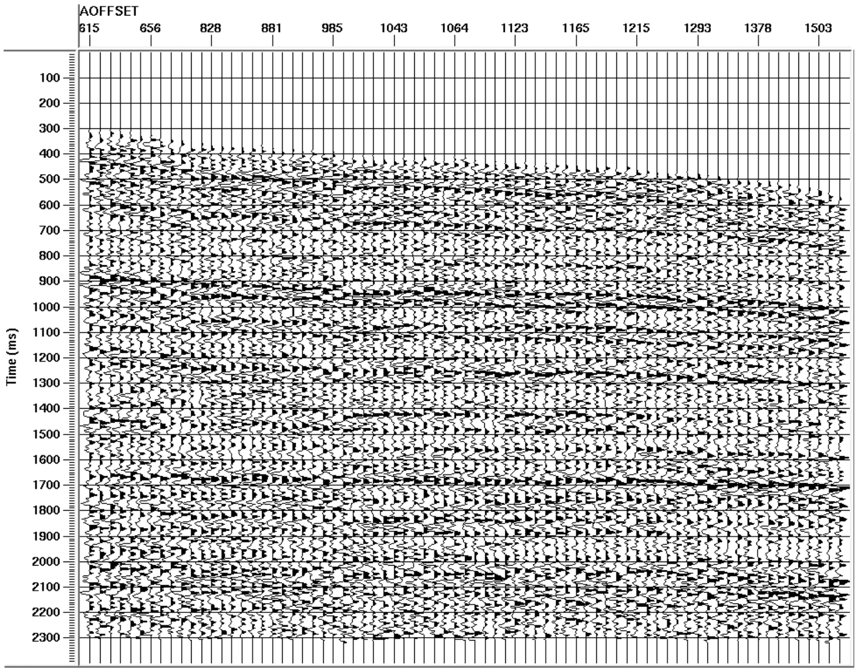

Fig.3.9. Deconvolved upgoing converted-waves on radial component receiver gather for receiver at depth 655m. Data is displayed with an AGC window of 500ms.

3.3.2.1 P-wave imaging

Two approaches were taken for the VSPCDP mapping of P-wave reflections (Figure 3.10). One approach was to use conventional raytracing and the other was to use amplitude semblance and Equation 2.3 mapping formula as discussed in Chapter 2. The elastic model used for the raytrace mappings is shown in Table 2.1.

The model was interactively built until traveltimes computed by raytracing through the model matched with the observed traveltimes (John Parkin, personal communication). Figures 3.12 and 3.13 show an inline from the VSPCDP stacks using the two mapping methods. The two are remarkably similar except at bin locations further from the well where the raytracing method yields more coherent reflections. This is more due to an incomplete implementation than due to the traveltime moveout approximation of the latter method. Figure 3.14 shows the correlation between the two results.

The stacked sections were then trace equalized followed by time-variant spectral whitening. To interpret the stacked volumes using standard interpretive techniques, we would require that every bin location be represented by a reflectivity value. As this was not possible with the 3-D VSP survey at hand, f-xy deconvolution was then used to fill in empty bin locations. F-xy deconvolution also serves to increase the coherency of reflection events (compare Figures 3.12 and 3.15).

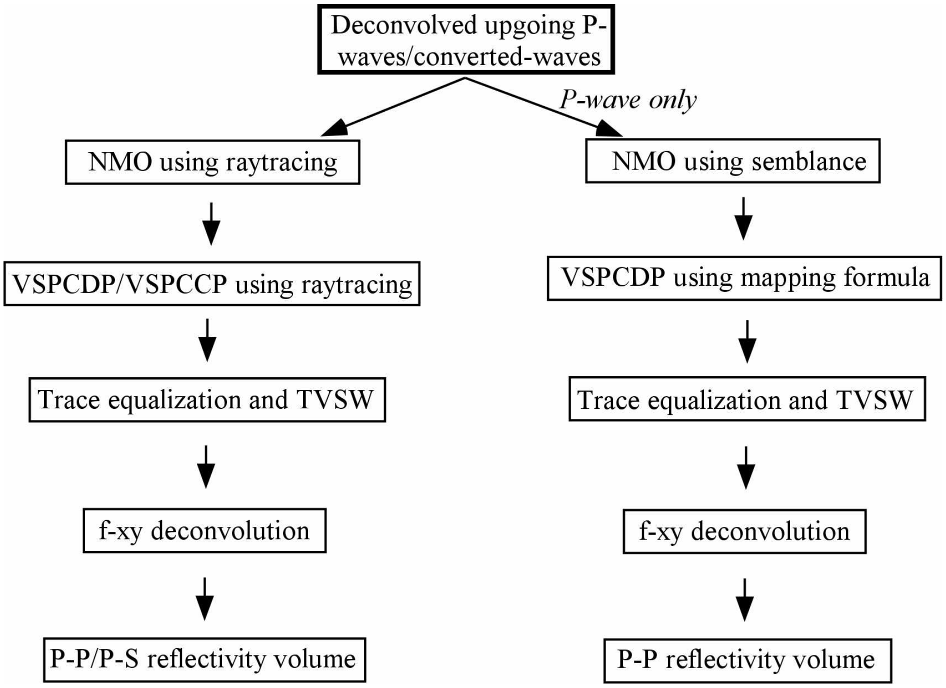

Fig.3.10. Flow for imaging the deconvolved upgoing P-wave and converted-wave reflections.

Table 2.1. Elastic model used for raytrace mapping. Datum depth = 1000m asl. (from John Parkin, pers. comm.)

Depth below datum (m)	P-wave velocity (m/s)	S-wave velocity (m/s)
224	3000	1500
600	3050	1605
963	3275	1725
1231	3512	1975
1486	3672	2062
1600	4179	2347
1733	4179	3125
2000	5500	3425
2500	6000	3690
3000	5900	3650
3500	5850	3625
6500	5850	3650

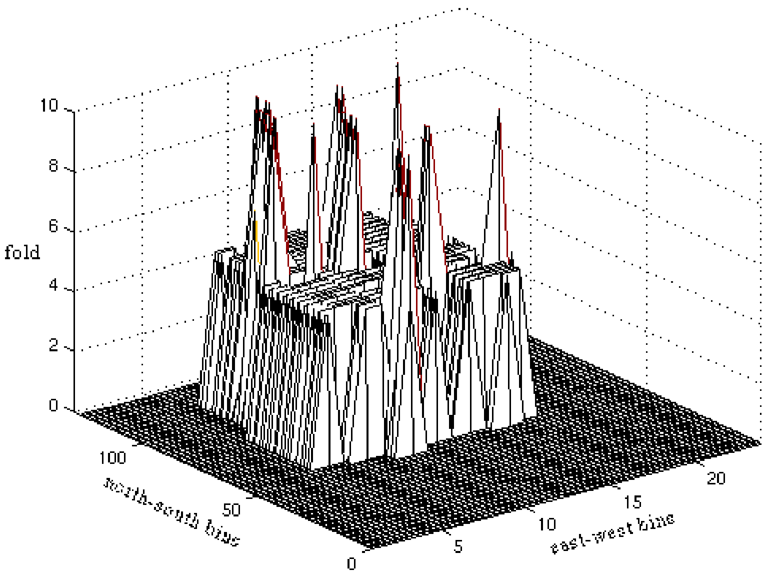

Fig.3.11. Fold distribution for P-P data at the target depth of 1500m when using a bin size of 110m by 20m.

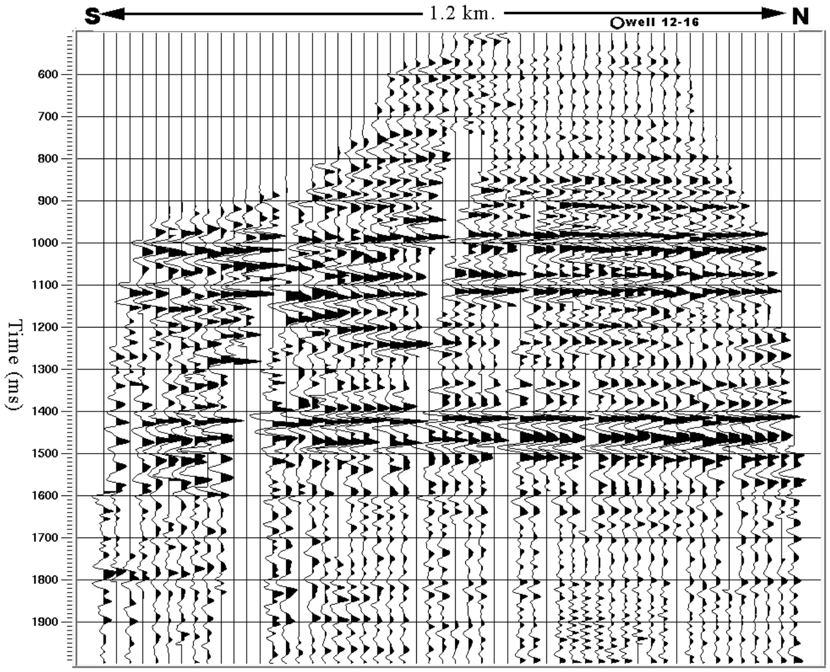

Fig.3.12. An inline section from the P-wave 3-D volume obtained from raytracing. Shown also is the crossline surface location of well 12-16.

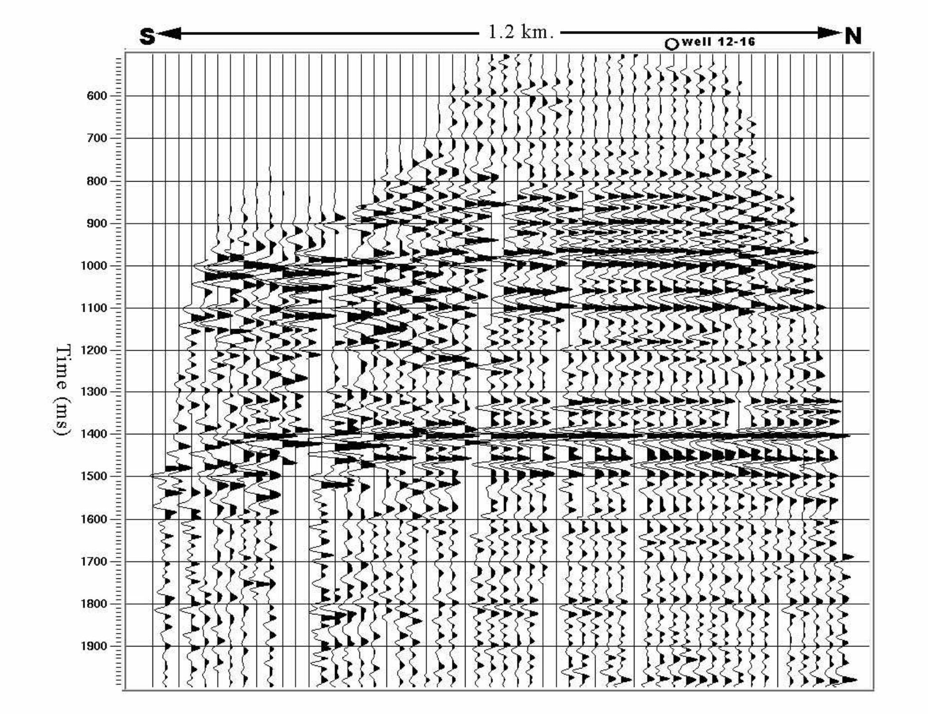

Fig.3.13. An inline section from the P-wave 3-D volume obtained from semblance and mapping formula. Shown also is the crossline surface location of well 12-16.

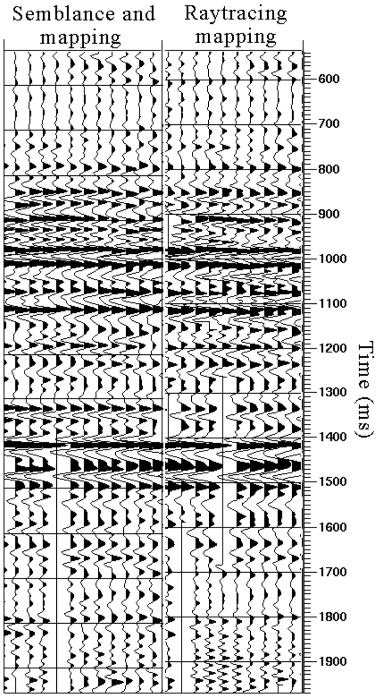

Fig.3.14. Correlation of the 3-D VSPCDP stacking of P-wave reflections using two different mapping methods.

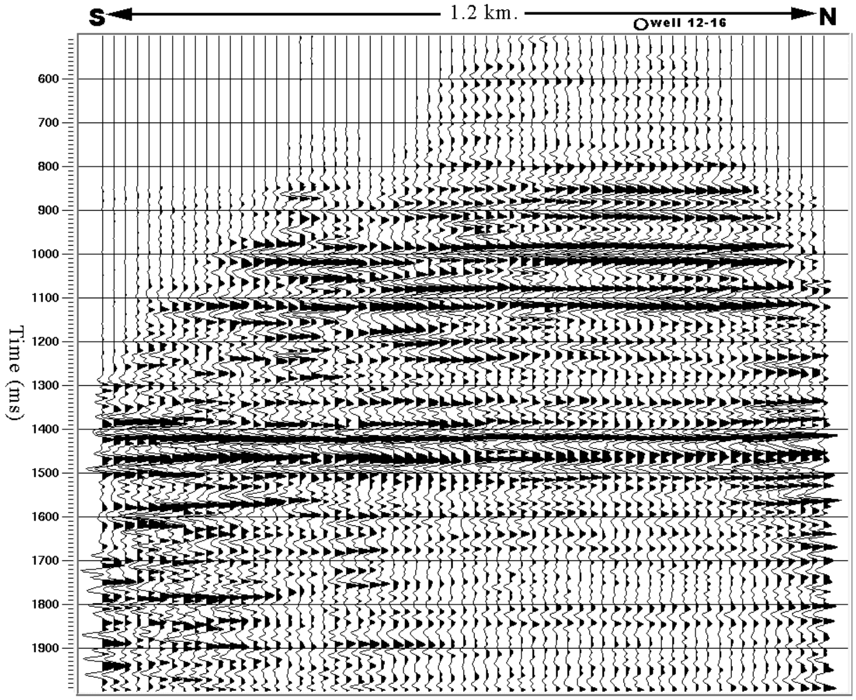

Fig.3.15. Same inline section as in Figure 3.12 but after trace equalization, time-variant spectral whitening and f-xy deconvolution.

3.3.2.2 Converted-wave imaging

The converted-wave reflection mapping was done using the conventional raytracing approach only. Apart from raytracing being the preferred option for converted-wave mapping, the approximate converted-wave mapping could not be implemented due to technical reasons.

The radial component data was VSPCCP stacked using the same bin size of 110m by 20m as in the case of P-wave data (Figure 3.16). The stacked data was then passed through the same processes as in the case of P-wave data to give the final interpretable volume (Figure 3.17). Unlike P-wave data, all mode-converted events experience strong amplitude variation with offset and which is known to be a quasi-sinusoidal function of the P-wave incident angle (Gulati and Stewart, 1997). Likewise for the present survey, strong converted-waves are observed for shallow reflectors (Figures 3.16 and 3.17) as the P-wave incident angle for these appear to fall in the zone where mode-conversion is maximum. On the other hand, in the case of deeper converted-wave events such as the one at around 2100ms, the expected sinusoidal-like amplitude behaviour is visually evident. Thus, when designing a 3C-3D VSP survey for converted-wave interpretation, care should be taken to place the receivers at depths such that P-wave incident angles at the target depth fall in the range of maximum mode conversion. Fortunately, the present survey appears to satisfy this criterion for the target reflection time around 1550ms.

3.4 P-wave and converted-wave correlation and interpretation

3.4.1 P-wave interpretation

Formation tops were identified on the 3-D VSP P-wave image by correlating it with a image from a previously interpreted surface 3C-3D survey in the area (Figure 3.18). There exists good correlation between the two although the VSP is lower frequency. Following this correlation, a time slice at the channel level was obtained from the VSP. Figures 3.19 and 3.20 show the time slices for the VSP from the two mapping methods and Figure 3.21 shows the corresponding time slice from the surface 3-D survey. Both the time slices from the 3-D VSP show a similar northeast-southwest trend which is evident on the surface data time slice as well.

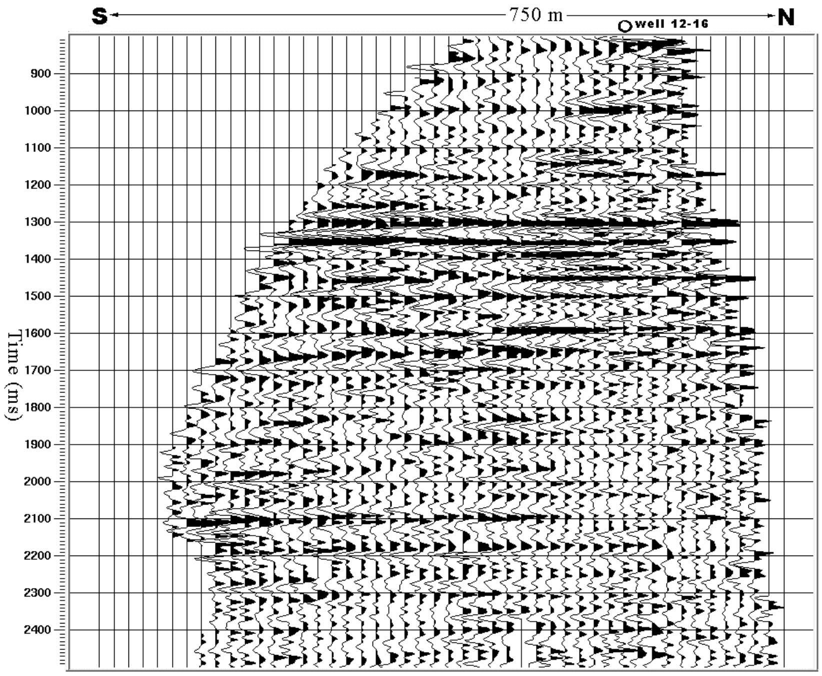

Fig.3.16. An inline section from the converted-wave 3-D volume obtained from raytracing. Shown also is the crossline surface location of well 12-16.

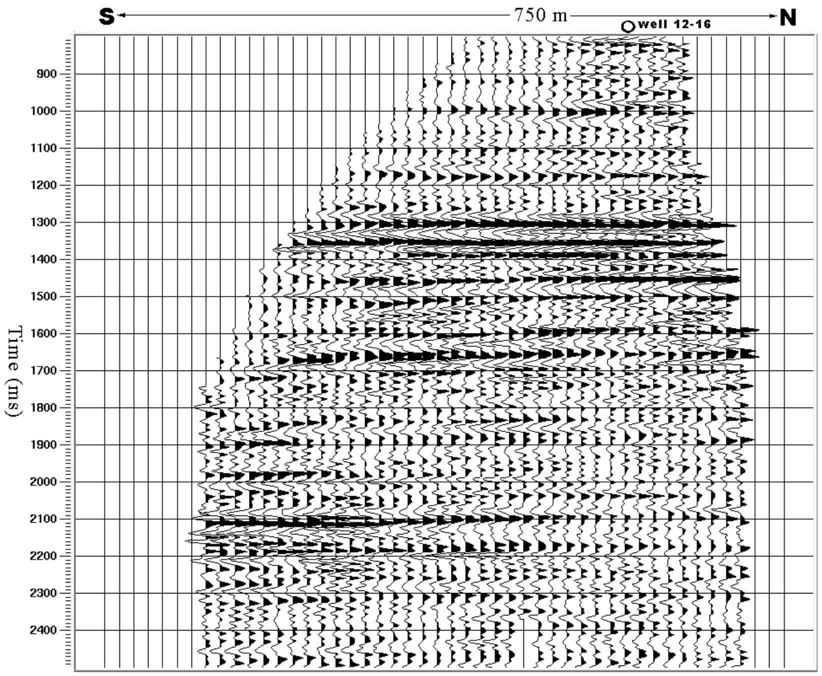

Fig.3.17. Same inline section as in Figure 3.16 but after trace equalization, time-variant spectral whitening and f-xy deconvolution.

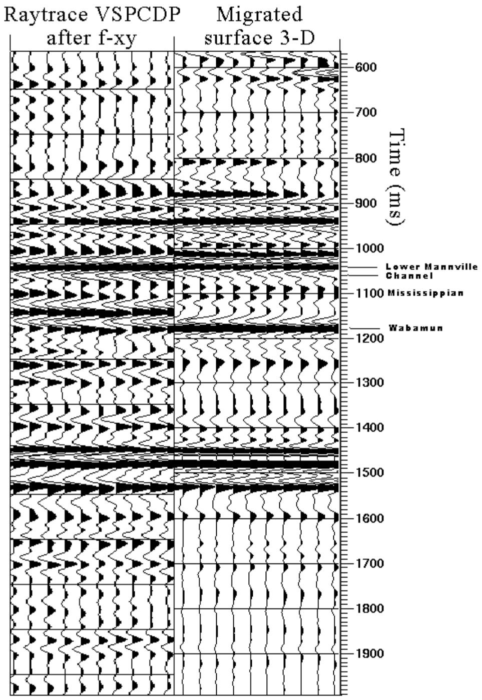

Fig.3.18. 3-D VSP P-wave correlation with migrated surface 3-D P-wave data. The VSP is displayed with reversed polarity.

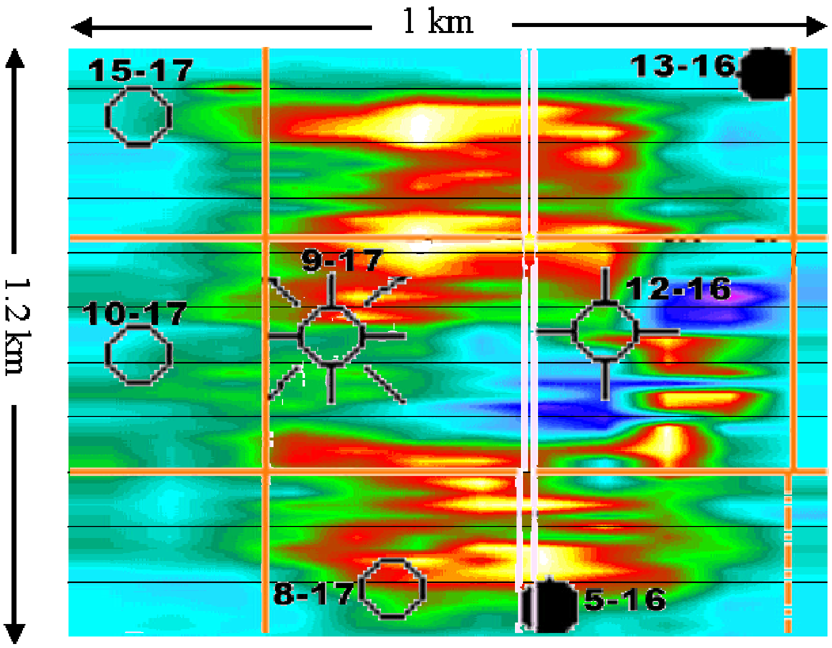

Fig.3.19. P-wave time slice at the channel level from the raytraced VSPCDP volume with flattening at the Mannville.

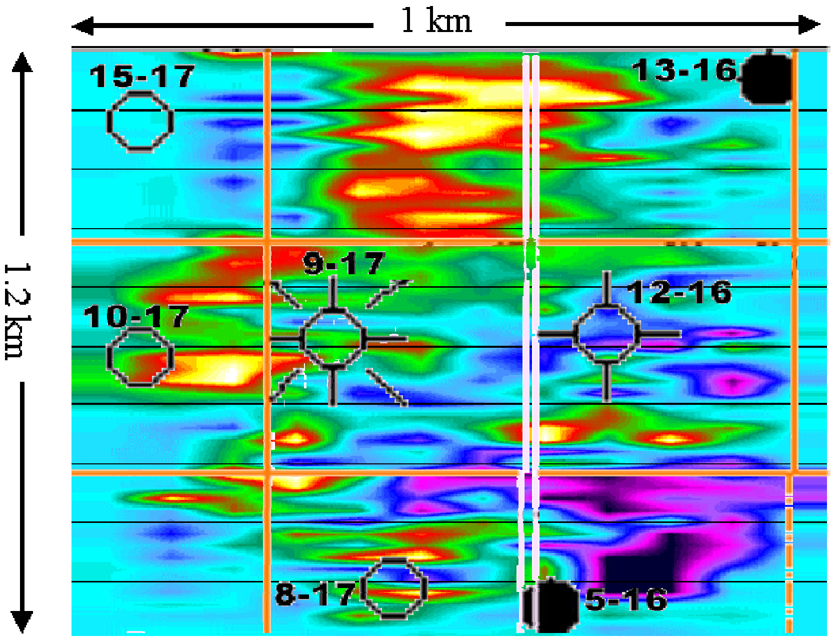

Fig.3.20. P-wave time slice at the channel level from the semblance and mapping formula VSPCDP volume with flattening at the Mannville.

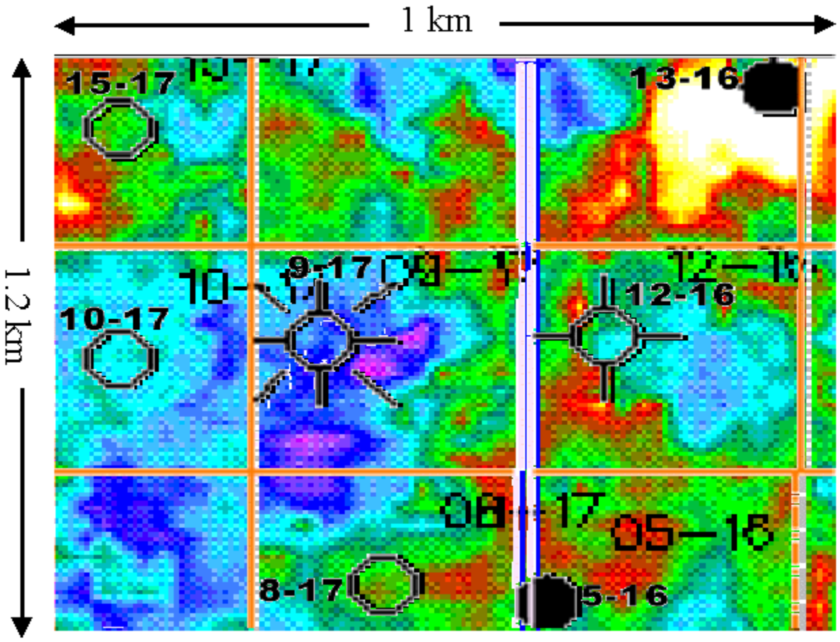

Fig.3.21. P-wave time slice at the channel level from the migrated surface 3-D volume with flattening at the Mannville (modified from Yang et al., 1996).

Figure 3.22 shows the entire time slice from the surface 3-D survey. It shows a north-south channel trend joined by another channel body from the west in the north-side of the map. Figure 3.23 shows the same time slice but with the time slice from the raytraced 3-D VSP inset into it. Comparing Figures 3.22 amd 3.23, one can observe that the channel trend is similar in both the time slices. However, the channel in the northern part of the map appears to have a more easterly trend in the original time slice of Figure 3.22.

3.4.2 Converted-wave interpretation

The converted-wave image from the VSP was also correlated and interpreted in a similar manner. Formation tops were identified on the converted-wave data from the VSP by correlating it with a previously interpreted surface 3C-3D survey in the area (Figure 3.24). In the zone of interest, the converted-wave from the VSP appears to show somewhat better resolution than the converted-wave image from the surface seismic data. However, at later times, the surface seismic image is higher frequency compared to the VSP image.

In addition, the above converted-wave images were also correlated with P-wave images from the 3-D VSP and the surface 3-D, with images from an offset 3-C VSP and with synthetics derived from well-logs (Figure 3.25). From these correlations, the channel anomaly on the converted-wave 3-D VSP image is seen to be a trough. Following this, a time slice at the channel level was obtained for the converted-wave image from the 3-D VSP (Figure 3.26). The corresponding time slice from the surface 3C-3D survey is shown in Figure 3.27. Due to their small size, it is difficult to interpret these time slices. Figure

3.28 shows the converted-wave time slice from the entire 3C-3D survey and Figure 3.29 is the same time slice but with the converted-wave time slice from the 3-D VSP inset into it. The north-south trending channel has a easterly drift in the north part of the map in Figure 3.28. The same trend is seen in Figure 3.29 as well but the drift to the east starts more to the south in Figure 3.29 than in Figure 3.28.

3.5 Conclusions

The Blackfoot 3-D VSP experiment has shown that acquisition of simultaneous 3-D VSP and surface seismic surveys is possible and is cost-effective. Basic processing of the 3-D VSP data has shown the robustness of such simultaneous acquisitions. There is also a need for improvement in the wavefield separation and deconvolution processes and new techniques need to be developed.

VSPCDP stacking of the 3-D VSP data using amplitude semblance analysis was observed to yield meaningful results. While the recording geometry for the 3-D VSP was not ideal, both P-wave and converted-wave VSP images were observed to correlate well with images from the surface 3C-3D in the same area. Time slices from the 3-D VSP also indicated the channel trend evident on the surface data. Results from this preliminary survey show the promise of the 3-D VSP. The 3-D VSP could be a significant tool to obtain high-resolution 3-D images near the borehole.

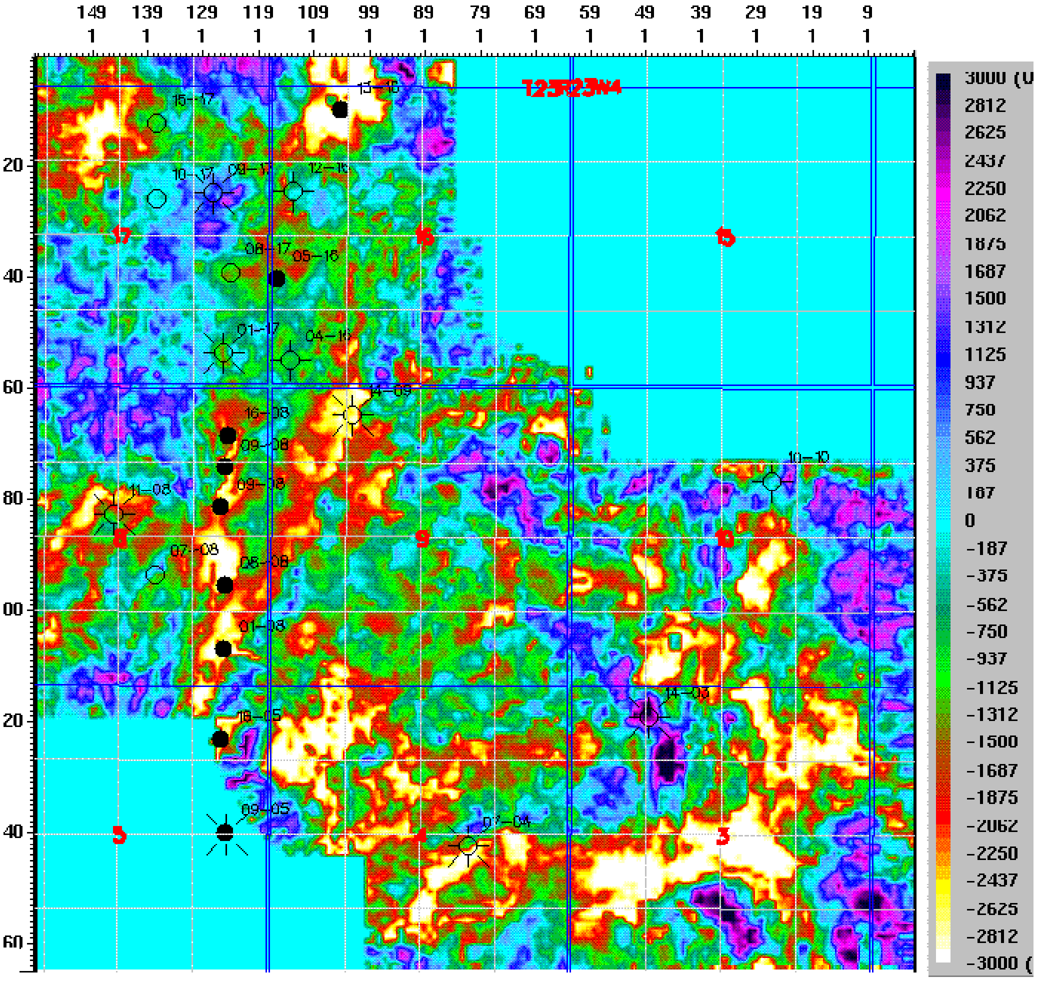

Fig.3.22. P-wave time slice at the channel level for the entire surface 3-D survey (from Yang et al., 1996).

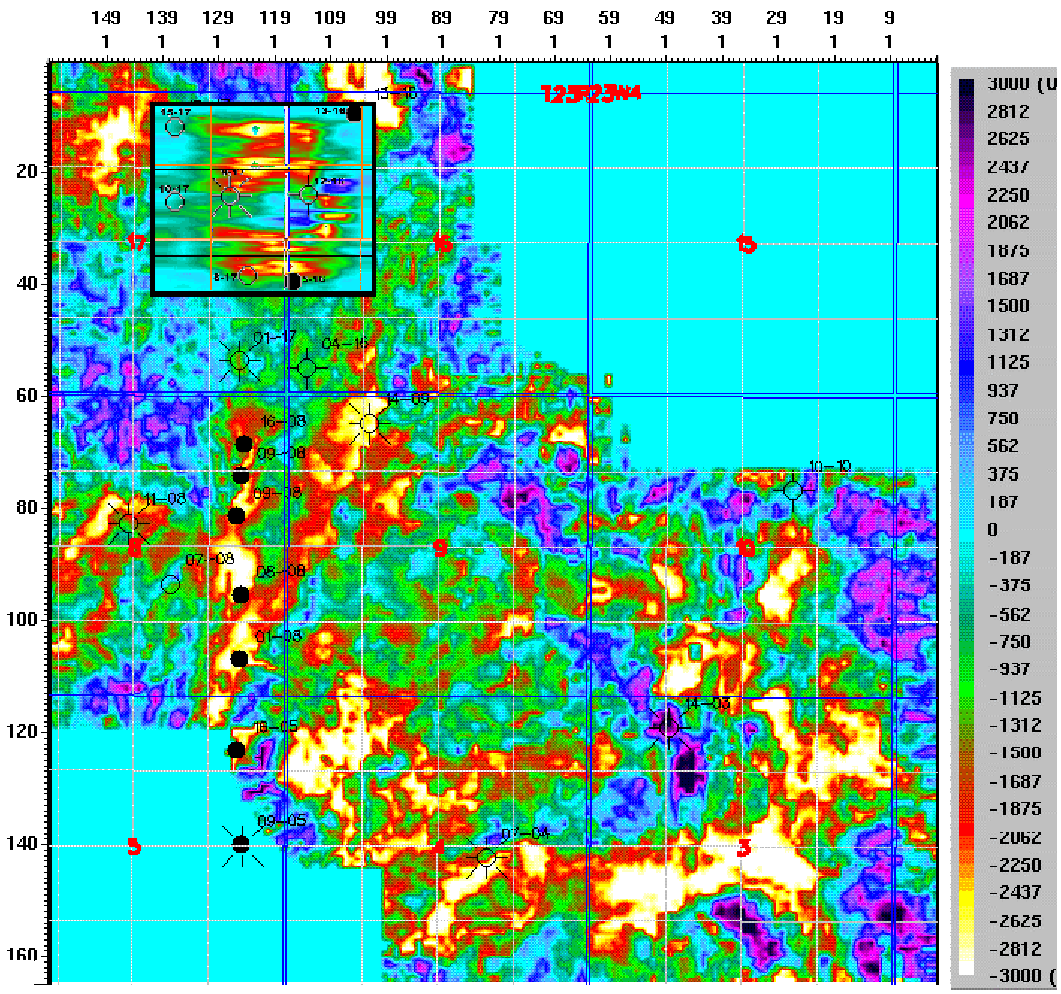

Fig.3.23. P-wave time slice at the channel level from Figure 3.17 inset into the corresponding time slice for the entire 3-D survey.

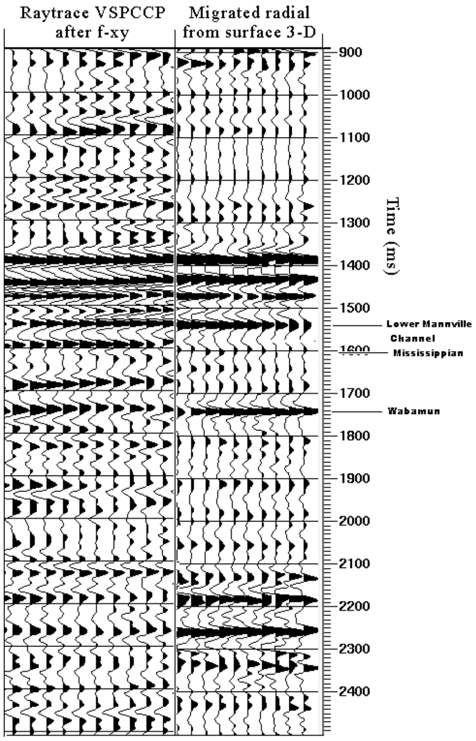

Fig.3.24. 3-D VSP converted-wave correlation with migrated 3-D converted-wave data from surface seismic.

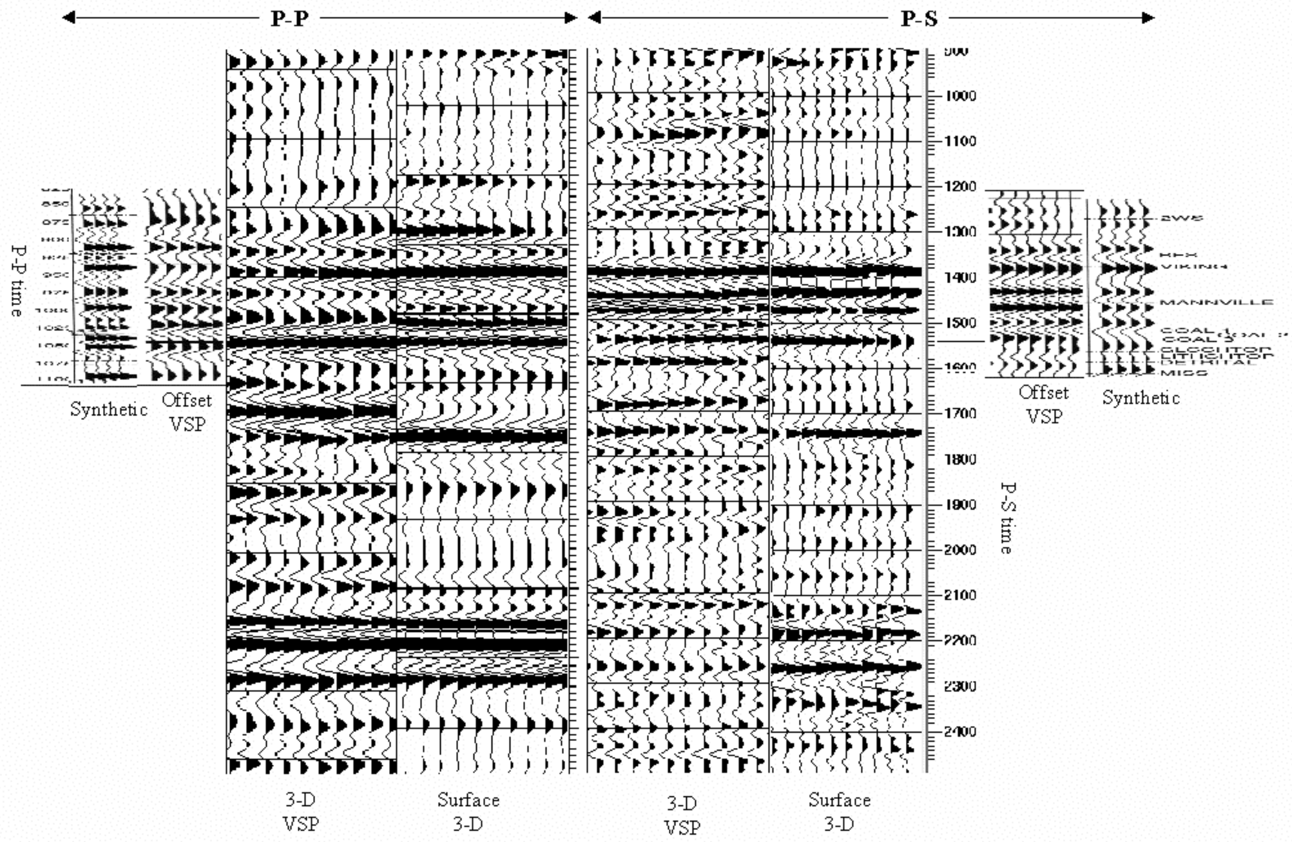

Fig. 3.25. Correlation between synthetics and different data

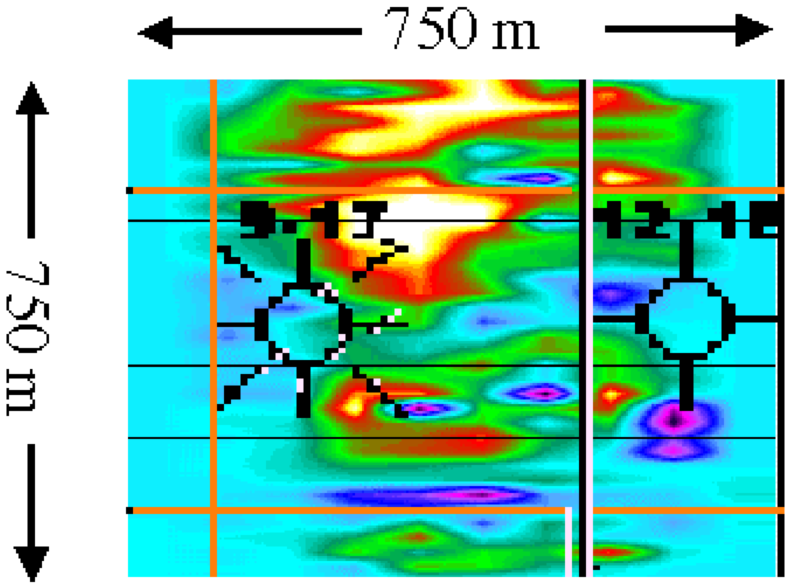

Fig.3.26. Converted-wave time slice at the channel level, flattened at the Mannville, from the 3-D VSP.

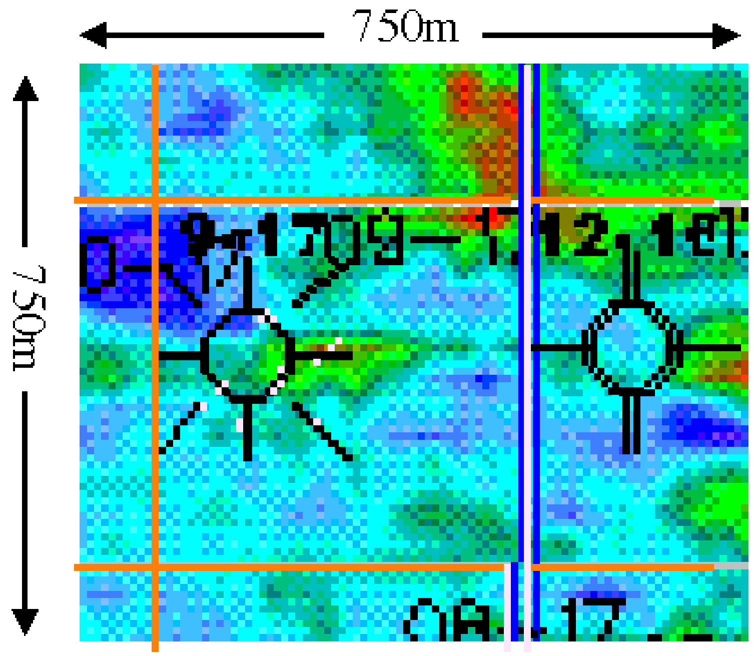

Fig.3.27. Converted-wave time slice at the channel level, flattened at the Mannville, for the area in Figure 3.22 from the migrated surface 3-D radial data (modified from Yang et al., 1996).

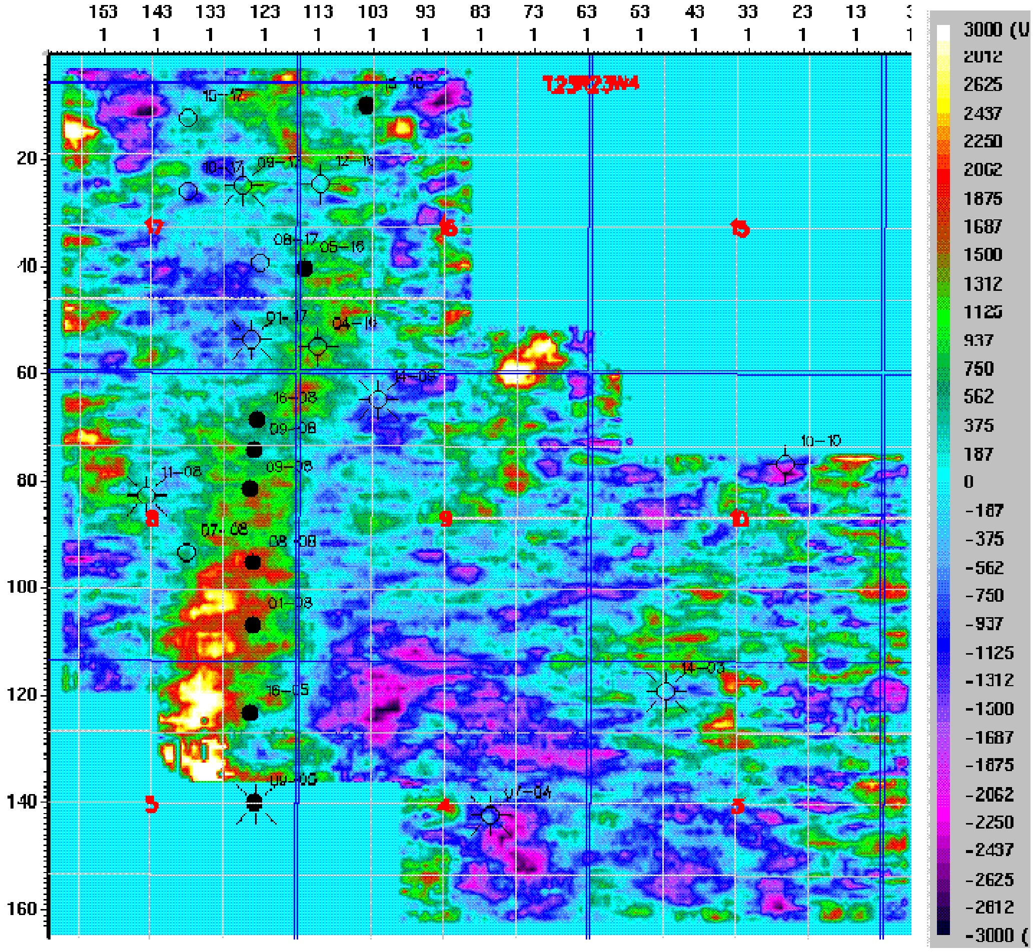

Fig.3.28. Converted-wave time slice at the channel level from the migrated surface 3-D radial data (from Yang et al., 1996).

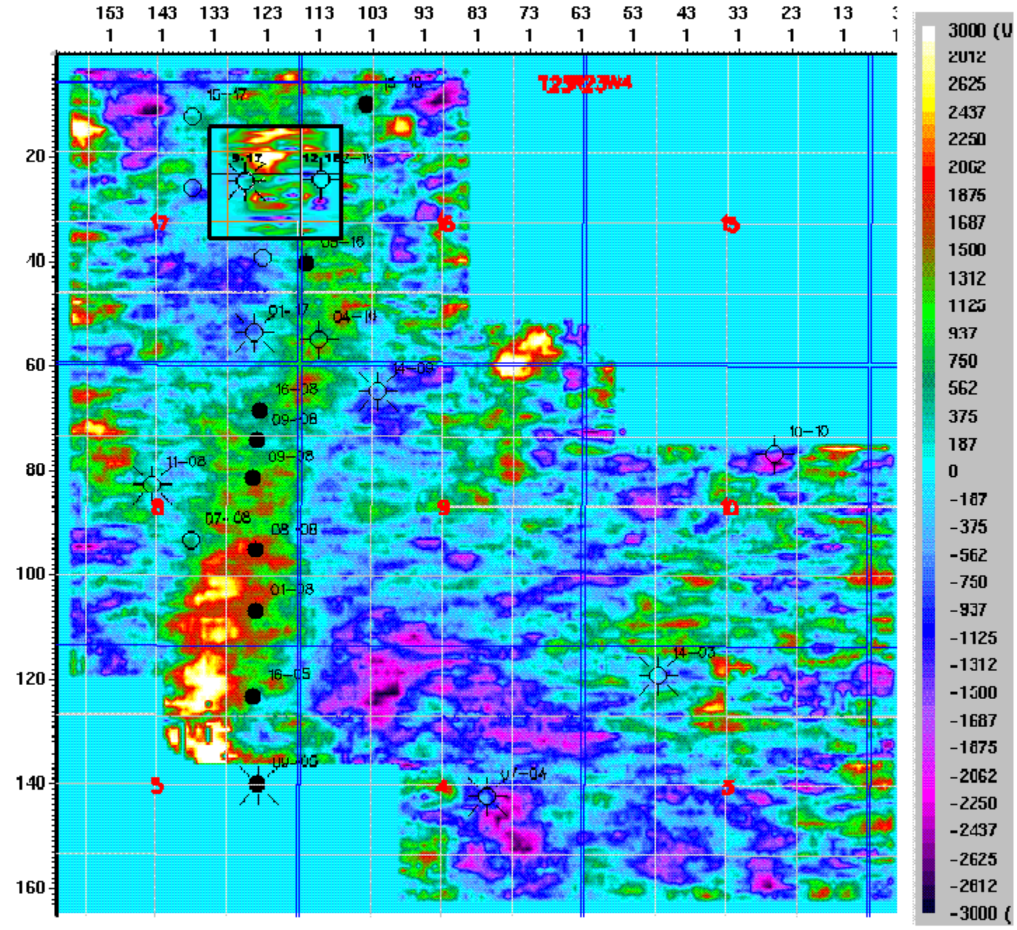

Fig.3.29. Converted-wave time slice at the channel level from Figure 3.22 inset into the corresponding time slice for the entire 3-D survey.

CHAPTER 4: LAND VERTICAL CABLE ACQUISITION AND IMAGING

4.1 Introduction

The widespread use of vertical seismic profile (VSP) data in imaging the earth is partially hindered by its cost. Apart from a well being required, the VSP is expensive in its present form also due to the speed at which the data are acquired. VSP data are conventionally acquired using downhole seismic tools containing three-component geophones clamped to the borehole wall. Coupling the geophone to the borehole wall is critical to recording true earth motion (Van Sandt and Levin, 1963; Wuenschel, 1976; Gaiser et. al., 1988; Wuenschel, 1988) and is a complicated and time-consuming process in the borehole. Another factor adding to the acquisition time is that most tools have a maximum of five geophone levels, so the tool is usually moved over the borehole length and shot points repeated to obtain adequate fold and offset coverage per bin location. Recently, Omnes and Clough (1998) demonstrate the implementation of a twelve-level tool which significantly reduced the acquisition time of the VSP surveys they conducted. This is a welcome advance. Paulsson (1998) shows data from a 40-level receiver tool.

A less expensive alternative for the rapid and efficient acquisition of VSP data is the use of multi-level vertical hydrophone array. Hydrophones are pressure sensitive receivers and not required to be clamped to the borehole wall. They are, therefore, easy to deploy in a borehole and a large number of them can be simultaneously used in the borehole. Early experiments using hydrophone detectors in borehole were those conducted by White and Sengbush (1953) and Riggs (1955). Recent experiments to evaluate the capabilities of using a vertical array of hydrophones for VSP on land were carried out by

Marzetta et. al. (1988) and Krohn and Chen (1992). Findlay et al. (1991) and Sheline (1998) showed the successful implementation of an offshore crosswell reflection imaging program that used an array of hydrophone receivers. Milligan et. al. (1997) demonstrated the viability of using a vertical hydrophone array in a walkaway VSP to image shallow structures on land. Most authors note that a major impediment to the use of vertical hydrophone array in a borehole has been the presence of strong coherent noise on the VSP data in the form of tube waves. Tube waves are guided waves confined to the borehole fluid and hydrophones are more sensitive to the tube waves compared to properly clamped geophones (Wuenschel, 1988; Krohn and Chen, 1992).

Both field and processing methods to attenuate tube wave noise on VSP data have been investigated by several authors. Riggs (1955) and Gal'perin (1974) observed that moving the surface source away from the borehole significantly reduced the intensity of tube waves. Hardage (1981) made similar observations and also found surface ground roll sweeping across the well head to be the principal source of tube waves. Krohn and Chen (1992) used dipole hydrophones to attenuate tube waves in field. Pham et al. (1993) and Milligan et al. (1997) used closed-cell-foam baffles between hydrophone elements to suppress tube waves in borehole surveys. Velocity filtering has been very effective in isolating tube waves in the processing centre (Hardage, 1981; DiSiena et al., 1984; Marzetta et al., 1988; Milligan et al., 1997). Median and wavelet filtering can also be used to remove tube waves from VSP data (Schuster and Sun, 1993). Marzetta (1992) developed an inverse borehole coupling theory to derive a tube-wave free quantity which he called as “squeeze strain” from data recorded using hydrophones in a borehole.

While these field experiments are very important to the study of vertical hydrophone cable on land, the source-offset and the depth range in these surveys was severely limited. The use of hydrophones in VSP surveys depends on the ability to obtain reliable offset sections or seismic volumes of size of current VSP surveys. It was to fill in some of these gaps that the CREWES Project at the University of Calgary acquired a shallow vertical hydrophone cable data on land in November 1997 at the Blackfoot oil field located in Alberta, Canada. The objectives of the hydrophone VSP survey were 1) to compare hydrophone data with nearby three-component geophone records and determine the validity of the raw hydrophone records and 2) to see if the hydrophone cable can be used to obtain reliable stand-alone images. The following sections give details of the Blackfoot land vertical cable survey from the acquisition to the data analysis and interpretation stage.

4.2 Field description and data acquisition

On November 1-2, 1997 the CREWES Project at the University of Calgary with assistance from Boyd PetroSearch Consultants Ltd. and PanCanadian Petroleum Ltd. recorded a high-resolution 3C-2D seismic survey at the PanCanadian-owned Blackfoot field. The Blackfoot field is located some 50-55km east of Calgary in Alberta, Canada (Figure 4.1). As described before, the producing formation within the Blackfoot area is a Lower Cretaceous, cemented glauconitic sand.

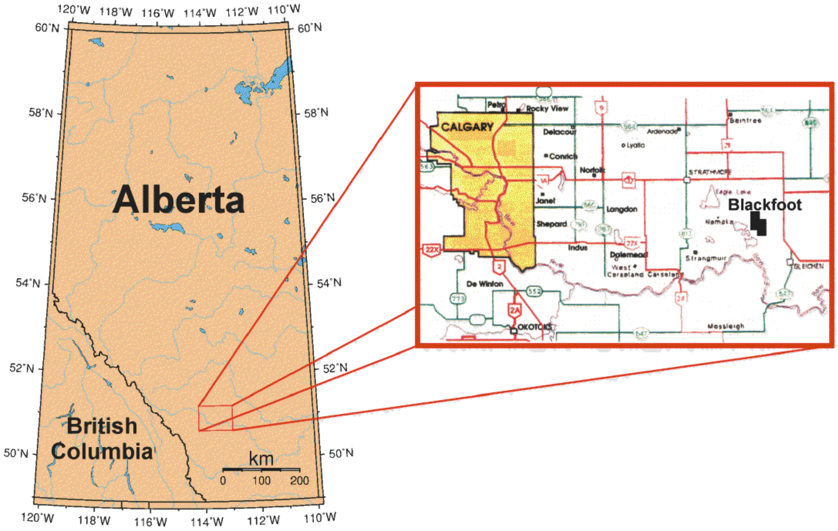

Fig.4.1. Map showing the location of the PanCanadian Blackfoot field.

The 3C-2D survey involved the acquisition of a 3km reflection profile which consisted of a combination of “normal-resolution” 20m and “high-resolution” 2m receiver intervals. The shot interval employed for the entire 2D profile was 20m and shot on the half-station. The survey also involved the simultaneous recording into 21×3 buried 3-C geophones situated in 6, 12 and 18m holes drilled every 50m along the central km of the profile. In addition to these buried geophones, a 48-channel vertical hydrophone cable with a 2 m receiver interval was deployed in a 100m cased hole located in the centre of the profile (Figure 4.2). A walk-away AVO VSP was also recorded in a well located near the centre of the spread at the same time the surface shots were being taken.

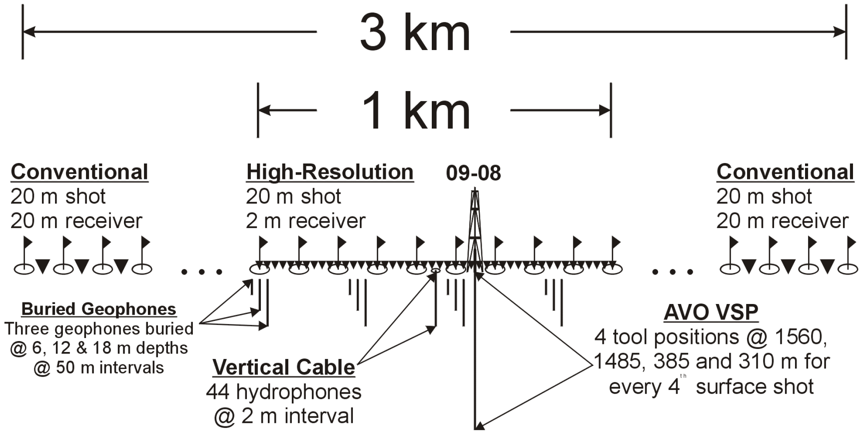

Fig.4.2. A schematic diagram of the Blackfoot 3C-2D survey (not to scale).

The 48-channel hydrophone cable consisted of Benthos AQ-4 hydrophones at 2m separation with AQ-302 preamps molded into the cable which is terminated by an Amphib-122 connector. Adapter plugs were constructed to tie these channels into the surface recording spread and the preamps were powered via a 12V battery during recording. Acquisition parameters for the hydrophone data were the same as that for the entire survey. Data were recorded with a 6s record length at a sampling rate of 1ms. The preamp gain used for recording was 24dB with low and high cut filters set at 3Hz (12dB slope) and 413Hz (293dB slope) respectively. A total of 151 shot points with each consisting of a 4kg charge size loaded in a single hole at 18m depth were used for the survey.

The objectives and results of the entire survey are discussed in Hoffe et al. (1998). In this chapter, results from the hydrophone data are presented.

4.3 Vertical hydrophone cable data versus geophone data

Hydrophones and geophones not only measure different physical quantities but also record data in different physical environments. One is suspended in a fluid medium in a borehole or in a marine environment whereas the other is clamped to a borehole-solid interface or an air-ground interface. Properly clamped geophones are believed to portray the true earth motion. Therefore the use of hydrophones in borehole surveys is justified if it is known that the pressure waveform in the borehole fluid is directly related to the stress waveform in the solid when an elastic wave passes the borehole. White (1953) developed a “borehole coupling” theory which quantified borehole fluid pressure and motion due to the passage of low frequency elastic waves past the hole. He observed that the “formation break” [*White (1953) defines “formation break” as the pressure signal that has the same phase velocity as of that of the wave cutting the borehole, and which was also called as “squeeze strain” by Marzetta (1992)*] due to a compressional wave was in phase with the disturbance in the surrounding solid. This is true when the velocity of the wave in the solid is larger than that in the borehole fluid. Blair (1984) and Schoenberg (1986) also made similar observations for low frequency or which is the same as long wavelength seismic waves.

The borehole radius in which the vertical hydrophone cable was deployed was around 14cm. Using frequency filter panels, the smallest possible wavelength of the seismic data was calculated to be 20m. The borehole geometry, therefore, satisfied the long wavelength criterion given by Blair (1984) and the hydrophones should represent the earth motion similar to a geophone in the surrounding solid. Thus, in theory, we expect the P-wave signal on the pressure and velocity phones to be in phase assuming similar detector transduction for both phones.

To test the validity of this hypothesis, a hydrophone receiver gather at 18m depth is compared with a three-component geophone gather at the same depth located about 8m away from the hydrophone. Field tap tests showed that an upcoming compressive stress would record as a negative pulse on the geophone and a pressure increase would record as a positive pulse on the hydrophone. We analyzed the field data considering the above report. The first break refraction arrivals on the geophone and the hydrophone appeared opposite polarity. On reversing the polarity of the hydrophone data, the first break arrivals on the two phones appeared to be in phase with each other. This is in direct agreement with White's borehole coupling theory and increased our confidence about the hydrophone data.

Figures 4.3-4.5 show the hydrophone data at 18m depth, the vertical and the inline horizontal component of the geophone at the same depth respectively. One can observe that although the hydrophone is noisy compared to the geophone gather it mimics the refraction and reflection arrivals of the geophone data. The hydrophone data has the character of both the vertical and inline horizontal components of the geophone. This is because the hydrophone is sensitive to pressure generated by both the compressional and shear wavefields. Notice also that reflections on the hydrophone data are more prominent for shots at intermediate-to-far offsets as the ground roll arrives later in time. This conforms well with Hardage's (1981) observation that ground roll is the major source of tube waves.

Figure 4.6 is a comparison of the amplitude spectrum of the stack of the hydrophone and vertical component geophone gather at 18m depth. The hydrophone is seen to be lower frequency compared to the geophone stack. Also, severe notches on the spectrum of the hydrophone stack are representative of the tube wave interference with body wave reflections on the hydrophone gather.

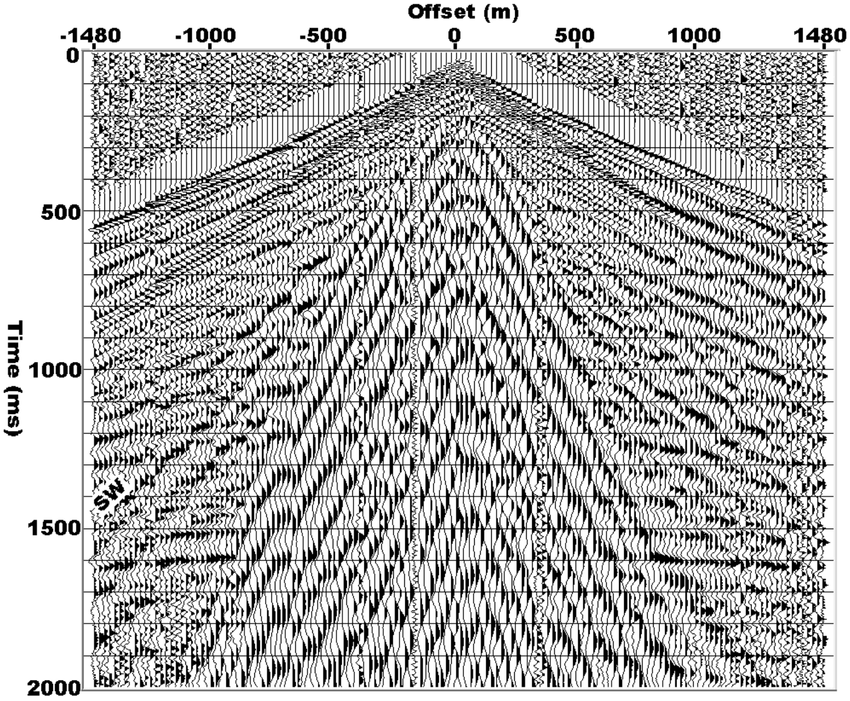

Fig.4.3. Receiver gather for hydrophone at 18m depth displayed with reversed polarity and 250ms AGC window. SW is the zone of shear-wave refraction arrivals.

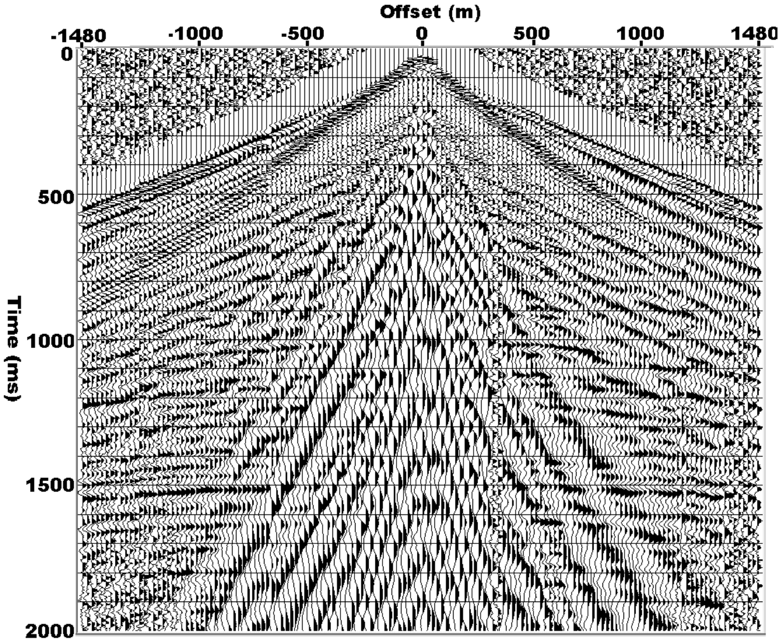

Fig.4.4. Receiver gather for vertical component geophone at 18m depth displayed with normal polarity and 250ms AGC window.

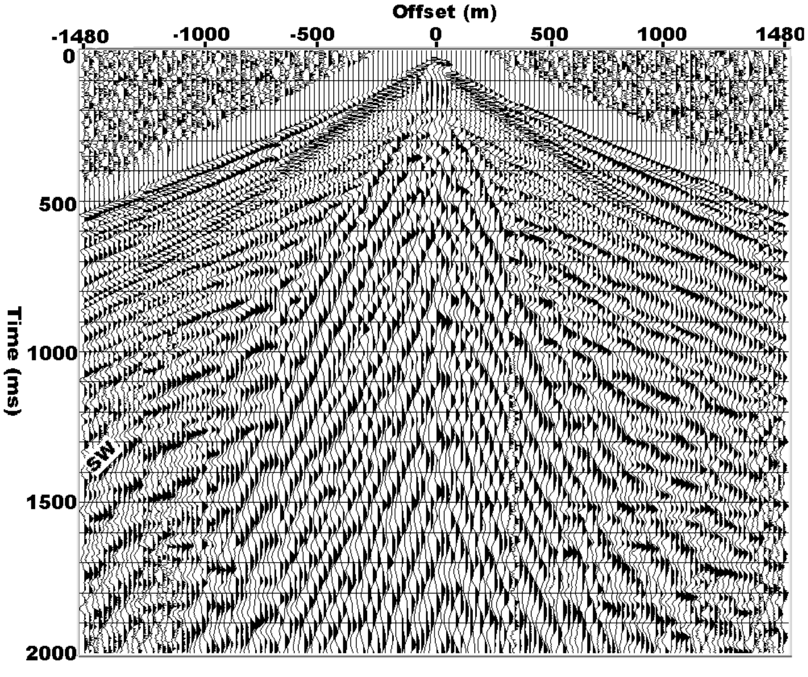

Fig.4.5. Receiver gather for inline horizontal component geophone at 18m depth displayed with normal polarity and 250ms AGC window. SW is the zone of shear-wave refraction arrivals.

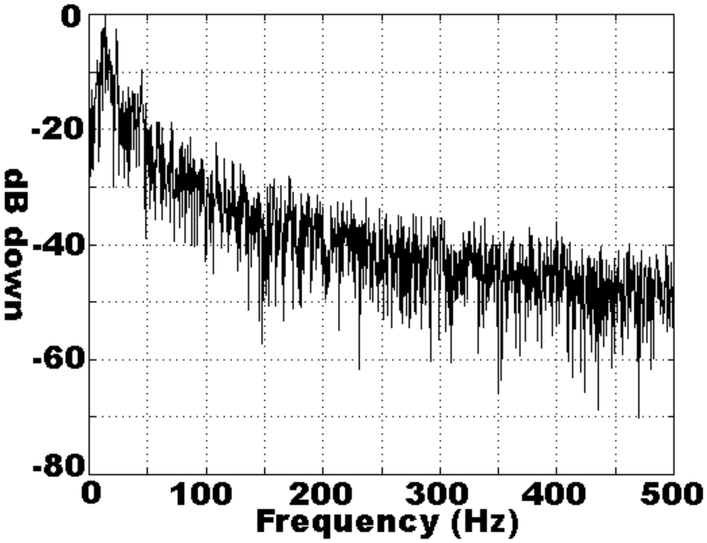

(a)

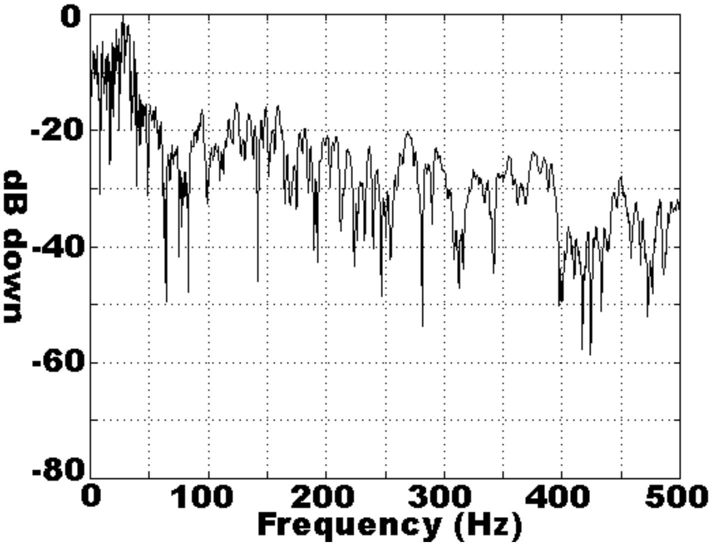

(b)

Fig.4.8. Amplitude spectrum of stacked receiver gather for (a) hydrophone at 18m depth and (b) vertical component geophone at 18m depth.

4.5 Processing the hydrophone cable data

Tube waves are the primary source of noise present on hydrophone data acquired in boreholes. This is true when the objective is to generate an image of the earth. The main objective of processing the hydrophone data was, therefore, to suppress tube waves and at the same time obtain an image that could be reliably interpreted. However, tube waves can also be used to determine valuable information about the rigidity of the solid surrounding the borehole as shown in White and Sengbush (1953) and Riggs (1955).

The steps involved in processing the hydrophone data (Figure 4.7) follow. After trace edits and mutes, shot statics computed during processing of the “low-resolution” 20m surface seismic survey were applied to the hydrophone data. Shot statics were small and therefore application of shot statics only marginally changed the moveout of events in the hydrophone receiver gathers (Figure 4.8). A spherical spreading gain correction using a preliminary RMS velocity function was then applied to the data.

In the simplest case, we can assume that tube waves bounce back and forth only from the top and bottom of the borehole. In other words, tube waves are predictable in time. The time taken for the tube wave to travel from the top to the bottom of the borehole and back was calculated to be around 150ms. Although an oversimplified assumption, it nevertheless forms a basis to use predictive deconvolution. It was observed that a predictive deconvolution operator with a 12ms prediction distance significantly suppressed tube waves. Several reflection events that were either not visible or feebly visible on the raw data were now be easily observed on the processed data (compare

Figures 4.9 and 4.10). The low-frequency and low-velocity tube waves were further reduced by *f-k* filtering of shot gathers of the data (Figure 4.11). Several events at times less than 1000ms are now clearly visible on the data. Figures 4.12-4.14 show the results of the above processing steps for three different shot gathers. Upgoing reflection events are much evident on the data in Figures 4.12 than in Figures 4.14. Notice a change in character in Figure 4.12 at a depth of about 44m due to the reflection and transmission of tube waves at that depth. Change in borehole rugosity at that depth is a likely reason for the reflection and transmission of tube waves at that depth. This change in character is notably absent on the processed shot gathers in Figures 4.13 and 4.14.

Velocity analysis of receiver gathers was then performed after trace equalization of the traces. The data were then VSPCDP stacked using the procedure discussed in Chapter 2. Several coherent reflections typical for the Blackfoot area are seen on the stacked section (Figure 4.15). Note that a cable every 750m or so would adequately image the reservoir at around 1000ms. Reflections on the stacked data away from the borehole show a better continuity compared to those closer to the borehole. This is because the tube wave contamination was stronger for shots closer to the borehole compared to shots at intermediate-to-far offsets from the borehole. The dead traces in the section represent missing shot locations along the profile. Time-variant spectral whitening was applied to the stacked data which was then passed through either an f-x deconvolution or a post-stack migration operator to give the final interpretable section.

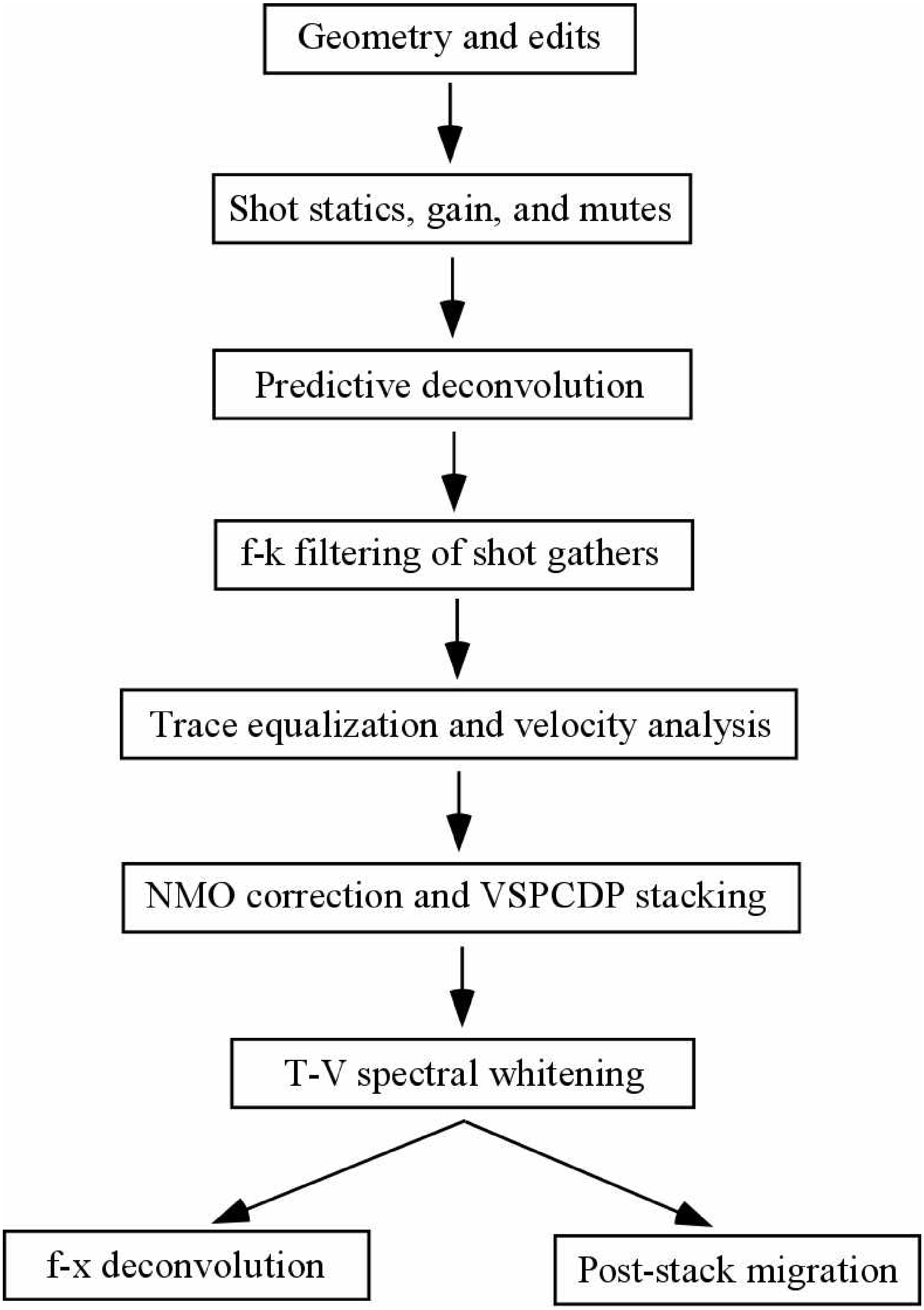

Fig.4.7. Hydrophone vertical cable processing flow.

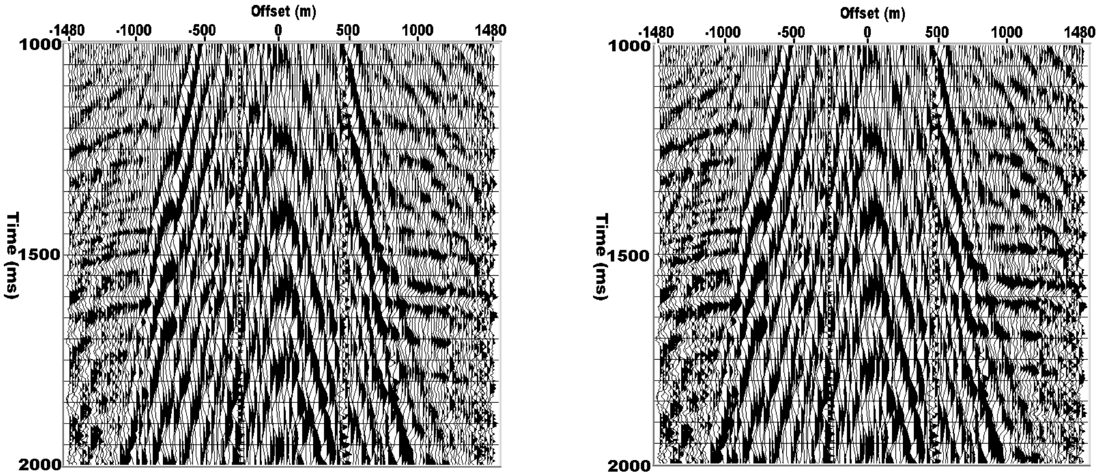

(a) with no statics

(b) with statics applied

Fig.4.8. Receiver gather for hydrophone at 98m depth.

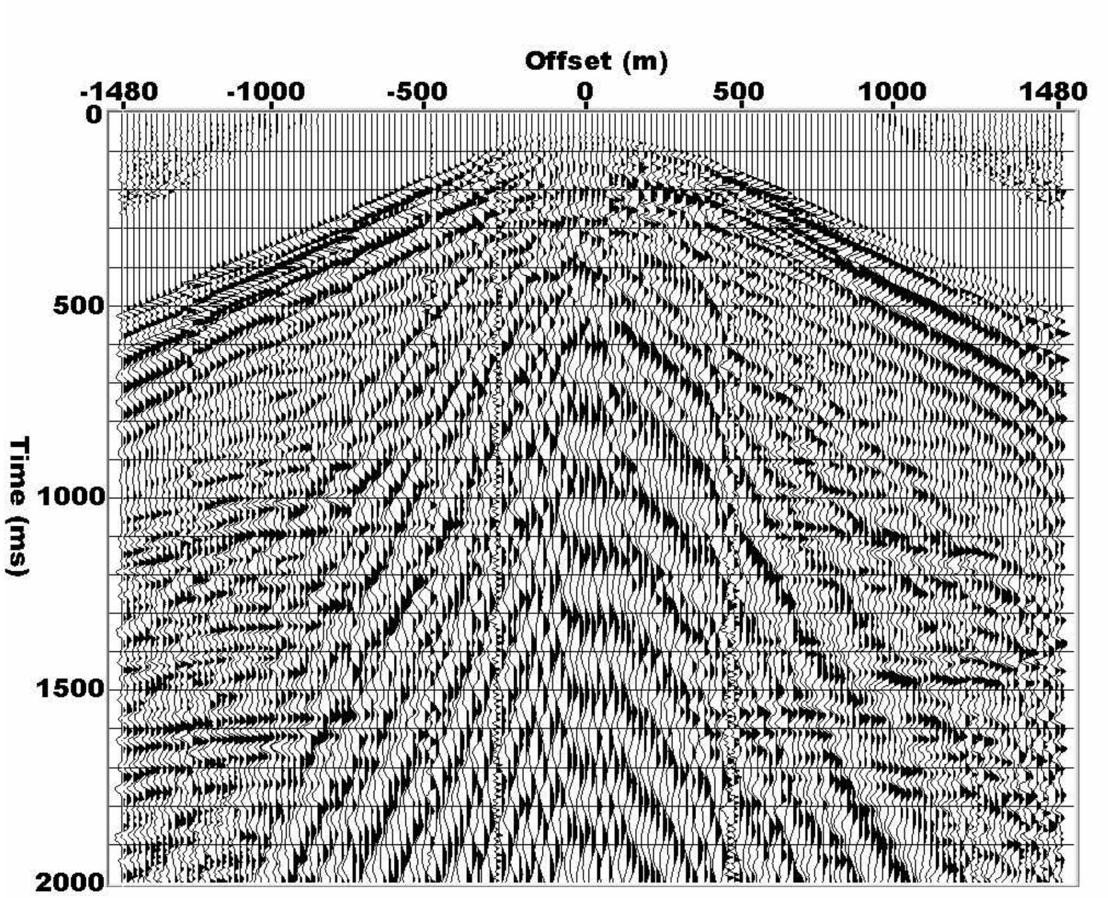

Fig.4.9. Raw receiver gather for hydrophone at 98m depth after application of shot statics. AGC is used for display purpose.

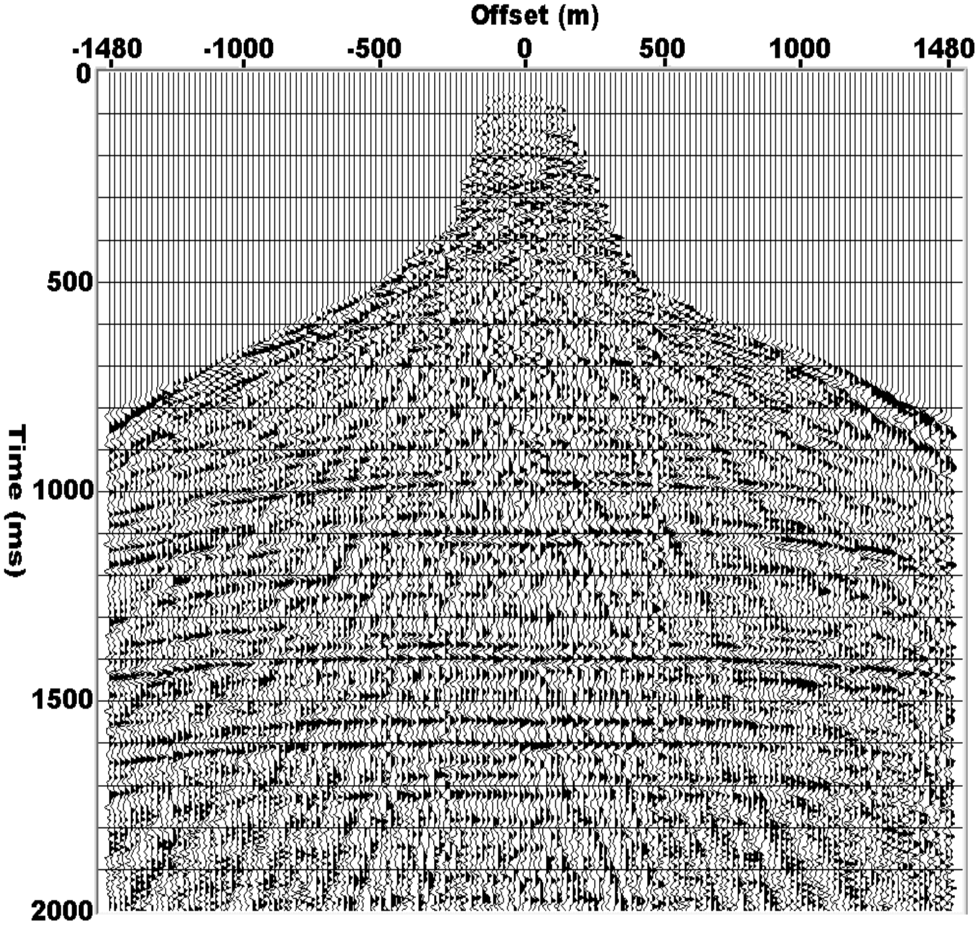

Fig.4.10. Same receiver gather as in Fig.4.9 but after top mute and predictive deconvolution, with AGC and a bandpass filter for display.

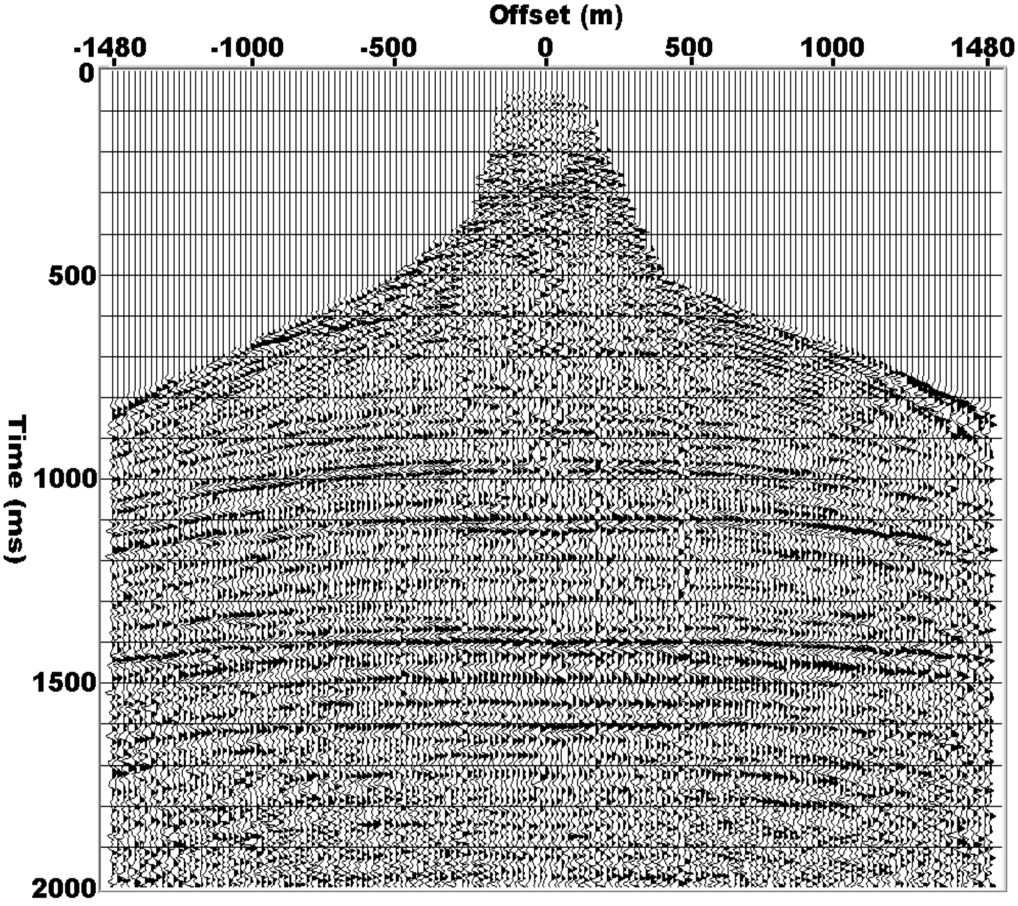

Fig.4.11. Same receiver gather as in Fig.4.10 but after *f-k* filtering of shot gathers, with AGC for display.

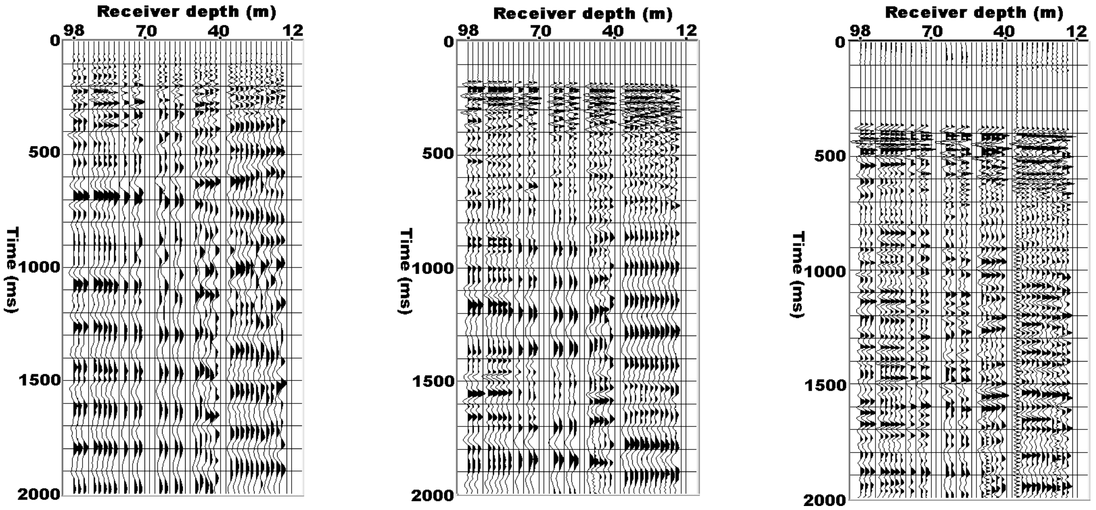

(a) (b) (c)

Fig.4.12. Shot gathers after application of gain. Shot offsets are (a) 112m, (b) 450m, and (c) 1000m. AGC used for display.

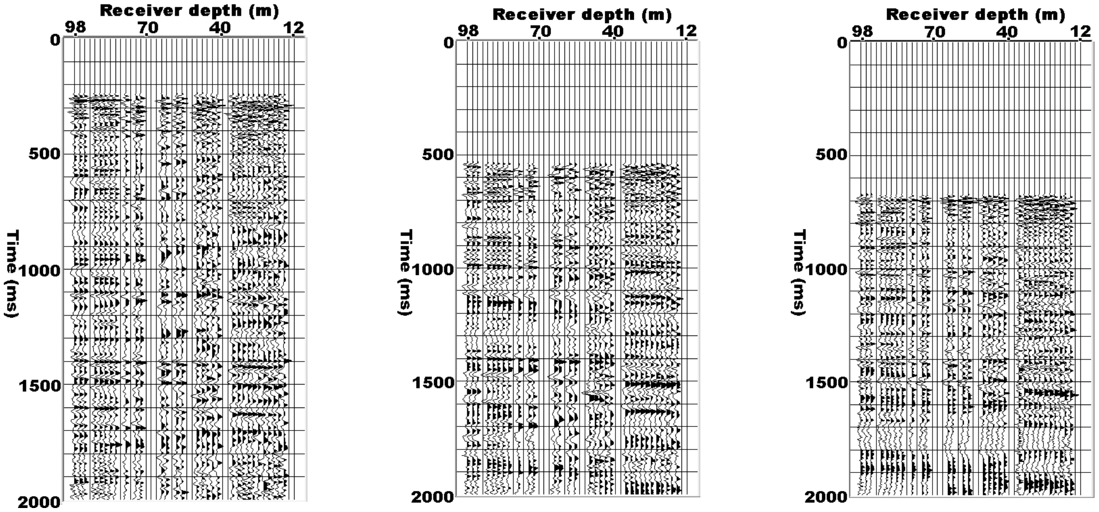

(a) (b) (c)

Fig.4.13. Shot gathers in Fig.4.12 after application of mute and predictive deconvolution. Shot offsets are (a) 112m, (b) 450m, and (c) 1000m. AGC and a bandpass filter used for display.

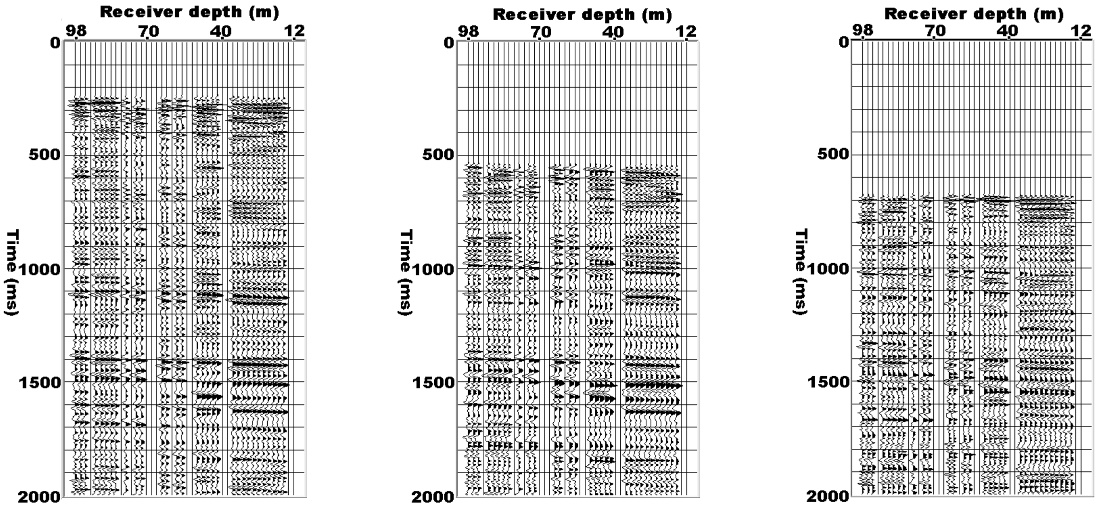

(a) (b) (c)

Fig.4.14. Shot gathers in Fig.4.13 after *f-k* filtering. Shot offsets are (a) 112m, (b) 450m, and (c) 1000m. AGC used for display.

F-x deconvolution of the whitened data resulted in a better continuity of events (Figure 4.16). The whitened VSPCDP stacked data were also migrated, under the assumptions discussed in Chapter 2, using migration velocities equal to the stacking velocities for the hydrophone gather in the centre of the vertical array (Figure 4.17). The quality of the final migrated section is certainly better than the f-x deconvolved stacked section. Events on the migrated section are more representative of the horizontal, flat-layered geology of the area than the f-x deconvolved section. This shows that post-stack migration, under certain limitations, can be successfully applied to stacked VSP data.

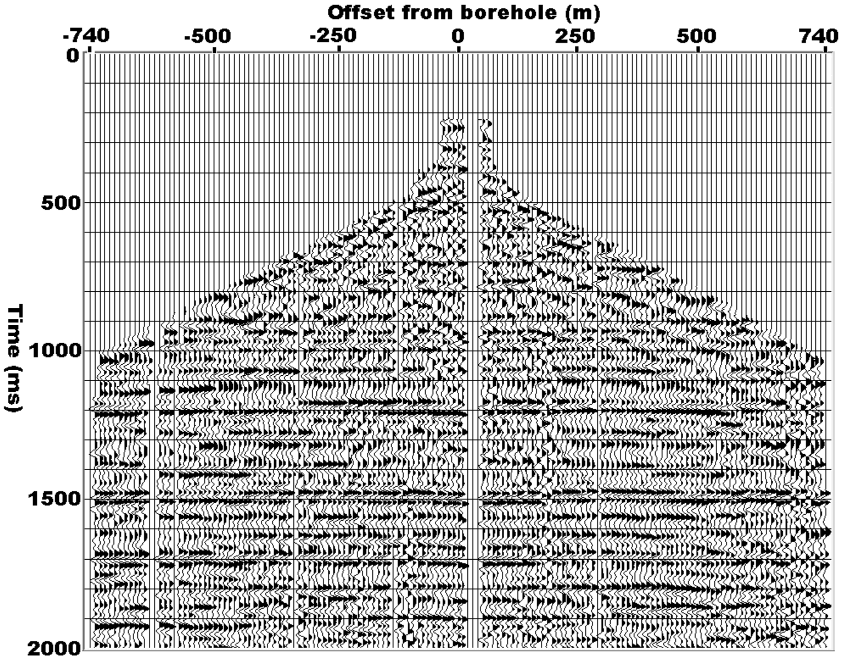

Fig.4.15. VSPCDP stacked section of the hydrophone data. Trace normalization used for display.

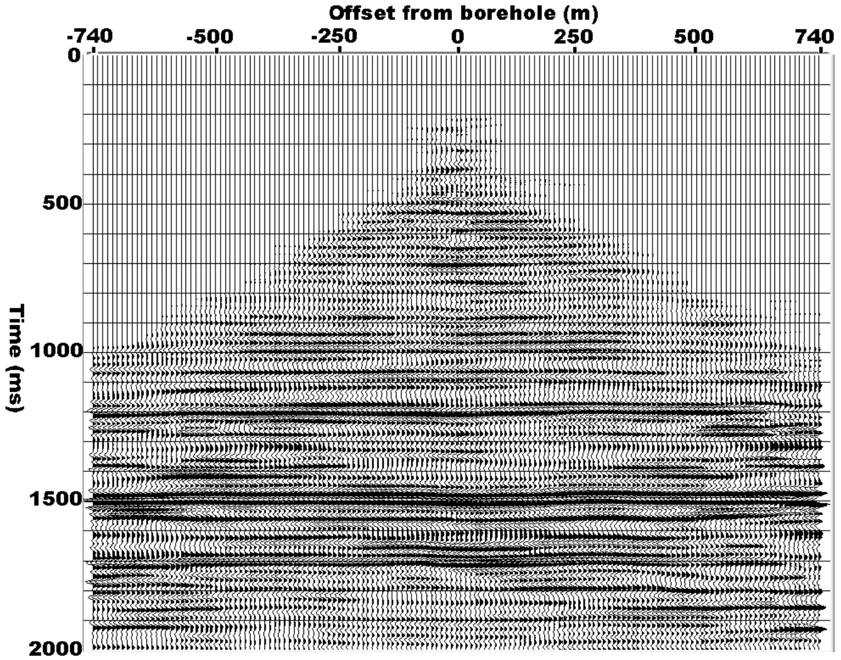

Fig.4.16. f-x deconvolution of the whitened VSPCDP stack in Figure 4.15.

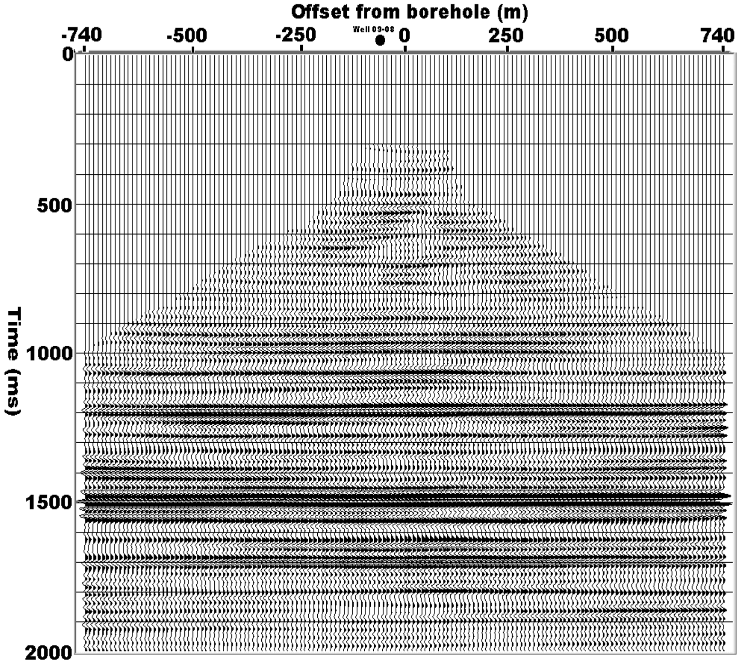

Fig.4.17. Post-stack migration of whitened VSPCDP stack in Figure 4.15.

4.6 Correlation and interpretation of the hydrophone data

The migrated hydrophone data (Figure 4.17) was then correlated with the final migrated section from the 20m surface seismic survey. The hydrophone data correlates well with the surface seismic data although it is lower frequency (Figure 4.18). Interpretation of the Blackfoot area has been performed by several people (eg. Miller, 1996 and Margrave et al., 1998). The purpose of the present exercise is not a complete interpretation of the area but to show that hydrophone data can be reliably interpreted. Events were identified on the hydrophone data by correlating it with a previously interpreted crossline from a 3C-3D survey over the area (Figure 4.19). Figure 4.20 shows events identified above and below the channel interval. In fact, the channel play is interpretable on the hydrophone section.

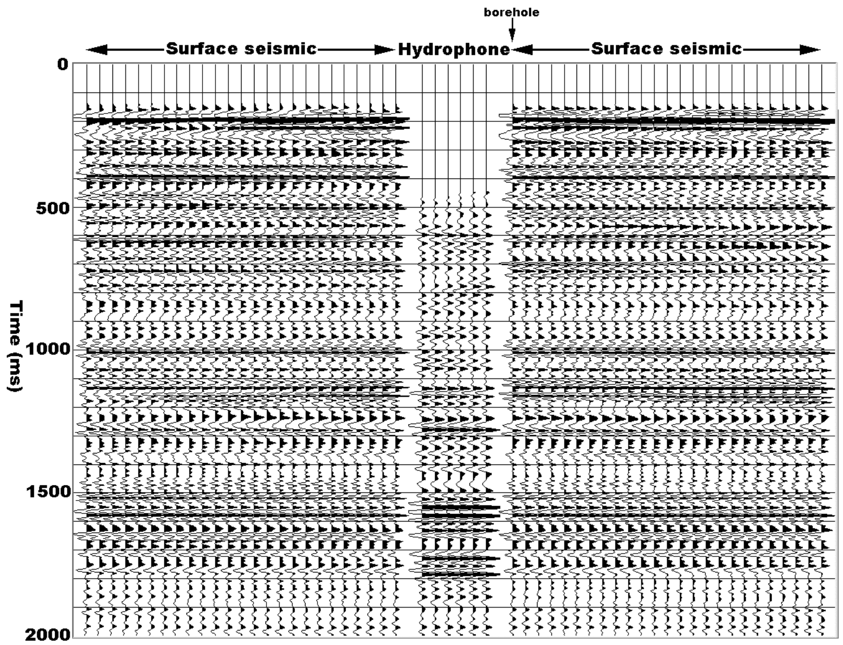

Fig.4.18. Migrated hydrophone traces near the borehole spliced into a section of the final migrated 20m surface seismic data.

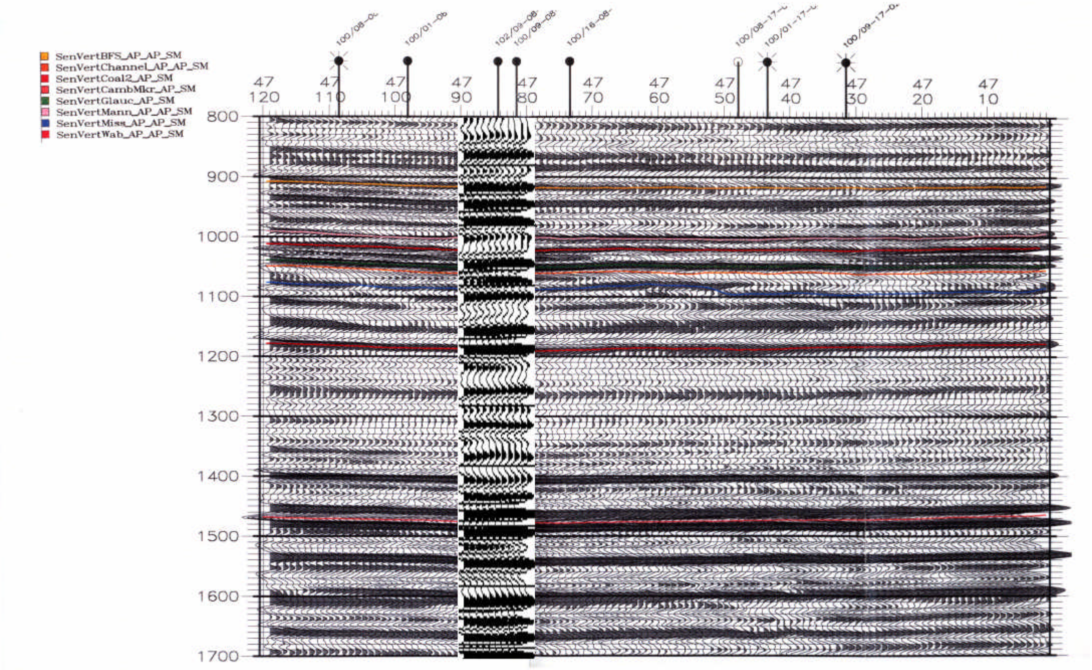

Fig.4.19. Migrated hydrophone traces inserted into a previously interpreted crossline from a 3C-3D survey in the area.

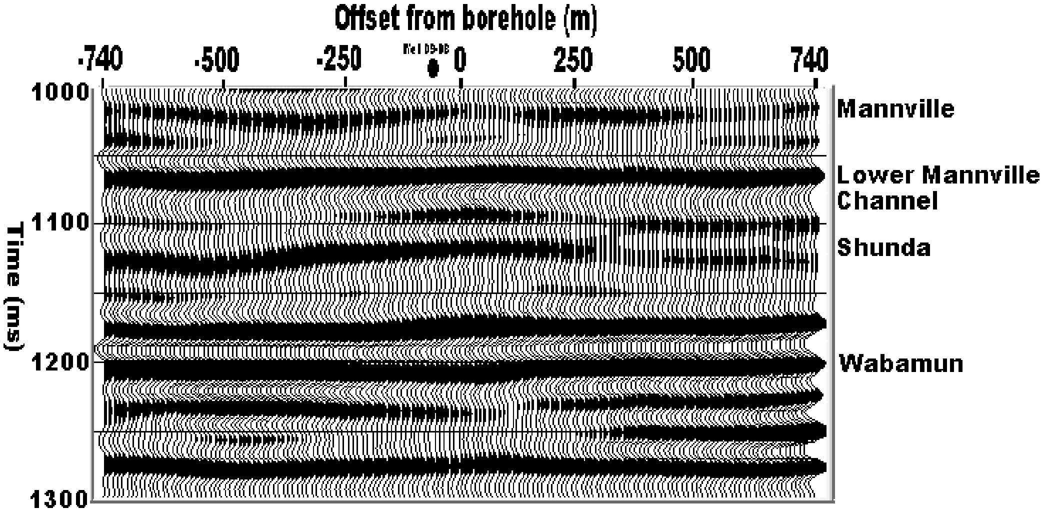

Fig.4.20. Interpreted hydrophone data. The channel at around 1100ms is clearly visible in the centre of the profile.

4.7 Discussion

Apart from resulting in rapid acquisition of VSP surveys, the vertical hydrophone cable may have advantages in other applications. In areas such as those covered by carbonates or basalts on the surface, the reflection signal is weak due to the strong impedance contrast among layers. In such areas, the problem could be minimized by the use of hydrophone cables in several areally distributed shallow boreholes. In coal exploration projects, boreholes usually have diameters of 7.6 cm or less and VSP in such boreholes is done using slimline wall-locking tools (Gochioco, 1998). Alternately, the vertical hydrophone cable due to the small size of hydrophones could easily be deployed in such boreholes and result in efficient acquisition. Since hydrophones in borehole are sensitive to fluid pressure generated by both compressional and shear wavefields impinging on the borehole wall, the vertical cable might also be used for full waveform inversion or imaging purposes.

4.8 Conclusions

Comparison of vertical hydrophone cable data with geophone data shows that in the long wavelength case, as predicted by theory (White, 1953), hydrophones in borehole represent the true earth motion. Tube wave contamination of hydrophone records is severe at short offsets and decreases with increasing offset. This property of increasing signal-to-noise ratio with increasing offset is very similar to that observed so commonly on ground roll affected geophone data.

In the simplest case, tube waves can be assumed to be predictable in time assuming that they bounce back and forth only from the top and bottom of the borehole. A predictive deconvolution operator used to suppress tube wave contamination on the hydrophone data was found to be very effective.

Processing of the vertical hydrophone cable data resulted in an image that correlated well with that from the 20m surface seismic survey and a previous 3-D seismic survey over the area. Events present on the surface geophone data were identifiable on the hydrophone data as well. In fact, the channel structure was very much interpretable on the hydrophone image. These correlations and interpretations indicate that hydrophones in boreholes would result not only in efficient acquisition of VSP data but also result in images that can be interpreted.

CHAPTER 5: CONCLUSIONS AND FUTURE WORK

5.1 Thesis conclusions

An approximate method for VSPCDP mapping of P-wave arrivals is developed for efficient imaging of large VSP data. The method, based on amplitude semblance analysis, is found to be robust and efficient. It gives reasonably accurate reflection maps when compared to the raytrace VSPCDP mapping method. It is also found that post-stack migration of VSPCDP stacked data, although theoretically incorrect, could be used under certain limitations.

The simultaneous acquisition of the Blackfoot 3-D VSP along with a surface 3-D program has shown that such surveys are possible and cost-effective. Both P-wave and converted-wave images from the 3-D VSP were observed to have good correlation with images from the surface 3C-3D survey. Time slices from the 3-D VSP inset into the surface seismic time slices also indicated the channel trend of the Blackfoot field. Although much work needs to be done to improve processing of the 3-D VSP data, results from this experimental survey were encouraging and showed the potential of the 3-D VSP. The 3-D VSP could be a significant tool to obtain detailed 3-D reservoir information near the well.

The Blackfoot land vertical cable data showed the promise of using hydrophones for acquiring VSP data. Tube waves, which were the primary source of coherent noise on the data, were effectively suppressed by a combination of predictive deconvolution and f-k velocity operators. The image from the land vertical cable data correlated very well with that from a 20m 2-D surface seismic data and a previous 3-D seismic data from the same area. The channel structure in the Blackfoot field was very much interpretable on the hydrophone image. These results show that hydrophones in borehole can not only result in efficient acquisition of VSP but also result in images that can be interpreted.

5.2 Future work

In view of most 3-D VSP surveys having few receiver levels (about 5 in most cases), accurate wavefield separation of VSP data remains the major concern in processing the 3-D VSP data. Wavefield separation techniques based on the Radon transform are well documented in the literature and such techniques could be tested on the Blackfoot 3-D VSP data for improved images. Also, accuracy of median-based technique may be improved by applying it on offset-sorted data that has been moved to zero-offset direct and reflection arrival times.

With increasingly large offsets in 3-D VSP data, VSP deconvolution may be inappropriate due to the first-break arrivals not being the direct arrivals. In such cases, statistical techniques such as surface-consistent deconvolution may be more appropriate.

Statics is another aspect of the 3-D VSP processing flow that has room for improvement. It may be possible to develop a ray parameter approach using the polarization of the VSP data to solve the statics problem.

The land vertical cable data could also be processed for generating converted-wave images.

REFERENCES

Al-Chalabi, M., 1973, Series approximation in velocity and traveltime computations: Geophysical Prospecting, 21, 783-795.

Bicquart, P., 1998, Application of Kirchhoff migration to 3D-VSP: Presented at 68th Ann. Intl. SEG Mtg., Expand. Abst., 389-392.

Blair, D.P., 1984, Rise times of attenuated seismic pulses detected in both empty and fluid-filled cylindrical boreholes: Geophysics, 49, 398-410.

Boelle, J., Kiaser, P. and Maocec, E., 1998, Difficulties and clues in 3D VSP processing: Presented at 68th Ann. Intl. SEG Mtg., Expand. Abst., 373-376.

Byun, B.S., Corrigan, D. and Gaiser, J.E., 1989, Anisotropic velocity analysis for lithology discrimination: Geophysics, 54, 1564-1574.

Chang, W. and McMechan, G.A., 1986, Reverse-time migration of offset vertical seismic profiling data using he excitation-time imaging condition: Geophysics, 51, 67-84.

Chen, G., 1998, 3D VSP CDP mapping with interactive reflection traveltime display: Presented at 68th Ann. Intl. SEG Mtg., Expand. Abst., 361-364.

Chen, H. and McMechan, G.A., 1992, 3-D pre-stack depth migration for salt and sub-salt structures using reverse-VSP data: J. Seis. Explor., 281-291.

Chen, G. and Peron, J.F., 1998, Mapping of 3D VSP data using quick ray tracing: Presented at 68th Ann. Intl. SEG Mtg., Expand. Abst., 365-368.

Clochard, V., Compte, P., Nicoletis, L., Lucas-Svay, J. and Dillon, P.B., 1997, 3D walk-away imaging in the overthrust model: Presented at the 57th Ann. EAGE Mtg., E047.

Clochard, V., Nicoletis, L., Svay-Lucas, J., Mendes, M. and Anjos, L., 1998, 3-C imaging of 3D walk-away data in regard to preprocessing: Presented at 68th Ann. Intl. SEG Mtg., Expand. Abst., 377-380.

Dangerfield, 1996, Shallow 3-D seismic and a 3-D borehole profile at Ekofisk field, in Ed. Brown, A., *Interpretation of three-dimensional seismic data*, AAPG Memoir 42.

DiSiena, J.P., Byun, B.S., Fix, J.E., and Gaiser, J.E., 1984, F-K analysis and tube wave filtering, in Eds. Toksoz, N.M. and Stewart, R.R., *Vertical Seismic Profiling, Part B-Advanced Concepts*, Geophys. Press.

Dillon, P.B. and Thomson, R.C., 1984, Offset source VSP surveys and their image construction: Geophysical Prospecting, 32, 790-811.

Dix, C.H., 1955, Seismic velocities from surface measurements: Geophysics, 20, 68-86.

Esmersoy, C., 1990, Inversion of P and SV waves from multicomponent offset vertical seismic profiles: Geophysics, 55, 39-50.

Fairborn, J.W. and Harding, R.S., Jr., 1996, 3D seismic velocity tomography at SPR sinkhole site, Weeks Island, Louisiana: Presented at 59th Ann. Intl. SEG Mtg., Expand. Abst., 896-898.

Farmer, P., Chapman, C., Fryer, A., Paul, A. and Sandvin, O., 1997, 3-D tomographic inversion and depth migration of VSP data. Presented at 60th Ann. Intl. SEG Mtg., Expand. Abst.

Findlay, M.J., Goulty, N.R., and Kragh, J.E., 1991, The crosshole seismic reflection method in opencast coal exploration: First Break, 9, 509-514.

First Break, 1997, Large 3D VSP survey completed on BP Magnus field: First Break, 15, 290.

Gaiser, J.E., Fulp, T.J., Petermann, S.G., and Karner, G.M., 1988, Vertical seismic profile sonde coupling: Geophysics, 53, 206-214.

Gal'perin, 1974, Vertical seismic profiling, Ed. White, J.E., SEG.

Gochioco, L.M., 1998, Shallow VSP work in the U.S. Appalachian coal basin: Geophysics, 63, 795-799.

Gulati, J.S. and Stewart, R.R., 1997, Seismic exploration through high-velocity layers: Presented at 67th Ann. Intl. SEG Mtg., Expand. Abst., 1297-1300.

Hardage, B.A., 1981, An examination of tube wave noise in vertical seismic profiling data: Geophysics, 46, 892-903.

Hardage, B.A., 1983, Vertical seismic profiling: Geophysical Press.

Hardage, B.A., 1992, Crosswell seismology and reverse VSP: Geophysical Press.

Hoffe, B.H., Stewart, R.R., Bland, H.C., Gallant, E.V., and Bertram, M.B., 1998, The Blackfoot high-resolution 3-C seismic survey: design and initial results, Presented at 68th Ann. Intl. SEG Mtg., Expand. Abst., 103-106.

Kennett, P., Ireson, R.L., and Conn, P.J., 1980, Vertical seismic profiles: Their applications in exploration geophysics: Geophysical Prospecting, 28, 676-699.

Kohler, K. and Koenig, M., 1986, Reconstruction of reflecting structures from vertical seismic profiles with a moving source: Geophysics, 51, 1923-1938.

Krail, P.M., 1994a, Measurements of cable shape in a cross current: Geophysics, 59, 1156-1159.

Krail, P.M., 1994b, Vertical cable as a sub-salt imaging tool: The Leading Edge, 885-887.

Krohn, C.E., and Chen, S.T., 1992, Comparisons of downhole geophones and hydrophones: Geophysics, 57, 841-847.

Labonte, S., 1990, Modal separation, mapping, and inverting three-component VSP data: M.Sc. Thesis, The University of Calgary.

Loewenthal, D., Lu, L., Roberson, R., and Sherwood, J., 1976, The wave equation applied to migration: Geophysical Prospecting, 24, 380-399.

Margrave, G.F., Lawton, D.C., and Stewart, R.R., 1998, Interpreting channel sands with 3C-3D seismic data: The Leading Edge, 4, 509-513.

Marzetta, T.L., Orton, M., Krampe, A., Johnston, L.K., and Wuenschel, P.C., 1988, A hydrophone vertical seismic profiling experiment: Geophysics, 53, 1437-1444.

Marzetta, T.L., 1992, Inverse borehole coupling theory and its application to hydrophone vertical seismic profiling: 62nd Ann. Internat. Mtg., Soc. Expl. Geophys., Expanded Abstracts, 145-147.

Miller, S.L.M., 1996, Multicomponent seismic data interpretation: M.Sc. thesis, University of Calgary.

Milligan, P.A., Rector III, J.W., and Bainer, R.W., 1997, Hydrophone VSP imaging at a shallow site: Geophysics, 62, 842-852.

Mittet, R., Landro, M., Hokstad, K. and Ostmo, S., 1997, A methodology for 3D elastic depth imaging of marine 3D walkaway data. Presented at the 57th Ann. EAGE Mtg., E046.

Moeckel, G.P., 1986, Moveout correction, bin and stack of offset VSP reflection data: 56th Ann. Int. Mtg. Soc. Expl. Geophys., Expanded Abstracts, 568-572.

Omnes, G., and Clough, P., 1998, Data acquisition with a 12-level 48-channel borehole seismic system: The Leading Edge, 17, 955-959.

Paulsson, B., and Fuller, B., 1998, An 80-level 3-C clamped receiver array for boreholes: P/GSI brochure.

Pham, L.D., Krohn, C.E., Murray, T.J., and Chen, S.T., 1993, A tube wave suppression device for cross-well applications: 63rd Ann. Internat. Mtg., Soc. Expl. Geophys., Expanded Abstracts, 17-20.

Riggs, E.D., 1955, Seismic wave types in a borehole: Geophysics, 20, 53-67.

Schuster, G.T., and Sun, Y., 1993, Wavelet filtering of tube and surface waves: 63rd Ann. Internat. Mtg., Soc. Expl. Geophys., Expanded Abstracts, 25-28.

Schoenberg, M., 1986, Fluid and solid motion in the neighbourhood of a fluid-filled borehole due to the passage of a low-frequency elastic plane wave: Geophysics, 51, 1191-1205.

Shekhtman, G.A. Zernov, A.E., Potapov, O.A., Lebedeva, I.I., Sokolova, K.B., 1993, Areal modification of the VSP method: Presented at the 55th Ann. EAGE. Mtg., P090.

Sheline, H.E., 1998, Crosswell seismic interpretation and reservoir characterization: An offshore case study: The Leading Edge, 17, 935-939.

Slotnick M.M., 1959, Lessons in seismic computing: Tulsa, SEG.

Stewart, R.R., 1984, VSP interval velocities from traveltime inversion: Geophysical Prospecting, 32, 608-628.

Stewart R.R., 1985, VSPCDP mapping: course notes 'Borehole Seismic Methods: Acquiring, processing, and interpreting VSP surveys', Western Atlas Logging Services, 1997.

Stewart R.R., 1991, Rapid map and inversion of P-SV waves: Geophysics, 56, 859-862.

Stewart, R.R. and Zhang, Q., 1996, 2-D and 3-D VSP interpretation: Blackfoot field, Alberta, CREWES Research Report, Chpt. 41.

Stewart, R.R. and Gulati, J.S., 1997, 3-D VSP: Recent history and future promise, CREWES Research Report, Chpt. 9.

Sun, Z. and Stewart, R.R., 1994, 3-D reverse VSP: CREWES Research Report, v. 6,Chpt. 12.

Taner, T.M. and Koehler, F., 1969, Velocity spectra-Digital computer derivation and applications of velocity functions: Geophysics, 34, 859-881.

Tessmer, G. and Behle, A., 1988, Common reflection point data-stacking technique for converted waves: Geophysical Prospecting, 36, 671-688.

Toksoz, N.M. and Stewart, R.R., 1984, Vertical Seismic Profiling, Part B-Advanced Concepts, Geophysical Press.

Van der Pal, R.C., Bacon, M. and Pronk, D., 1996, 3D walkaway VSP, enhancing seismic resolution for development optimization of the Brent field: First Break, 14, 463-469.

Van Sandt, D.R., and Levin, F.K., 1963, A study of cased and open holes for deep-hole seismic detection: Geophysics, 28, 8-13.

White, J.E., 1953, Signals in a borehole due to plane waves in the solid: J. Acoust. Soc. Am., 25, 906-915.

White, J.E., and Sengbush, R.L., 1953, Velocity measurements in near-surface formations: Geophysics, 18, 54-69.

Whitmore, N.D., and Lines, L.R., 1986, Vertical seismic profiling depth migration: Geophysics, 51, 1087-1109.

Wuenschel, P.C., 1976, The vertical array in reflection seismology – Some experimental studies: Geophysics, 41, 219-232.

Wuenschel, P.C., 1988, Removal of detector-ground coupling effect in the vertical seismic profiling environment: Geophysics, 53, 359-364.

Wood, J.M., and Hopkins, J.C., 1992, Traps associated with paleovalleys and interfluves in uncorfomity bounded sequence: Lower Cretaceous Glauconitic Member, Southern Alberta, Canada: AAPG Bull., 76(6), 904-926.

Wyatt, K.D. and Wyatt, S.B., 1984, Determining subsurface structure using the vertical seismic profile, in Eds. Toksoz, N.M. and Stewart, R.R., *Vertical Seismic Profiling, Part B-Advanced Concepts*, Geophys. Press.

Yang, G.Y.C., Lawton, D.C., Stewart, R.R., Miller, S.L.M., Potter, C.C., and Simin, V., 1996, Interpretation and analysis of the Blackfoot 3C-3D survey, CREWES Project Research Report, Chpt. 46.

Zhang, Q., Stewart R.R., and Sun, Z., 1995, 3-D VSP: Survey design and processing: CREWES Project Research Report, v. 7, ch. 34, 1-24.

Zhang, Q., Stewart R.R. and Sun, Z., 1997, 3D borehole seismic imaging and correlation – a field experiment. Presented at the 59th Ann. EAGE Mtg., E048.

Zhang, Q., Stewart R.R., Parkin, J.M. and Sun, Z., 1996, Analysis of the Blackfoot 3C-3D VSP survey, CREWES Project Research Report, Chpt. 40.